



UNIVERSITÀ  
DEGLI STUDI  
FIRENZE

PhD  
in  
Earth Sciences

CYCLE XXXIII

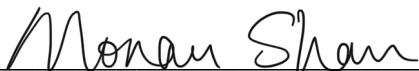
COORDINATOR Prof. Francalanci Lorella

**Permafrost Deformation Monitoring and Interpretation  
Using InSAR Technique in Northeastern China and Aosta  
Valley Region, Italy**

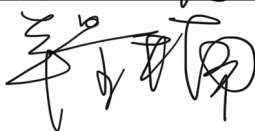
Academic Discipline (SSD) GEO/05

**Doctoral Candidate**

Dr. Shan Monan

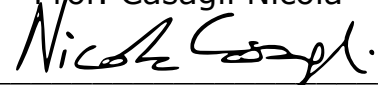
  

---



**Supervisors**

Prof. Casagli Nicola



Dr. Bianchini Silvia



**Coordinator**

Prof. Francalanci Lorella

---

Years 2017/2020



# Contents

<b>INTRODUCTION .....</b>	<b>1</b>
1.1 Permafrost and permafrost degradation .....	1
1.2 Landslides .....	5
1.3 Research Objective .....	8
1.4 Structure of the Thesis .....	9
<b>RADAR, SAR AND INSAR .....</b>	<b>10</b>
2.1 Earth Observation .....	10
2.2 Radar Remote Sensing and Synthetic Aperture Radar (SAR) .....	11
2.2.1 Radar Remote Sensing .....	11
2.2.2 Synthetic Aperture Radar (SAR) .....	13
2.3 SAR Interferometry (InSAR) and Differential InSAR (DInSAR) .....	17
2.4 Persistent Scatterers InSAR (PSI) and SqueeSAR™ Method .....	20
<b>CASE STUDY 1: LOW-LAND PERMAFROST REGION OF NORTHEASTERN CHINA.....</b>	<b>22</b>
3.1 Study Area .....	22
3.2 Data and processing methods .....	23
3.2.1 Sentinel-1 .....	24
3.2.2 ALOS PALSAR.....	29
3.3 Results .....	33
3.3.1 ALOS PALSAR SqueeSAR™ processing .....	33
3.3.2 ALOS PALSAR differential interferometry processing .....	41
3.3.3 Sentinel-1 SqueeSAR™ and differential interferometry processing.....	46
3.4 Discussion .....	53
3.4.1 Sentinel-1 .....	53
3.4.2 ALOS PALSAR .....	55
3.4.3 Other possible sensors .....	56
<b>CASE STUDY 2: AOSTA VALLEY REGION, NORTHWESTERN ITALY.....</b>	<b>58</b>
4.1 Introduction .....	58
4.2 Study Area, data, and methodology .....	60
4.2.1 Aosta Valley Region .....	60

4.2.2 Rock glacier inventory data of Aosta Valley Region .....	62
4.2.3 Sentinel-1 SqueeSAR™ processing results .....	63
4.2.4 ALOS PALSAR data and DInSAR processing .....	65
4.3 Results .....	67
4.3.1 Permanent scatters and distributed scatters (PS/DS) detected in the Rock Glaciers by Sentinel-1 SqueeSAR™ analysis .....	67
4.3.2 Using ALOS PALSAR L-band differential interferometry to map the active rock glaciers in the late summer season of 2007 .....	76
4.4 Discussion .....	78
4.4.1 ALOS PALSAR differential interferometry processing and the updated results of active rock glacier mapping .....	78
4.4.2 Sentinel-1 SqueeSAR™ processing results and the seasonality of active rock glaciers in VdA Region...	81
<b>CONCLUSION AND FUTURE RECOMMENDATIONS .....</b>	<b>86</b>
<b>ACKNOWLEDGEMENTS .....</b>	<b>88</b>
<b>REFERENCE .....</b>	<b>89</b>

## List of Tables

<b>Table 1.1</b> Landslide velocity scales (Cruden & Varnes, 1996) .....	7
<b>Table 2.1</b> SAR bands, wavelengths, and frequency (Ortiz, 2017).....	13
<b>Table 2.2</b> Major PSI based methodologies.....	20
<b>Table 3.1</b> Sentinel-1 imaging information.....	26
<b>Table 3.2</b> Acquisition geometry of Sentinel-1 .....	26
<b>Table 3.3</b> ALOS PALSAR FBS and FBD products .....	30
<b>Table 3.4</b> ALOS PALSAR data used in this study. ....	30
<b>Table 3.5</b> Imaging information of ALOS PALSAR data .....	30
<b>Table 3.6</b> Acquisition geometry of ALOS PALSAR data.....	31
<b>Table 3.7</b> ALOS PALSAR SqueeSAR™ processing information .....	34
<b>Table 3.8</b> The interferometric parameters of the studied points .....	37
<b>Table 3.9</b> The interferometric parameters of the studied points .....	38
<b>Table 3.10</b> The interferometric parameters of the studied points .....	40
<b>Table 3.11</b> Processing information of ALOS PALSAR differential interferogram .....	41
<b>Table 3.12</b> Sentinel-1 SqueeSAR™ processing information.....	46
<b>Table 3.13</b> Processing information of Sentinel-1 differential interferogram.....	47
<b>Table 4.1</b> Satellite information of Sentinel-1 SqueeSAR™ processing.....	63
<b>Table 4.2</b> The imaging dates of the acquired available ALOS PALSAR data within the study area provided by ESA TPM on-the-fly service.....	65
<b>Table 4.3</b> Planned interferometric pairs. ....	66
<b>Table 4.4</b> Statistics of the displacement time series of the detected active rock glaciers using Sentinel-1 SqueeSAR™ analysis.....	69
<b>Table 4.5</b> The characteristic information of the studied rock glacier .....	71
<b>Table 4.6</b> The interferometric parameters of the studied points .....	71
<b>Table 4.7</b> The characteristic information of the studied rock glaciers.....	71
<b>Table 4.8</b> The interferometric parameters of the studied points .....	71

**Table 4.9** Experiment records of ALOS PALSAR differential interferogram processing in VdA Region. The temporal baseline of each interferometric pair is listed in the brackets. The items colored in red refers to the ideal differential interferogram used in the active rock glacier mapping. .... 80

## List of Figures

<b>Figure 1.1</b> Circum-Arctic Map of Permafrost and Ground Ice Conditions .....	2
<b>Figure 1.2</b> Permafrost Favorability Index map of Alps Mountains in Europe (Azócar, 2016) .....	3
<b>Figure 1.3</b> Permafrost Favorability Index map of northeastern China, eastern Mongolia and eastern Siberia, Russia (Azócar, 2016) .....	4
<b>Figure 1.4</b> Global Landslide Susceptibility Map (2000-2013, Stanley & Kirschbaum, 2017) .....	6
<b>Figure 1.5</b> Global Fatal Landslide Database (2004-2016, Froude & Petley, 2018) .....	6
<b>Figure 2.1</b> Side-looking radar .....	12
<b>Figure 2.2</b> Angles in spaceborne radar imaging (Rizzoli & Bräutigam, 2014).....	12
<b>Figure 2.3</b> Diagram of vegetation penetration capability among X-, C- and L-band sensors (Pham et al., 2019) .....	14
<b>Figure 2.4</b> Illustration of ascending and descending spaceborne SAR satellite geometries (Capes et al., 2009) .....	14
<b>Figure 2.5</b> Past and current SAR satellites used for historical analysis and ongoing monitoring.....	15
<b>Figure 2.6</b> Foreshortening, shadow, and layover of SAR imaging.....	16
<b>Figure 2.7</b> Schematic picture of SAR differential interferometry.....	17
<b>Figure 2.8</b> Interferogram of the Qinghai earthquake.....	18
<b>Figure 2.9</b> Distribution of displacement in the line-of-sight direction between satellites and surface .....	19
<b>Figure 3.1</b> Study area .....	23
<b>Figure 3.2</b> Sentinel-1 Constellation Revisit & Coverage Frequency .....	24
<b>Figure 3.3</b> Sentinel-1 imaging modes.....	25
<b>Figure 3.4</b> Diagram of Sentinel-1 core products .....	26
<b>Figure 3.5</b> Acquisition geometry diagram of Sentinel-1.....	26
<b>Figure 3.6</b> GEP, EO Services for Land Subsidence monitoring thematic application and DIAPASON S-1 processing interface. ....	27
<b>Figure 3.7</b> ALOS PALSAR imaging modes.....	29
<b>Figure 3.8</b> Acquisition geometry diagram of ALOS PALSAR .....	31
<b>Figure 3.9</b> The presented workflow .....	32
<b>Figure 3.10</b> ALOS PALSAR SqueeSAR™ Mean Displacement Velocity Results .....	35

<b>Figure 3.11</b> Delineated possible permafrost zones using ALOS PALSAR SqueeSAR™ processing results.....	35
<b>Figure 3.12</b> Analyzed degrading permafrost patch No.1 and the high-resolution optical imagery of June 2004 and July 2011 near the permafrost patch No.1.....	36
<b>Figure 3.13</b> The displacement time series of the studied points in permafrost patch No.1.....	36
<b>Figure 3.14</b> Analyzed degrading permafrost patch No.2 and the high-resolution optical imagery of June 2004, August 2008, and September 2010 near the permafrost patch No.2.....	37
<b>Figure 3.15</b> The displacement time series of the studied points in permafrost patch No.2.....	38
<b>Figure 3.16</b> Analyzed degrading permafrost patch No.2 and the high-resolution optical imagery of June 2004, August 2008, and September 2010 near the permafrost patch No.3.....	39
<b>Figure 3.17</b> The displacement time series of the studied points in permafrost patch No.3.....	39
<b>Figure 3.18</b> 20071211-20080126 ALOS PALSAR differential interferogram and corresponding SqueeSAR™ results.....	42
<b>Figure 3.19</b> 20081213-20090128 ALOS PALSAR differential interferogram and corresponding SqueeSAR™ results.....	43
<b>Figure 3.20</b> 20090615-20090731 ALOS PALSAR differential interferogram and corresponding SqueeSAR™ results.....	44
<b>Figure 3.21</b> 20100618-20100803 ALOS PALSAR differential interferogram and corresponding SqueeSAR™ results.....	45
<b>Figure 3.22</b> Sentinel-1 SqueeSAR™ Mean Displacement Velocity Results .	48
<b>Figure 3.23</b> 20161230-20170111 Sentinel-1 differential interferogram and corresponding SqueeSAR™ results .	49
<b>Figure 3.24</b> 20170722-20170803 Sentinel-1 differential interferogram and corresponding SqueeSAR™ results .	50
<b>Figure 3.25</b> 20171201-20171213 Sentinel-1 differential interferogram and corresponding SqueeSAR™ results .	51
<b>Figure 3.26</b> 20180717-20180729 Sentinel-1 differential interferogram and corresponding SqueeSAR™ results .	52
<b>Figure 3.27</b> Cropped Sentinel-1 SqueeSAR™ mean displacement velocity result .	57
<b>Figure 3.28</b> Cropped ALOS PALSAR SqueeSAR™ mean displacement velocity result .	57
<b>Figure 4.1</b> Hill shade map that represents the mountainous geomorphology of the VdA Region. ....	60
<b>Figure 4.2</b> 10-meter resolution Digital Terrain Model (DTM, 10-meter resolution) of VdA Region .....	61
<b>Figure 4.3</b> Rock glacier inventory dataset in VdA Region.....	62
<b>Figure 4.4</b> The results of Sentinel-1 SqueeSAR™ analysis in VdA Region, ascending geometry, November 2014 to June 2020 .....	63



<b>Figure 4.5</b> The results of Sentinel-1 SqueeSAR™ analysis in VdA Region, descending geometry, November 2014 to June 2020.....	64
<b>Figure 4.6</b> The time series of displacement of the rock glaciers in VdA Region, Sentinel-1 ascending orbit, SqueeSAR™ method, from July 2015 to June 2020.....	67
<b>Figure 4.7</b> Mean displacement rate map of the rock glaciers in VdA Region, Sentinel-1 descending orbit, SqueeSAR™ method, from July 2015 to June 2020.....	68
<b>Figure 4.8</b> Detected La Clapey Gerbioz rock glacier.....	70
<b>Figure 4.9</b> The displacement time series of the studied points in La Clapey Gerbioz rock glacier and the MODIS 8-day land surface temperature from November 2014 to July 2020.....	72
<b>Figure 4.10</b> Detected rock glaciers Example No.2.....	73
<b>Figure 4.11</b> The displacement time series of the studied points in the example 2 and the MODIS 8-day land surface temperature from October 2014 to July 2020.....	75
<b>Figure 4.12</b> Wrapped ALOS PALSAR 20070802-20070917 differential interferogram.....	76
<b>Figure 4.13</b> Delineated active rock glaciers using ALOS differential interferogram and Sentinel-1 SqueeSAR™ processing.....	77
<b>Figure 4.14</b> MODIS 8-day Land Surface Temperature at La Clapey Gerbioz rock glacier, January 2004 to January 2011.....	83
<b>Figure 4.15</b> MODIS 8-day Land Surface Temperature at La Clapey Gerbioz rock glacier, January 2014 to January 2021.....	83
<b>Figure 4.16</b> The displacement time series of the studied points in the La Clapey Gerbioz rock glacier case study and ERA5 monthly aggregated precipitation data from November 2014 to July 2020.....	84
<b>Figure 4.17</b> The displacement time series of the studied points in the example 2 and ERA5 monthly aggregated precipitation data from October 2014 to July 2020.....	85

## List of Acronyms

**ADEOS:** Advanced Earth Observing Satellite

**ALOS:** Advanced Land Observing Satellite

**APS:** Atmospheric Phase Screen

**ASI:** Italian Space Agency, Agenzia Spaziale Italiana in Italian language

**A.s.l.:** Above sea level

**ASTER:** Advanced Spaceborne Thermal Emission and Reflection Radiometer

**AVNIR:** Advanced Visible and Near Infrared Radiometer

**CNES:** The National Center for Space Studies, Centre National d'Études Spatiales in French language

**COSMO-SkyMed:** Constellation of Small Satellites of Mediterranean basin Observation

**CPT:** Coherent Pixels Technique

**DEM:** Digital Elevation Model

**DIAPASON:** Differential Interferometric Automated Process Applied to Survey of Nature

**DInSAR:** Differential Synthetic Aperture Radar Interferometry

**DLR:** German Aerospace Center, Deutsches Zentrum für Luft- und Raumfahrt in German language

**DS:** Distributed Scatterers

**DSM:** Digital Surface Model

**EC:** European Commission

**ENVISAT:** Environmental Satellite

**EO:** Earth Observation

**ERAS:** ECMWF (European Center for Medium-Range Weather Forecasts) re-analysis generation 5

**ERS:** European Remote Sensing Satellite

**ESA:** European Space Agency

**ETM:** Enhanced Thematic Mapper

**EW:** Extra Wide Swath

**FBS:** Fine Beam Single

**FBD:** Fine Beam Dual

**GBInSAR:** Ground Based Synthetic Aperture Radar Interferometry

**GEE:** Google Earth Engine

**GEP:** Geohazards Exploitation Platform

**GIS:** Geographic Information System

**GMT:** Greenwich Mean Time

**GNSS:** Global Navigation Satellite System

**GPS:** Global Positioning System

**IFFI:** Italian landslides inventory, "Inventario dei Fenomeni Franosi in Italia" in Italian language

**InSAR:** Synthetic Aperture Radar Interferometry

**IPTA:** Interferometric Point Target Analysis

**IW:** Interferometry Wide

**JAXA:** Japan Aerospace Exploitation Agency

**JERS:** Japanese Earth Resources Satellite

**JPL:** Jet Propulsion Laboratory

**LiDAR:** Light Detection and Ranging

**LOS:** Line-of-sight

**LST:** Land Surface Temperature

**MODIS:** Moderate Resolution Imaging Spectroradiometer

**MTInSAR:** Multi-temporal Synthetic Aperture Radar Interferometry

**NASA:** National Aeronautics and Space Administration

**NISAR:** NASA-ISRO Synthetic Aperture Radar

**PALSAR:** Phase Array type L-band Synthetic Aperture Radar

**PFI:** Permafrost Favorability Index

**PLR:** Polarimetry

**POT:** Pixel Offset Tracking

**PRISM:** Panchromatic Remote Sensing Instrument for Stereo Mapping

**PS:** Persistent Scatterers

**PSInSAR (PSI):** Persistent Scatterers Synthetic Aperture Radar Interferometry

**RADAR:** Radio Detection and Ranging

**SAR:** Synthetic Aperture Radar

**SAOCOM:** Argentine Microwaves Observation Satellite, "Satélite Argentino de Observación Con Microondas" in Spanish language

**SBAS:** Small Baseline Subset

**SHP:** Statistically Homogenous Pixels

**SLC:** Single Look Complex

**SM:** StripMap

**SNAP:** Sentinel Application Platform

**SPOT:** Satellite for observation of Earth, "Satellite Pour l'Observation de la Terre" in French language

**StaMPS:** Stanford Method for Persistent Scatterers

**TOPSAR:** Terrain Observation with Progressive Scans Synthetic Aperture Radar

**TPM:** Third Party Mission

**UTC:** Coordinated Universal Time

**VdA:** Aosta Valley, "Valle d'Aosta" in Italian language

## Abstract

InSAR algorithms have been widely applied in monitoring and mapping for the purposes of engineering geology research and the InSAR derived products have been extensively used in geological risk management by administrative entities and Emergency Management authorities. In this PhD thesis, the research was focusing on the application of InSAR technique, including conventional DInSAR and advanced SqueeSAR™ in cold regions, (1) to locate the deformation hotspot caused by permafrost degradation, then to improve the regional permafrost mapping; (2) to analyze the deformation characteristics caused by the degradation of permafrost temporally and spatially.

The research was developed on two sites of cold regions of different geomorphologies. The first case study was focusing on the detection of permafrost degradation phenomena using DInSAR and SqueeSAR™ in the low-land permafrost distributed hilly regions in northern Heilongjiang Province, northeastern China. The study area is located at the southern margin of Siberia permafrost region, which is the largest area of the permafrost distribution in the northern Hemisphere. Studies have been revealing that the increasing mean annual air temperature in this study area has been causing the degradation of permafrost in decades and have been bringing geological risks to man-made infrastructures. Initially, the SqueeSAR™ analyses using C-band Sentinel-1 and L-band ALOS PALSAR were conducted to reveal the overall displacements time series in the extracted permanent and distributed scatterers of the study area. Then the DInSAR analyses using Sentinel-1 and ALOS PALSAR data were completed to map the deformation hotspot of the study area. Lastly, by combination of the results acquired by SqueeSAR™ and DInSAR analyses, the possible spatial distribution of permafrost deformation hotspot was mapped. PS and DS in the permafrost deformation hotspot are selected and analyzed to reveal the characteristics of permafrost degradation in the study area. The results indicate that in the permafrost distributed areas, the deformation velocity has been reduced in recent years from 2015 to 2019 than 2007 to 2010, roughly a decade ago. It could be related to the final degradation phase of the permafrost in recent years.

In the second case study, the feasibility of DInSAR and SqueeSAR™ in the study of active rock glacier in Alpine environments of mountainous geomorphologies of Aosta Valley Region, Italy was demonstrated, and the deformation characteristics corresponding to the seasonality of active rock glacier were discovered. The seasonal dynamic feature of the active rock glaciers was then analyzed using the regional monitoring results of Aosta Valley Region using Sentinel-1 SqueeSAR™ technique and the regional active rock glacier investigation dataset. Interestingly, according to the result of the analysis, the displacement time series of active rock glacier in Aosta Valley Region has shown a half-year lapse compared with the change of regional annual air temperature that is contradictive to the conventional understanding of permafrost deformation dynamics. The driving factor of such phenomena was left unfound and open to the future analysis. Second, combined with high-resolution optical remote sensing imagery, the conventional DInSAR analysis using ALOS PALSAR data collected in summer season of 2007 has detected more active rock glaciers than the regional active rock glacier investigation dataset. The results have provided the possibility of further analysis of improving active rock glacier mapping using InSAR method in the future.

In conclusion, this research highlights the value of using spaceborne DInSAR and SqueeSAR™ methods in mapping and monitoring active periglacial landforms in cold regions at regional scale. Thanks to its short revisiting time and medium to high spatial resolution, Sentinel-1 data can be used for systematic and continuous monitoring of ground deformation, especially slow and very slow periglacial processes due to the changing climate in cold regions but the effectiveness of the usage of Sentinel-1 in dealing with winter snow cover and dense vegetation should be enhanced. On the other hand, L-band ALOS PALSAR data has solved the problem of vegetation coverage, which extensively exists in the cold region that has limited the

capability of InSAR monitoring. The methods mentioned in this thesis are intended to be implemented in the regional or local geological hazard management in both study areas.



## Chapter 1. INTRODUCTION

### 1.1. Permafrost and permafrost degradation

Permafrost is defined as soil or rock that remains at or below 0 °C for at least two consecutive years (Brown et al., 2000; French, 2017; Rouyet et al., 2019). Widespread in the world, permafrost is a key element of the cryosphere, covering approximately 24% of the Earth's continental surface and occurring both on land and beneath offshore arctic continental shelves (Brown et al., 2000). More general, the cryosphere, which represents all kind of frozen environments, including glaciers, permafrost, lake, and river ice are home to approximately 10% of the global population (Hock et al., 2019).

The Global Permafrost Distribution Map that determined by the ice content is shown in **Figure 1.1** (Heginbottom et al., 1993; Brown et al., 2002). In 2017 Azócar et al., introduced an innovative way to model the likelihood of the occurrence of the permafrost globally in a statistical way. The result is renamed as "Permafrost Favorability Index" (PFI). The PFI map of European Alps is shown in **Figure 1.2** and The PFI map of low-land permafrost in northeastern China, Mongolia and Siberia, Russia is shown in **Figure 1.3**. A lower PFI indicates the higher uncertainty of the existence of permafrost within the pixel and its unstable thermal state development in the coming years under the background of global climate change.

The permafrost functions as inertia in different means. Its impermeable frozen layer controls the growth of the vegetation by controlling the water supplies. It is also a reservoir for the storage of organic matters. Moreover, the annual freeze and thaw cycle occurs on the top active layer alters the land surface thermal conditions (Outcalt et al., 1990; Christensen et al., 2004; Daout et al., 2017).

Influenced by the state changes of the ground ice profile, permafrost areas are prone to both seasonal and long-term surface deformation due to the annual seasonal changes and the inter-annual climate change (Eppler et al., 2015). The top layer of the permafrost, which thaws in warming seasons and refreezes in winter, is called active layer (Shur et al., 2005). During the annual freezing and thawing cycles, the thickness of the active layer keeps altering then has caused the quantity of water/ice content in the active layer varies temporal and spatial unevenly (Nelson et al., 2002), and the water-ice phase change in can induce centimeter, even decimeter scale heave and subsidence, therefore can influence the stability of the local infrastructure (Qingbai et al., 2002; Romanovsky et al., 2008; Harris et al., 2009; Harris et al., 2011; Chang & Hanssen, 2015; Strozzi et al., 2020). Having caused great attention from the public, climate change refers to the change of the mean climatic state over time. In the last decades, the continuously increasing average global surface temperature clearly indicates a warming trend worldwide and having caused a significant increment of temperature and increasing precipitation that having accelerated the degradation of the permafrost (Shan et al., 2015). Meanwhile, compare to other regions, global climate warming is most evident in Arctic regions, where the average air temperature has increased approximately twice as the situation of the rest of the world in the last few decades.

Permafrost is vulnerable to the climate change at various spatial and temporal scales (Cheng & Wu, 2007). Thawing permafrost has influenced the local hydrology, ecology, climate, and has brought severe geological hazards as well. In the Alpine mountainous geomorphology, as the climate change occurs, the accumulated loose debris may induce the development of rock glaciers (Delaloye et al., 2008). On hilly geomorphologies, mass-wasting processes create various creeping landforms (e.g., rock glaciers, solifluction, gelifluction) depending on topography, climate, water content, roughness of shear surface, etc. (Haeberli et al., Matsuoka, 2001) Landslides and debris flow could be induced by the increasing



extreme weather event in these years through altering the thermal state of the permafrost (Kharuk et al., 2013; Shan et al., 2015).

The presence of permafrost is an important factor that should be considered in civil engineering in permafrost distributed or favorable regions. The planning and construction of infrastructures, including railways, oil pipelines, expressways, buildings, etc., is influenced by the ground deformation of sufficient magnitude initiated by the permafrost degradation and reversely, it will alter the thermal regime of the permafrost underneath the ground.

Therefore, permafrost monitoring plays a vital role in natural hazard management. However, on one hand, in-situ investigations consume a lot of human power a financial budget and can only collect the observation and measurement in limited spots, which could bring problems during the interpolation.

In the last decades, satellite remote sensing has been demonstrated as a powerful tool to investigate large scale, and less accessible areas at high spatial and temporal resolution with a lower cost. Although as a subsurface condition that is unlikely to be directly observed from the optical satellites, but the geomorphological change can be interpreted and analyzed by other sensors (Bartsch et al., 2016; Trofaier et al., 2017; Strozzi et al., 2018). Spaceborne Synthetic Aperture Radar (SAR) sensors are especially favorably in the detection of ground deformation day-and-night at as high as millimeter levels of accuracy without the consideration of weather condition. Ground deformation that caused by permafrost degradation observed by multi-temporal SAR interferometry at local, regional, and global scale would provide new inspects in permafrost degradation mapping.

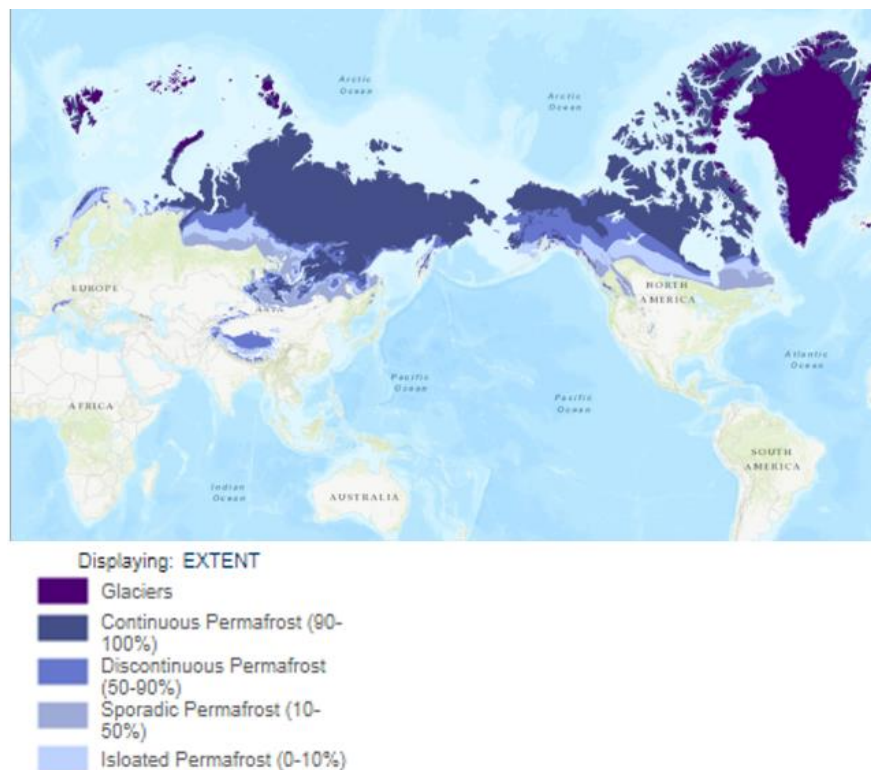


**Figure 1.1** Circum-Arctic Map of Permafrost and Ground Ice Conditions (Heginbottom et al., 1993; Brown et al., 2002)

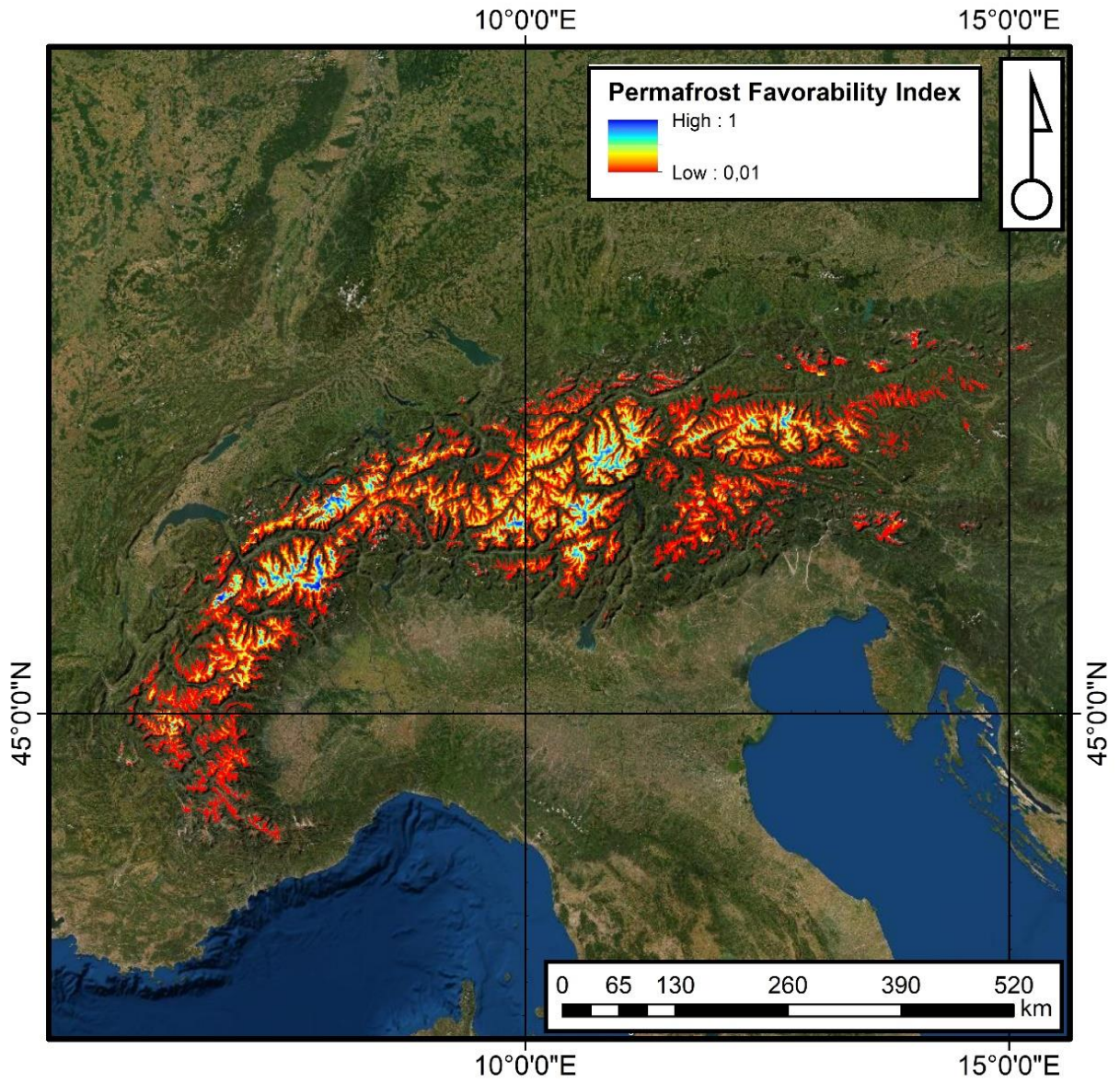


**Figure 1.2** Permafrost Favorability Index map of Alps Mountains in Europe (Azócar, 2016)

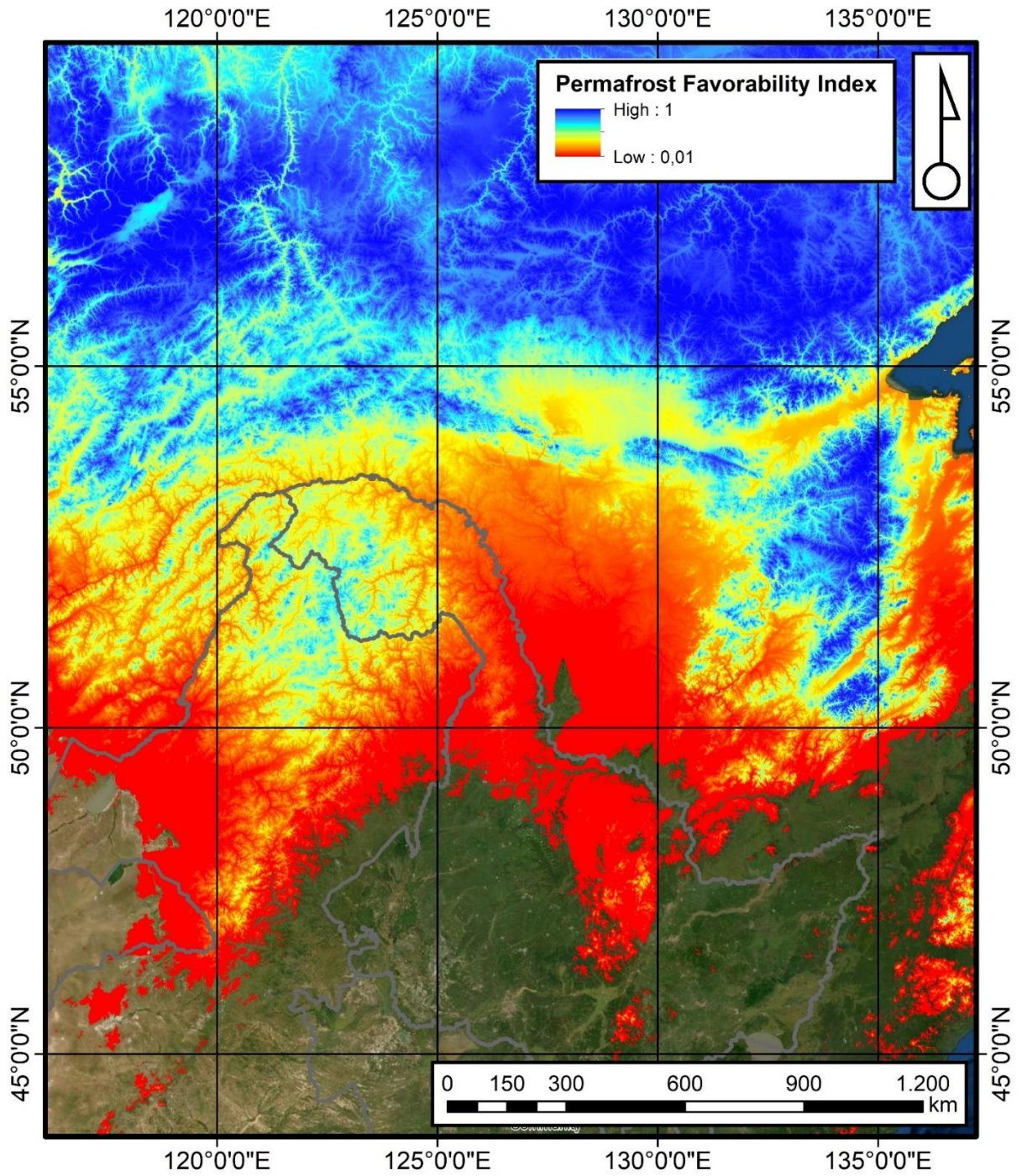


**Figure 1.3** Permafrost Favorability Index map of northeastern China and eastern Russia (Azócar, 2016)

## 1.2. Landslides

Landslide is a major type of geological hazard occurring ubiquitously worldwide. The term “landslide” was defined as “the movement of a mass of rock, debris or earth down a slope” by Cruden (1991). Landslides are usually driven by tectonic, climatic, or human activities (Froude & Petley, 2018).

Landslide susceptibility refers to the likelihood of the occurrence of a landslide. Landslide susceptibility maps identify areas and regions which are prone to occur landslide events and labeled from low to high. **Figure 2.1** shows a Global Landslide Susceptibility Map of 2000 to 2013 created by Stanley & Kirschbaum (2017). Many landslides are initiated by the permafrost degradation in different geomorphologies. Various parameters, including data on slope, fault, geology, forest loss, and road network were combined into a Geography Information System (GIS) using a heuristic fuzzy approach. From the **Figure 2.1**, a series of landslide susceptibility hotspot cluster can be recognized (e.g., western coast of America continent, southwestern China, Himalayan Arc, etc.). Fatal landslides refer to the landslide events with losses of lives. The spatial distribution of fatal landslide from 2004 to 2017 is studied by Froude & Petley (2018) and shown in **Figure 2.2**. From this **Figure 2.2**, fatal landslides occur mainly in densely populated Asian countries (e.g., central, and southern China, India, Pakistan, Japan, etc.).

Velocity is one of the most important parameters in landslide classification. It is regarded as a key proxy which indicates landslide intensity given the same volume of landslide body, the more rapid the movement, the severer the damage it will cause. Cruden & Varnes (1996) classified the landslides using velocity into seven classes from extremely slow to extremely rapid, shown in **Table 1.1**. Normally, for the deformation caused by a type of periglacial landform like the degradation of active rock glaciers or low-land permafrost patches, their velocity seldomly exceed a level of meter per year. Such relatively slow velocity is favorable for the InSAR technique to monitor in long term.

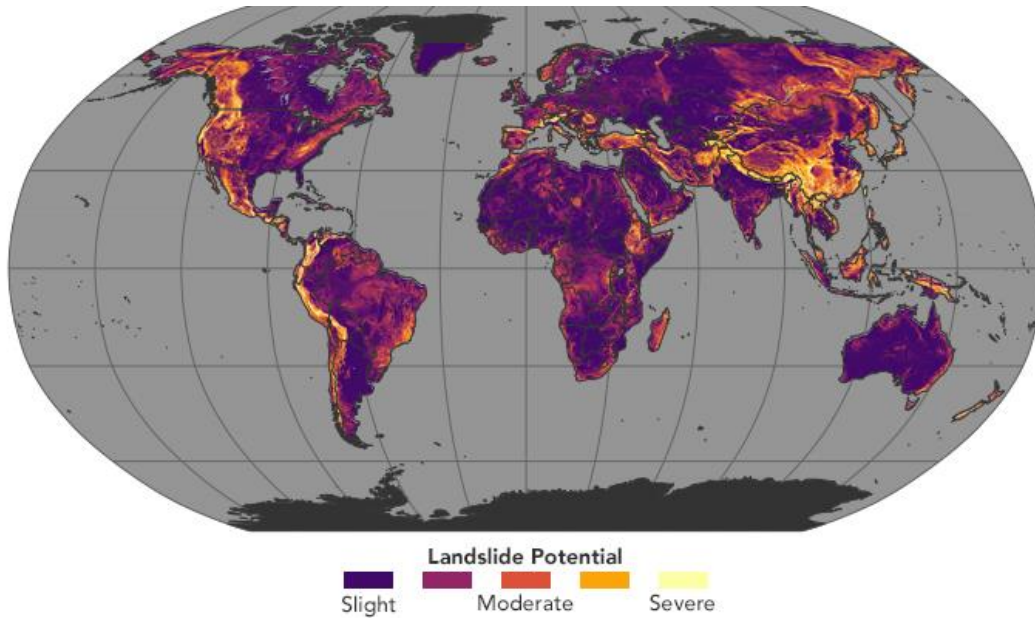


**Figure 1.4** Global Landslide Susceptibility Map (2000-2013, Stanley & Kirschbaum, 2017)

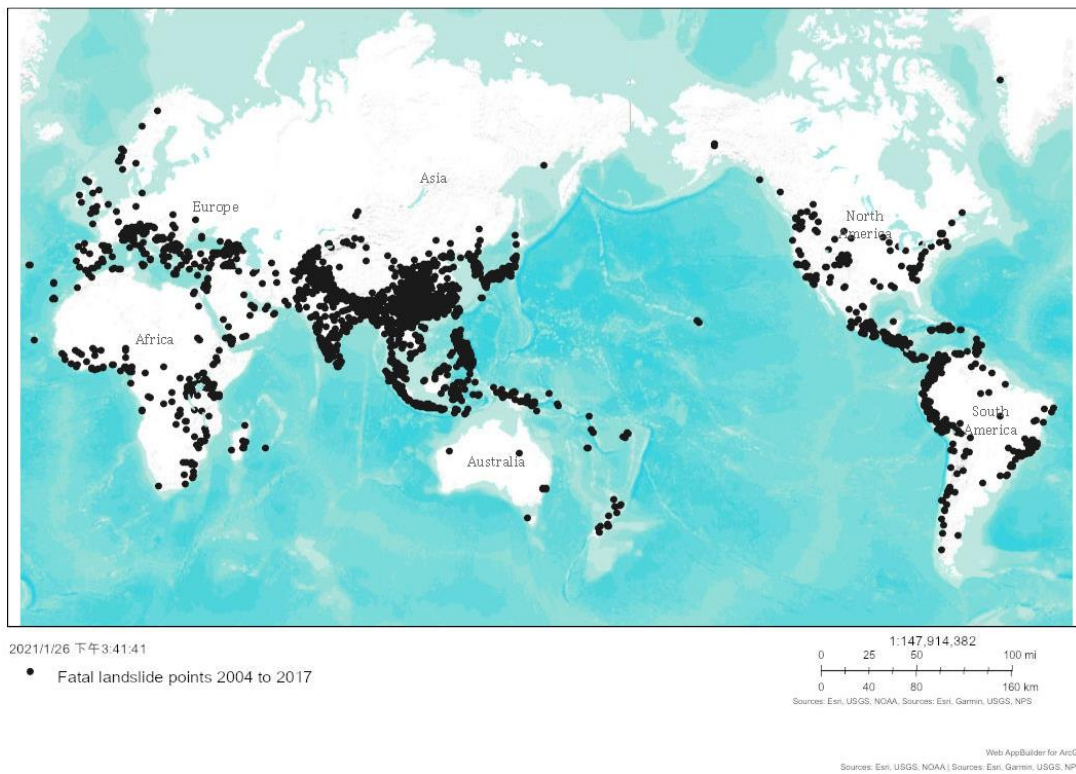


**Figure 1.5** Global Fatal Landslide Database (2004-2016, Froude & Petley, 2018)

Velocity Class	Description	Velocity (mm/sec)	Typical Velocity	Aftermaths
7	Extremely rapid	$5 * 10^3$	5 m/sec	Catastrophe of major violence; buildings destroyed by impacted displaces material; many deaths; no escape
6	Very rapid			Some lives lost; velocity too great to permit persons to escape
		$5 * 10^1$	3 m/min	
5	Rapid			Escape evacuation possible; structures, possessions and equipment destroyed
		$5 * 10^{-1}$	1.8 m/h	
4	Moderate			Some temporary ad intensive structures can be temporarily maintained
		$5 * 10^{-3}$	13 m/month	
3	Slow			Remedial construction can be undertaken during movement; intensive structures can be maintained with frequent maintenance work if total movement is not large during a particular acceleration phase
		$5 * 10^{-5}$	1.6 m/year	
2	Very slow			Some permanent structures undamaged by movement
		$5 * 10^{-7}$	16 mm/year	
1	Extremely slow			Imperceptible without instrument; construction possible with precautions

**Table 1.1** Landslide velocity scales (Cruden & Varnes, 1996)

### 1.3. Research Objective

This research is aimed to assess the capability of using SqueeSAR™ and differential interferometry technique to monitor ground stability in low-land permafrost regions of northeast China, and in alpine permafrost regions in Aosta Valley Region in northwest Italy, therefore, to testify if SAR interferometry can be regarded as a powerful tool to detect the degradation of periglacial landforms in greater cryosphere research under the background of global climate change.

The highlights of this work are:

- The exploration of L-band SAR interferometry in permafrost degradation detection in highly vegetated region improved the performance of the C-band SAR interferometry processing in the same area.
- The application of SqueeSAR™ algorithm in rock glacier dynamic analysis in Aosta Valley Region has revealed the half-year lapse of the dynamic of active rock glacier, compared to the conventional permafrost deformation time series.
- Using conventional DInSAR method to detect active rock glaciers in Alpine environment has improved the regional active rock glacier investigation dataset.

## **1.4. Structure of the Thesis**

This thesis is divided into five chapters.

The first chapter introduces the definition of permafrost, permafrost degradation, the definition and classification of landslide (geohazards), and then states the research objectives.

The second chapter depicts the knowledge of radar remote sensing and InSAR technique.

The third chapter shows and discusses the ground deformation results derived from Sentinel-1 SqueeSAR™, ALOS PALSAR SqueeSAR™, Sentinel-1 DInSAR and ALOS PALSAR DInSAR analysis of permafrost regions in northeastern China.

The fourth chapter shows how to use the results derived from regional Sentinel-1 SqueeSAR™ analysis to interpret the dynamic of active rock glaciers and uses ALOS PALSAR DInSAR analysis to enhance the active rock glacier mapping in Aosta Valley Region of northwestern Italy.

The fifth chapter illustrates the conclusion and future recommendation of the application of SqueeSAR™ and more general InSAR technique in the geological hazard research of cold regions.



## Chapter 2. Radar, SAR and InSAR

### 2.1. Earth Observation

Earth Observation (EO) is the gathering of information about Earth's physical, chemical, and biological systems by remote sensing technologies and by ground-based techniques. Compared to the ground-based techniques, the remote sensing technologies can conduct their missions of observation and measurement in a more effective way, providing a global or regional coverage all at once with relatively high spatial and temporal resolution.

Since 1960, after the first launch of a US meteorological satellite, hundreds of satellites with the general mission of EO have been launched and have been providing useful observations and measurements of hydrology, meteorology, climatology, oceanography, geology, biology, and other unnamed information from the space (Selva & Krejci, 2012). The increasing demand for EO missions probably is the clearest trend from the current progresses for international cooperation in the field of environmental monitoring, and EO satellites has been proven their efficiency to be regarded as essential elements in these years (Sandau, 2010).

Satellite-based EO data acquired by microwave-based sensor, compared to the optical spectrum sensor, is being increasingly and widely applied in the field of monitoring and detection of geological hazards and disasters due to its outstanding capability in various working conditions, including day-and-night operation and penetration into the atmosphere under all conditions (smoke, cloud, rain and so on, Solari, 2017).

## 2.2. Radar Remote Sensing and Synthetic Aperture Radar (SAR)

### 2.2.1. Radar Remote Sensing

The word “RADAR” is the acronym for “Radio Detection And Ranging”. It is a detection system that allows to use electromagnetic waves to determine the accurate current location and the velocity of movement of objects. Radar technique was designed for military applications initially and has been applied into civil and scientific utilizations only from a few years ago (Hanssen, 2001).

Radar technique uses two-ways travel time of pulses to determine the range to the sensing object and its backscattered intensity to distinguish the type of the targets, so radar can be regarded as an active sensing technique that is different from the passive ones, such as optical and thermal remote sensing (Confuorto, 2016).

Initiated by the launch of SEASAT satellite on June 27, 1978, by the National Aeronautics and Space Administration/Jet Propulsion Laboratory (NASA/JPL), which is the first radar mission for civilian applications, spaceborne imaging radars began to play a vital role in EO and remote sensing. The increasing application of radar remote sensing nowadays has provided an efficient way in the research of monitoring geological and geomorphological progresses, especially in the remoted, less accessible places where the field work is hard to be operated.

**Figure 2.1** indicates how a side-looking radar works. The flight direction of side-looking spaceborne radar is always perpendicular to the looking side. And nowadays, right is usually designed as the looking side. It means on a right-looking spaceborne radar, the antenna is always sensing and imaging the ground surface from the right side. This direction is called azimuth direction. The area sensed by the radar sensor is called antenna footprint. The width of the antenna footprint is called swath. The direction points from the satellite to the observed target is called slant range. The sensor to target direction is called line-of-sight direction. The off-nadir angle refers to the angle between the imaginary line that links the antenna to the nadir point and the line-of-sight direction. The incidence angle is the angle between the slant range and the imaginary line perpendicular to the Earth’s surface (**Figure 2.2**).

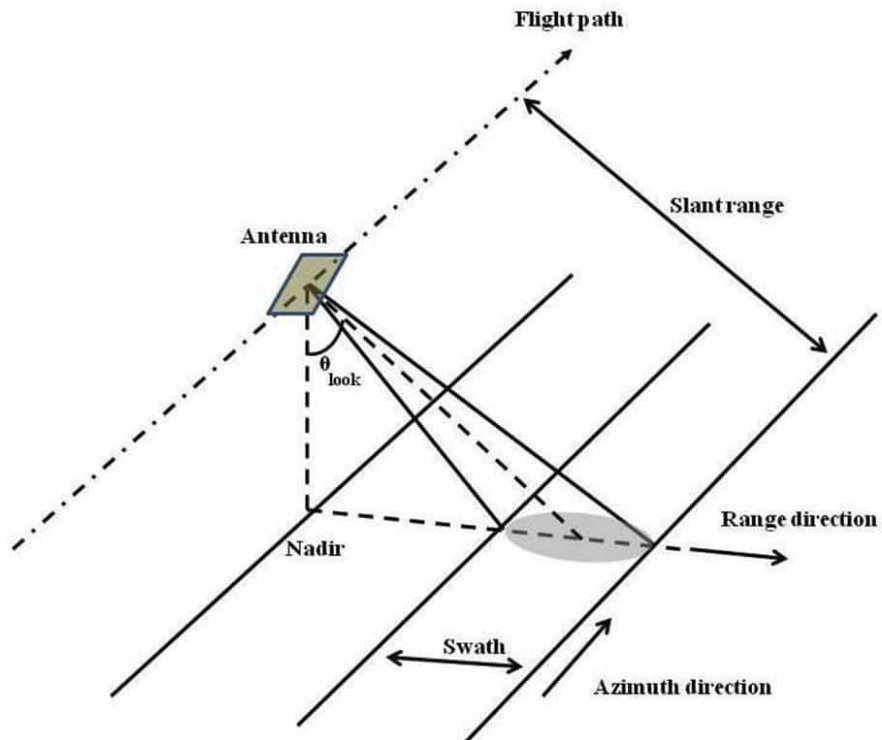


Figure 2.1 Side-looking radar (source: <https://asf.alaska.edu/information/sar-information/what-is-sar/> )

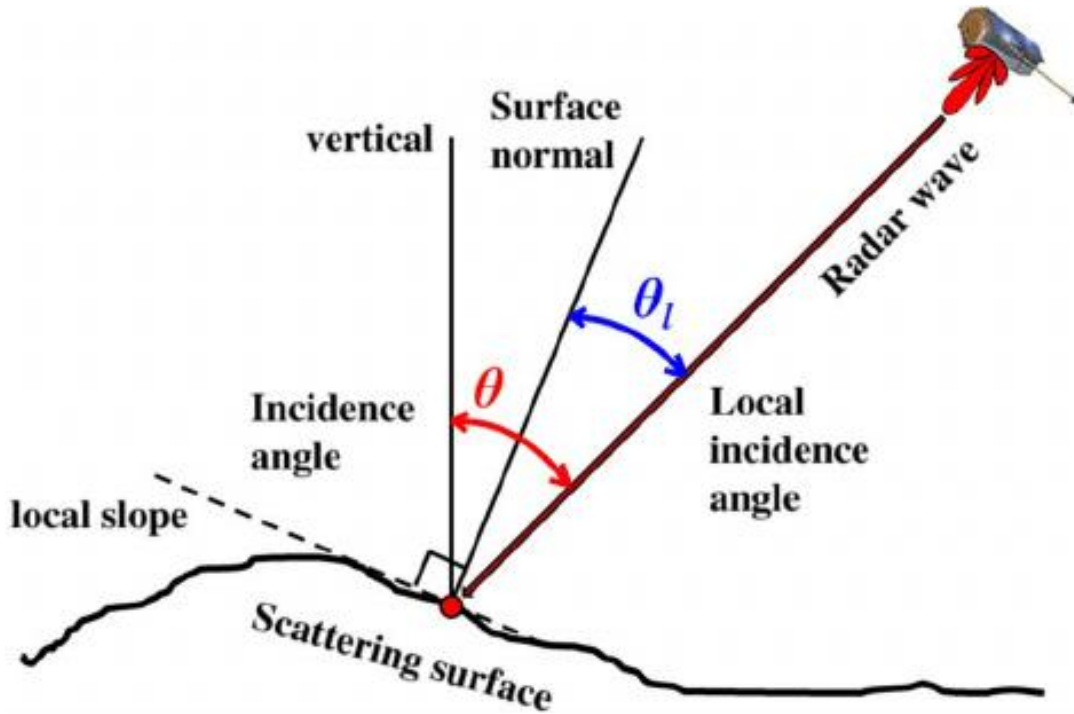


Figure 2.2 Angles in spaceborne radar imaging (Rizzoli & Bräutigam, 2014)

### 2.2.2. Synthetic Aperture Radar (SAR)

Synthetic Aperture Radar (SAR) is a type of radar imaging technique to create two-dimensional images or three-dimensional objects. Mounted on a moving platform, it “synthesizes” the acquired radar images along the flight path to “enlarge” the antenna aperture, then to improve the spatial resolution in the regional or global monitoring than conventional scanning radar systems. A spaceborne SAR sensor is carried by a satellite along a predefined polar orbit with the transmitting antenna pointed to the ground surface in the plane perpendicular to the orbit (Hooper, 2006).

Since its first applications, SAR has been demonstrated to be a powerful EO tool that have improved the understanding of Earth surface (over land, ice, and sea) physical progresses. SAR data are acquired in K-, X-, C-, L- and P- bands according to the different wavelengths with different polarizations, therefore, to have a variety of spatial resolutions (Sinha et al., 2015). **Table 2.1** lists the normal SAR bands, wavelengths, and their frequency.

Band	Wavelength (cm)	Frequency (GHz)
K-band	1.13 – 1.67	18.00 – 26.50
X-band	2.40 - 3.75	8.00 – 12.50
C-band	3.75 – 7.50	4.00 – 8.00
L-band	15.00 – 30.00	1.00 – 2.00
P-band	30.00 – 100.00	0.30 – 1.00

**Table 2.1** SAR bands, wavelengths, and frequency (Ortiz, 2017)

In civilian spaceborne SAR missions, the most used bands are L-band, C-band, and X-band (Barbieri & Lichtenegger, 2005). Each of these bands owns its specific characteristics in forest stand parameters, which are essential for the geohazard related research. In general, sensors with higher frequency and shorter wavelengths, such as C- and X-band have higher spatial resolutions. X-band sensors only receive the backscatter signals from the leave-top layer of the canopy. C-band microwave only can penetrate through canopy top leaves and scattered by small branches. While L-band, having lower frequency and longer wavelength, is less influenced by the vegetation, has the capability to penetrate through the canopy, and receive backscattered signals from the trunk and the main branches (**Figure 2.3**). As those above-mentioned SAR systems operate in the wavelength of centimeter to decimeter levels, they can acquire information almost without the consideration of meteorological conditions and solar illumination (Balmer & Hartl, 1998).

The spaceborne SAR satellite always follow a fixed trajectory around the Earth at an altitude ranging from 500 to 800 km. Therefore, the SAR satellite has two orbit directions: ascending, refers to the movement of the satellite from the south to north; and descending, refers to the movement of the satellite from the north to south. This feature makes it possible for SAR satellites to view the same area from two different geometries (**Figure 2.4**).

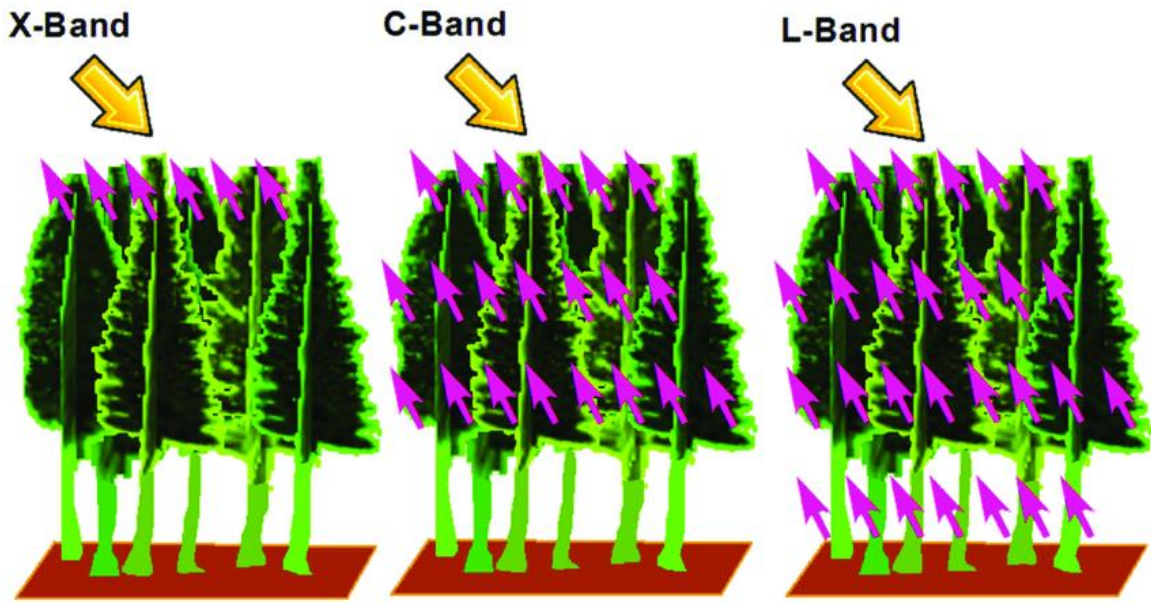


**Figure 2.3** Diagram of vegetation penetration capability among X-, C- and L-band sensors (Pham et al., 2019)

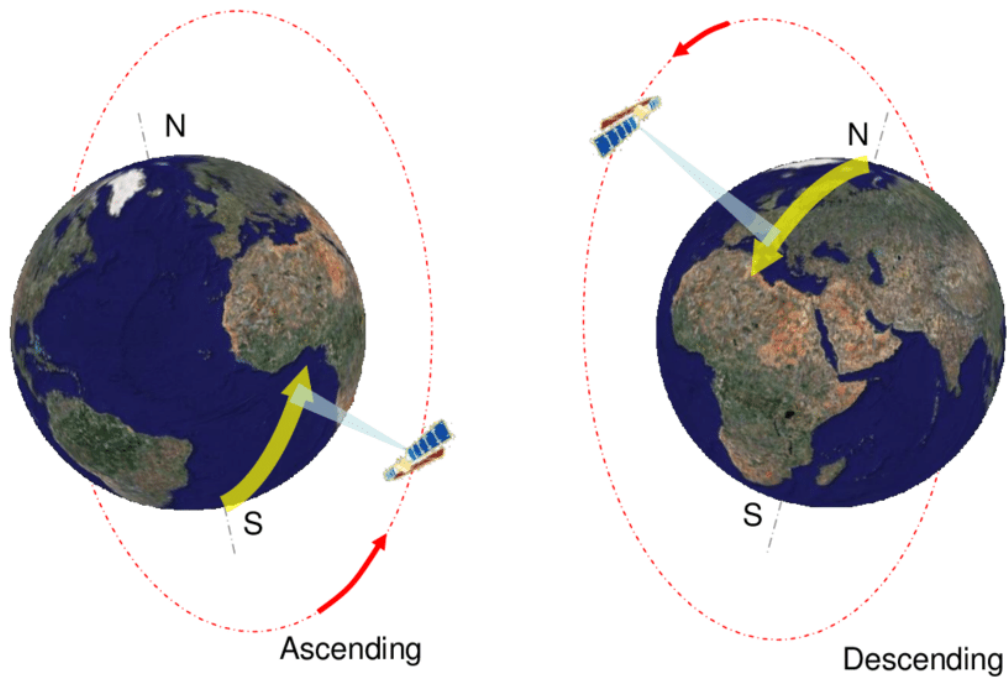


**Figure 2.4** Illustration of ascending and descending spaceborne SAR satellite geometries (Capes et al., 2009)

The revisiting time refers to the temporal period between a SAR sensor's first and second imaging the same area with the same geometry. Out of various purposes of operation, different SAR satellites have different revisiting times. But in general, starting from the launch of ERS-1 in 1992 to Sentinel-1b in 2015, the revisiting has been decreased from 35 days to minimum 6 days. **Figure 2.5** listed the common SAR satellites' launch date, revisiting time, and operation wavelengths.

Due to the curvature of different geomorphologies on Earth's surface, distortion is inevitably existing in spaceborne SAR imaging. On a SAR image, the forms of distortions appear differently.

Once slopes tilt toward the sensor, an increase in the backscattered energy will brighten the corresponding pixels on the SAR image. Such effect is foreshortening. While the slopes tilt away from the sensor, a decrease in the backscattered energy will darken the corresponding pixels. Such effect is called shadowing. In some circumstances, the slope exceeds the radar off-nadir angle, so the scatterers are imaged reversely and superimposed over other areas. Therefore, the top of the slope is imaged first and seems to be closer to the sensor than the lower part of the slope. Such phenomenon is called layover effect (**Figure 2.6**).

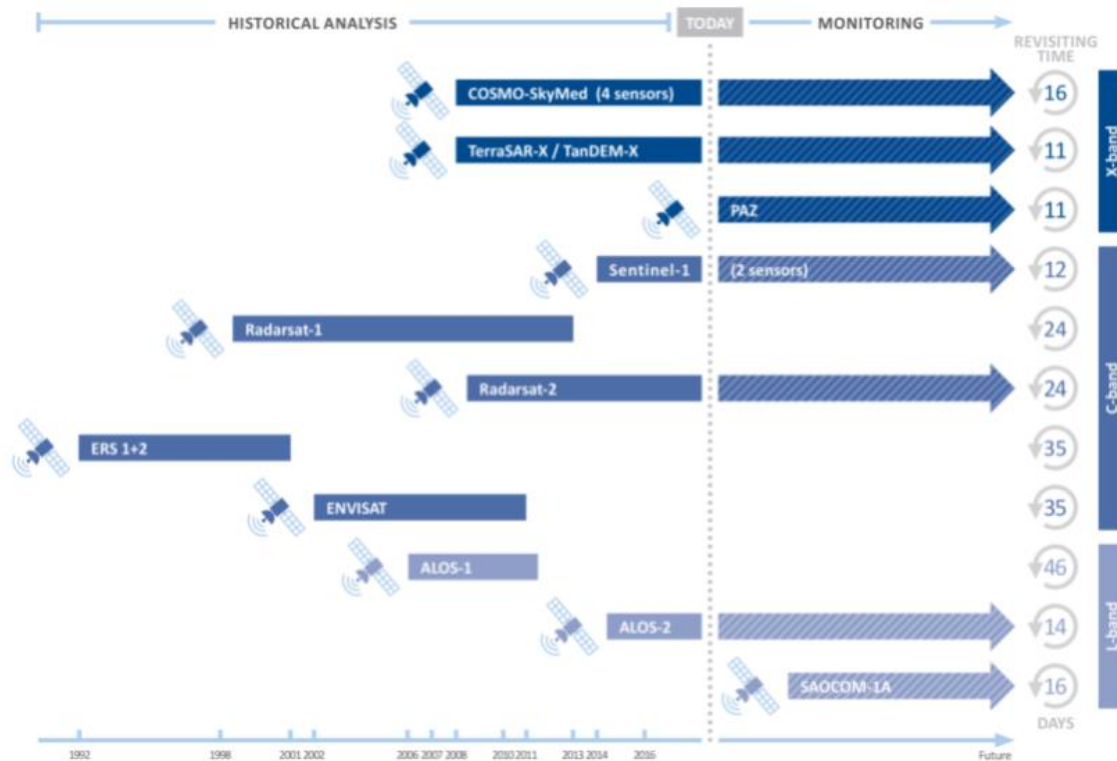


**Figure 2.5** Past and current SAR satellites used for historical analysis and ongoing monitoring (source: <https://site.tre-altamira.com/company/our-technology/#sar-imagery> )

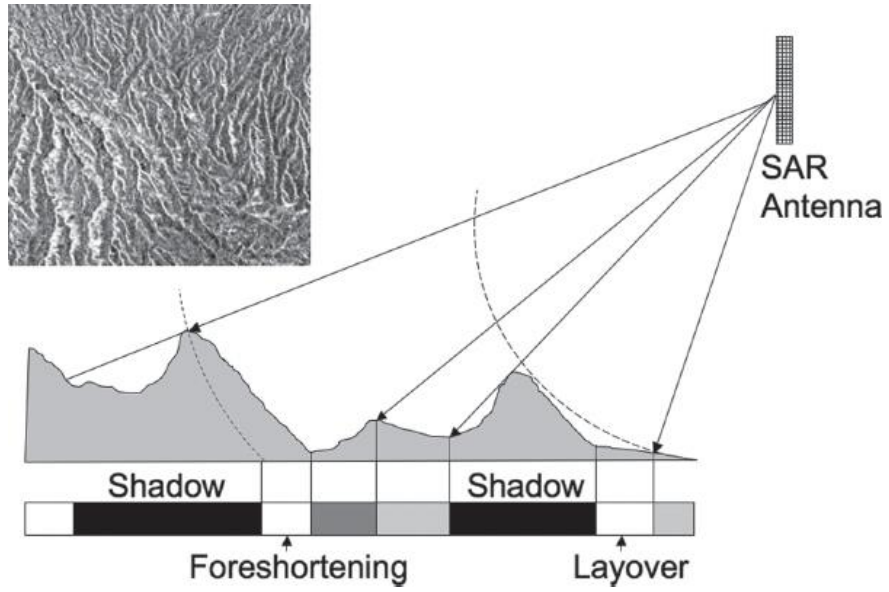


**Figure 2.6** Foreshortening, shadow, and layover of SAR imaging

### 2.3. SAR Interferometry (InSAR) and Differential InSAR (DInSAR)

Interferometric Synthetic Aperture Radar (InSAR) is an effective way to measure changes in land surface altitude. This method was firstly introduced by Gabriel & Goldstein (1988), but the research of interferometry could be dated back to early 1970s (Richman, 1971).

InSAR is the study of “subtraction calculation” of phase and amplitude signal contained in the same pixel collected by two SAR images sensed at different times and observing slightly different locations (Gabriel et al., 1989; Massonnet & Feigl, 1998, Bamler & Hartl, 1998, Rosen et al., 2000). It accomplishes high-accuracy measurements over large areas by the application of SAR phase signal contained in each pixel. The product derived from interfering between two SAR images (master-slave SAR images) is called interferogram.

The main goal of interferometry processing is to extract the component that related to the displacements and then to remove or minimize others. Therefore, Differential InSAR (DInSAR) has been introduced to retrieve the ground displacements between the two SAR acquisitions (**Figure 2.7**). DInSAR has been widely applied in different areas of research, including subsidence, landslides, heritage sites, volcanic activities, mining activities, tectonic movements, glacier movements and earthquake-induced deformations.

Here presents an application of DInSAR in the study of Earth Science. An earthquake (M=7.3) occurred in Qinghai Province, China on 21 May 2021 (UTC). Four days after, the newly acquired ALOS-2/PALSAR-2 data was used to measure the crustal deformation caused by this earthquake by researchers from Geospatial Information Authority of Japan. **Figure 2.8** shows the interferogram, and **Figure 2.9** shows the distribution of displacement in the line-of-sight direction between satellites and surface.

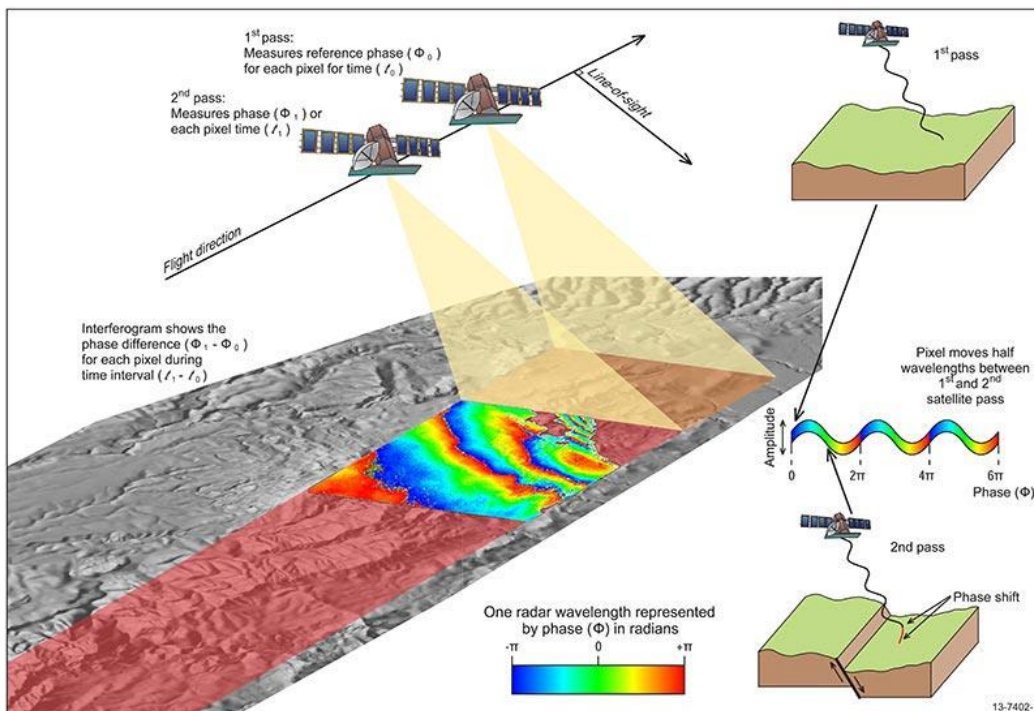


**Figure 2.7** Schematic picture of SAR differential interferometry (source: <https://www.ga.gov.au/scientific-topics/positioning-navigation/geodesy/geodetic-techniques/interferometric-synthetic-aperture-radar> )



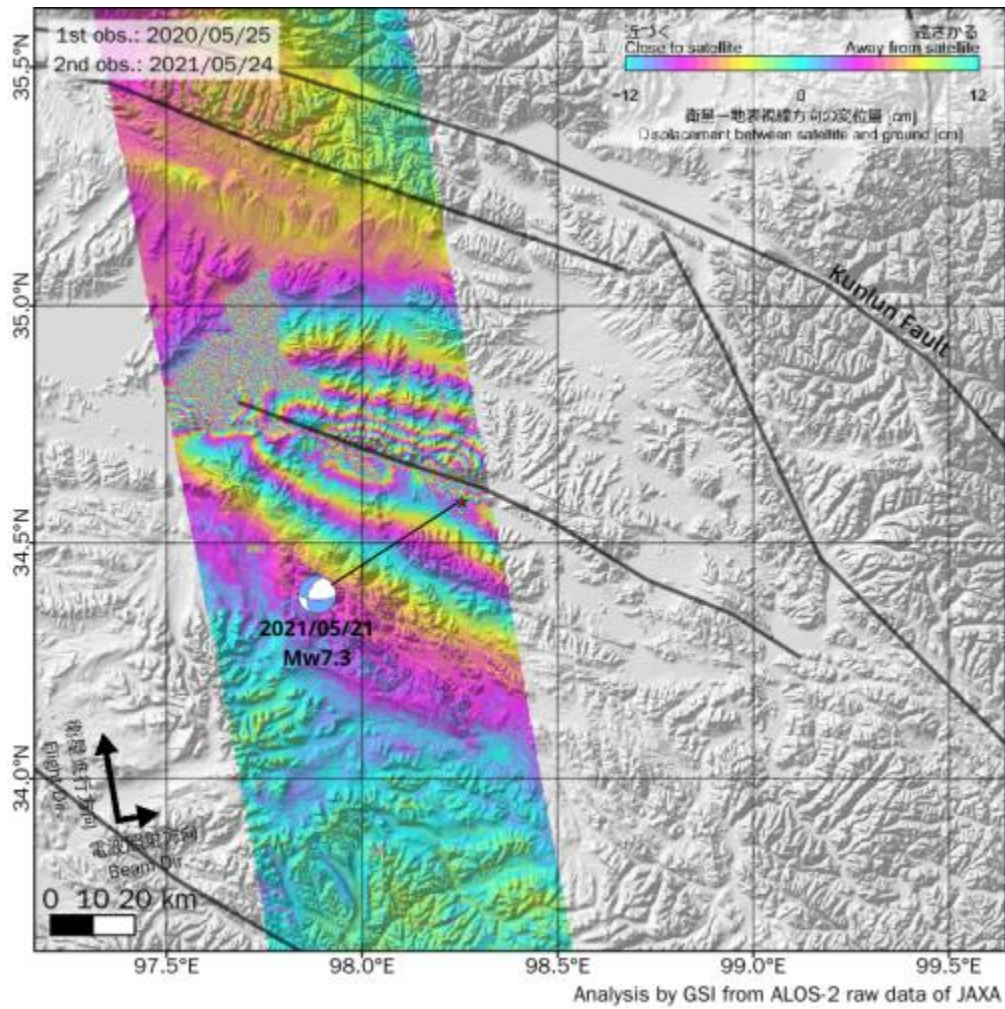


**Figure 2.8** Interferogram of the Qinghai earthquake (source: <https://www.gsi.go.jp/cais/topic20210521-e.html> )

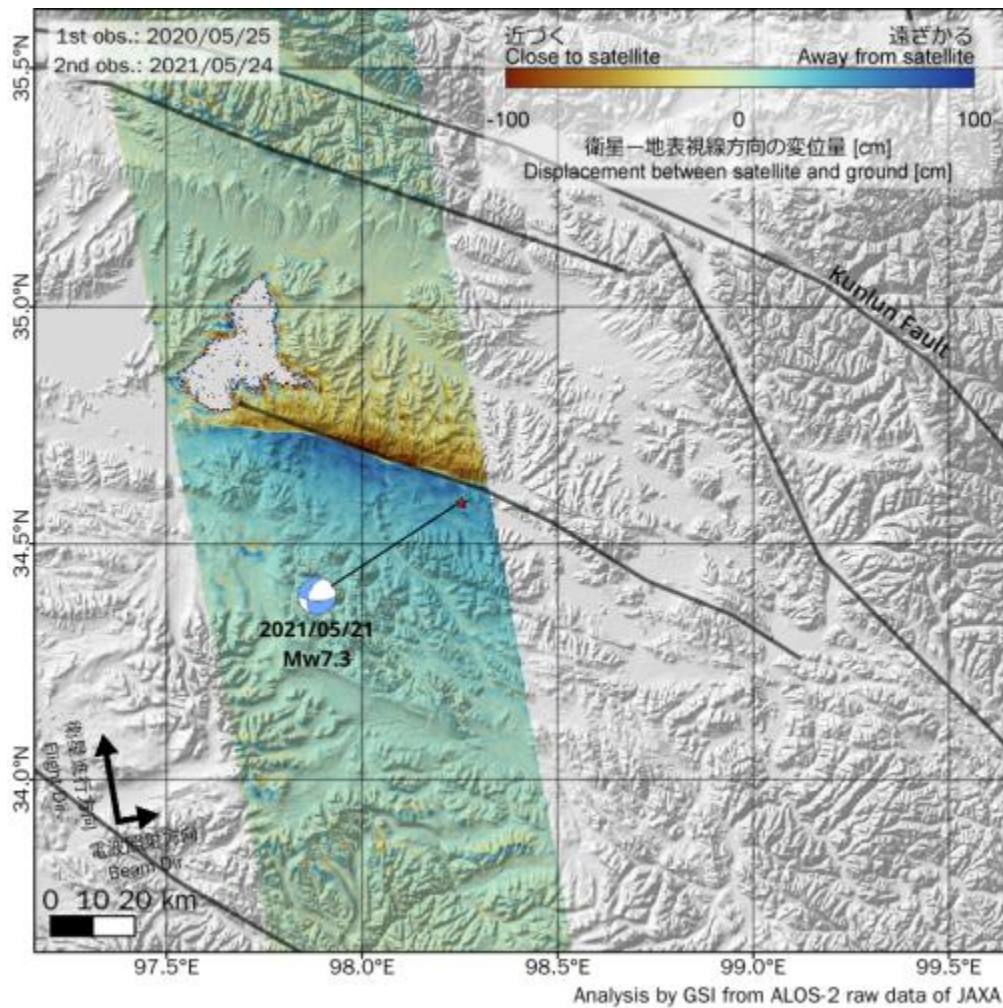


**Figure 2.9** Distribution of displacement in the line-of-sight direction between satellites and surface (source: <https://www.gsi.go.jp/cais/topic20210521-e.html> )

## 2.4. Persistent Scatterers InSAR (PSI) and SqueeSAR™ Method

Traditional single-pair DInSAR method has been demonstrated to be useful in various fields, but its limitations of atmospheric effects and the spatiotemporal decorrelation phenomena have slowed down the improvement of the usage in scientific research and applications (Massonnet & Feigl, 1998; Ferretti et al., 2001; Colesanti et al., 2003; Hooper et al., 2004).

To overcome the shortcomings of the single-pair DInSAR, new technique named as Persistent Scatterers Interferometry (PSI) was developed and introduced in the early 2000s. The core solution that PSI provides is the application of multi-temporal SAR interferometry (usually more than 30, 20 minimum) that allows the calculation of PS displacement time series, and then to eliminate the atmospheric noise after estimation. A series of interferograms is produced only related to one master image. As the number of SAR images in the stack increases, the quality of the estimation of the deformation of the PS points enhances (Crosetto et al., 2016). Different from the conventional DInSAR processing, the amplitude information is used for the selection of the candidate PS according to their reflectivity in the very first step. Phase information is still used as the indicator of the target-sensor distance.

The final result of PSInSAR processing is a time series of measurement of displacement of each of the selected PS targets along the line-of-sight direction respect to the reference point selected in very first steps.

Persistent Scatterers InSAR method includes numerous different approaches to derive the multi-temporal analysis to enhance the accuracy of ground movement measurement developed by the scientific community worldwide. These techniques are later proven to be successfully in monitoring deformation over a long period, are suitable for surface deformation inversion. **Table 2.2** lists some of those methods.

Name of the Method	References
Permanent Scatterers Interferometry SAR (PSInSAR™)	Ferretti et al. (2000) and Ferretti et al. (2001)
Small Baseline Subset (SBAS)	Berardino et al. (2002), Lanari et al. (2004), Casu et al. (2006) and Lanari et al. (2007)
Stanford Method for Persistent Scatterers (StaMPS)	Hooper et al. (2004) and Hooper (2008)
Interferometric Point Target Analysis (IPTA)	Werner et al. (2003) and Strozzi et al. (2006)
SqueeSAR™	Ferretti et al. (2011)

**Table 2.2** Major PSI based methodologies

The PS data processed and interpreted is all processed using SqueeSAR™ in this PhD research.

SqueeSAR™ method is an enhancement based on the PSInSAR™ technique to provide measurements taking advantage of low reflectivity, but coherent, homogenous natural targets defined as “Statistically Homogenous Pixels (SHP)” as “distributed scatterers (DS)” together with the permanent scatterers over area of interest (“squeezing”, Ferretti et al., 2011). It provides the possibility of point extraction over bare soils, uncultivated areas, debris, etc. In this way, the number of extracted points increases, therefore, to provide denser measurement compared to PSInSAR™ processing.

The selection of the DS uses a space adaptive filter called “DespeckS” based on the K-S statistical test (Ferretti et al., 2011). All the pixels will be searched using self-adapt filter with changing search radius, and those pixels either with good coherence, homogeneity or with strong reflectivity will be selected as candidate DS and PS, respectively. After the selection of candidate PS and DS using different methods, the PS/DS will candidates be processed using the standard PSInSAR™ method.

From the application point of view, given the same stack of SAR images, compared to conventional PSInSAR processing, SqueeSAR™ processing significantly improves the point density, therefore enhances the usage, reliability, and precision of the multi-temporal InSAR processing in non-urban areas (Ferretti et al., 2011; Lagios et al., 2013).

## Chapter 3. Case Study 1: Low-land Permafrost Region of Northeastern China

### 3.1. Study Area

The study area is in the Beian-Sunwu-Heihe area, Lesser Khingan Mountains in northern Heilongjiang Province, China (**Figure 3.1**). It is the southern margin of the Eurasian permafrost region. The permafrost distributed in this region represents the second largest of permafrost region in China (Ran et. al., 2012) and it is the only high-latitude permafrost region in China. These low-land permafrost patches are more sensitive to climate and environmental changes and have been degrading in the recent years since 2000 till now. As shown in **Figure 1.3**, the low PFI value makes the exploration of permafrost degradation a challenge as the permafrost distribution in this region is not continuous, more “island-like” at a small scale.

In this region, the Beian-Heihe expressway locates at the center of the study area. It was planned and built between 1997 and 2000 originally. Various incidents including sink holes and slope instabilities that can be related to the melting of permafrost has been reporting since 1999. Subsequently, one section of the road was even repaved to a nearby ridge because of the permafrost degradation. Then during 2009 to 2011 this expressway had a reconstruction and expansion engineering project. The original two-lane expressway had been expanded into four lanes. The electricity power facilities are located at the east of the study area. And some small villages and settlements are spotted around in the study area.

The geomorphology of the study area is mainly low hilly terrain with fluvial deposits distributed among the whole study area. The land cover is highly mixed, including cold temperate coniferous forests at higher altitudes, deciduous forests at lower altitudes, moss grasslands growing on lower surface, peatland and swampland near the draining channels and floodplains. Additionally, there are also a large proportion of agriculture fields, man-made infrastructures, and bare soils.

The climate in the study area has shown strong seasonal characteristics. The winters are usually long, cold, and dry, with short, hot, and humid summers. The precipitation mainly occurs during summers and early falls (Shi et al., 2014; Wang et al., 2019). According to the air temperature data from 1960 to 2019 of Sunwu National Meteorological Station that located inside the study area, the overall air temperature of the study area is increasing (Shan et al., 2020), and the rate of increment of air temperature in this dataset is the highest in northeastern China (Shan et al., 2015) From Wang et al. (2019), the annual average minimum air temperature from 1980 to 2018 records a 3.3 times rate of the annual average minimum air temperature in northeast China.

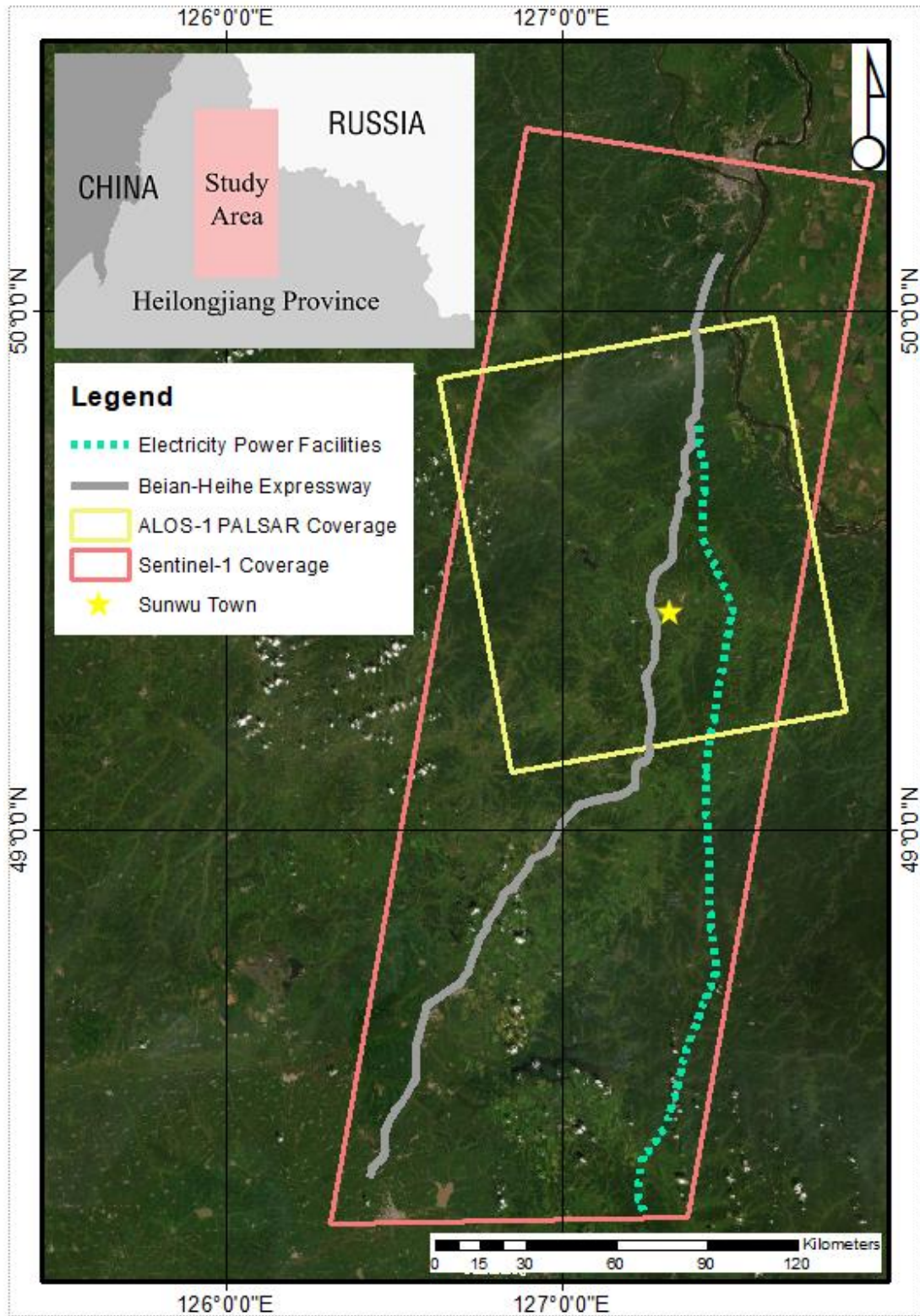


Figure 3.1 Study area

## 3.2. Data and Processing Methods

### 3.2.1. Sentinel-1

#### 3.2.1.1. Data

The Sentinel-1 mission is the European Radar Observatory for the Copernicus joint initiative of the European Commission (EC) and the European Space Agency (ESA).

Currently, the Sentinel-1 constellation is composed by two satellites, Sentinel-1A (launched in April 2014) and Sentinel-1B (launched in April 2016), and will include Sentinel-1C and Sentinel-1D for longer operation from 2022 (Sentinel-1C, <https://www.airbus.com/newsroom/press-releases/en/2020/08/sentinel1c-radar-antenna-has-spread-its-wings-for-the-first-time.html>). Working during day and night regardless of the weather conditions, the Sentinel-1A and Sentinel-1B share the same orbital plane and designed and operated with an effective minimum revisiting time of 12 days (6 days in Europe), which benefits the development of earth observation especially using SAR interferometric methods (**Figure 3.2**).

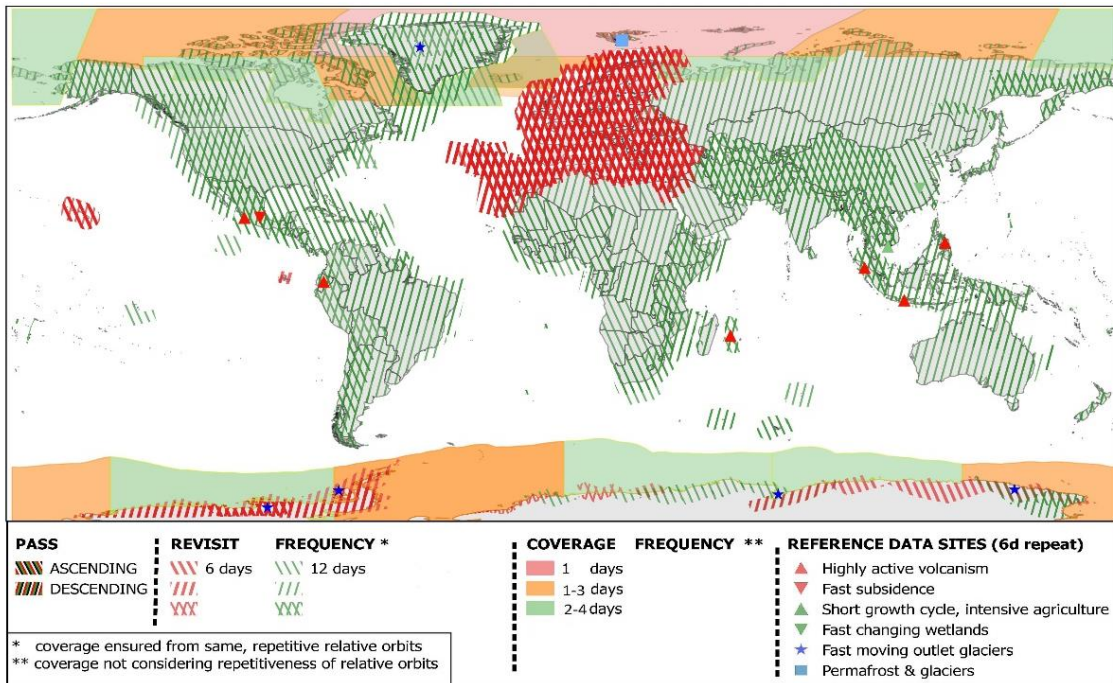


**Figure 3.2** Sentinel-1 Constellation Revisit & Coverage Frequency (source: <https://sentinels.copernicus.eu/web/sentinel/missions/sentinel-1/observation-scenario> )

As the first of the five missions that ESA is developing for the Copernicus initiative, Sentinel-1 SAR products are freely accessible online, regardless of the type of user. It has been proved as a powerful tool in a wide range of applications including global landmass monitoring (agriculture, forestry, etc.), land cover classification and change monitoring, geology/engineering geology (seismology, coastal erosion, volcanology, landslide hazard and urban subsidence monitoring, assessment and mapping, open pit mining, oil and gas extraction, underground civil engineering projects, etc.), oceanography, cryosphere monitoring. It should be noted that the rapid data dissemination of hour level and short revisit cycles of Sentinel-1 benefits emergency response/civil protection users including United Nations International Charter on Space and Major Disasters in emergency situations, including flood mapping, earthquake, volcano eruptions and landslides, as mentioned in previous chapters.

Sentinel-1's major EO instrument is C-band SAR with the operating wavelength of 5.55 cm and 5.405 GHz center frequency operating in four polarizations (VV, HH, HV, VH) and in four modes including Strip Map (SM), Interferometric Wide Swath (IW), Extra-Wide Swath (EW) and Wave modes (**Figure 3.3**). The final delivered products are in four formats, including Level-0 Raw, Level-1 Single Look Complex, Level-1 Ground Range Detected and Level-2 Ocean (**Figure 3.4**). In this PhD research, Level-1 Single Look Complex product in IW mode is selected following to the research objective (**Table 3.1**). This product provides up to 250 km coverage and down to 5 m spatial resolution. **Table 3.2** and **Figure 3.5** have shown the acquisition geometry of the used Sentinel-1 data in this study.

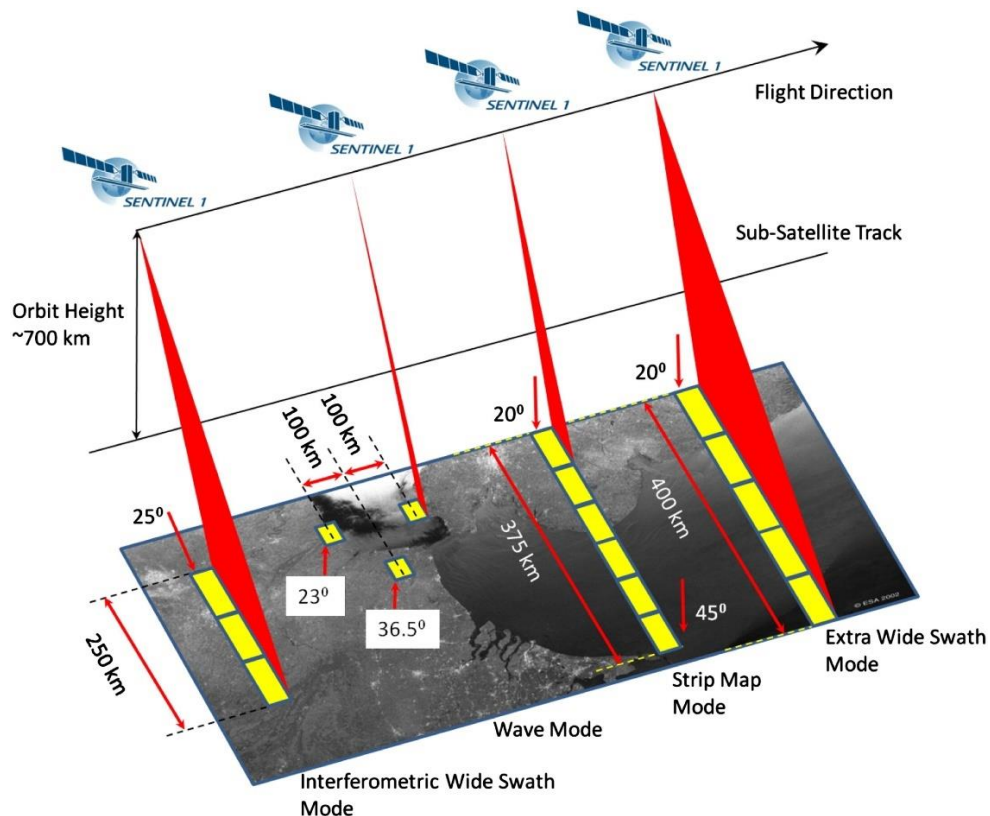


**Figure 3.3** Sentinel-1 imaging modes (source: <https://sentinel.esa.int/web/sentinel/missions/sentinel-1/data-products> )



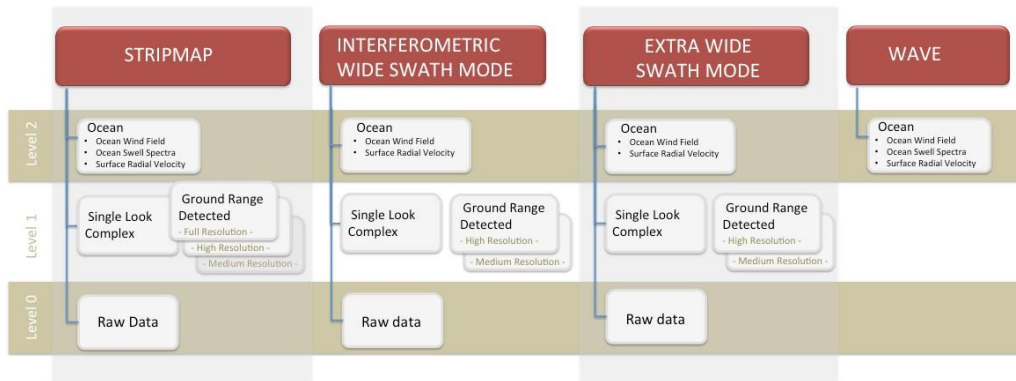


**Figure 3.4** Diagram of Sentinel-1 core products (source: <https://sentinel.esa.int/web/sentinel/missions/sentinel-1/data-products> )

Satellite and product	Wavelength	Geometry	Sensor mode	Track	Number of Scenes
Sentinel-1 SLC	5.55 cm	Descending	IW	105	90

**Table 3.1** Sentinel-1 imaging information

<b>Line of sight angle</b>	$\Theta = 36.21^\circ$	$\Delta = 11.94^\circ$	
<b>Line of sight versors</b>	$V = 0.807$	$N = -0.122$	$E = 0.578$

**Table 3.2** Acquisition geometry of Sentinel-1

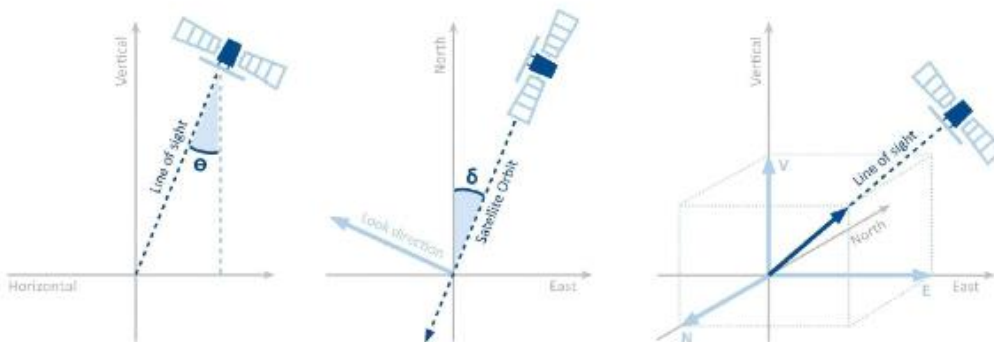


**Figure 3.5** Acquisition geometry diagram of Sentinel-1

The launching of Sentinel-1 sensors initiated a new perspective and opportunity for SAR/InSAR applications due to its increased revisit frequency, high reliability, high consistency of long time series data archive, global geographical coverage, rapid data dissemination, and regularity of acquisitions with respect to previous C-band missions of ERS-1/2 and ENVISAT operated by ESA and RADARSAT-1/2 operated by Canadian Space Agency (Raspini et al., 2018; Raspini et al., 2019; Torres et al., 2012).

### 3.2.1.2. Processing methods

In this research, Sentinel-1 SAR data is used in SqueeSAR™ processing to reveal the ground displacement in the study area, and then the Sentinel-1 differential interferograms are processed using “DIAPASON InSAR Sentinel-1 TOPSAR (IW/EW)” (DIAPASON S-1) algorithm on the Geohazards Thematic Exploitation Platform (GEP), as shown in **Figure 3.6**.

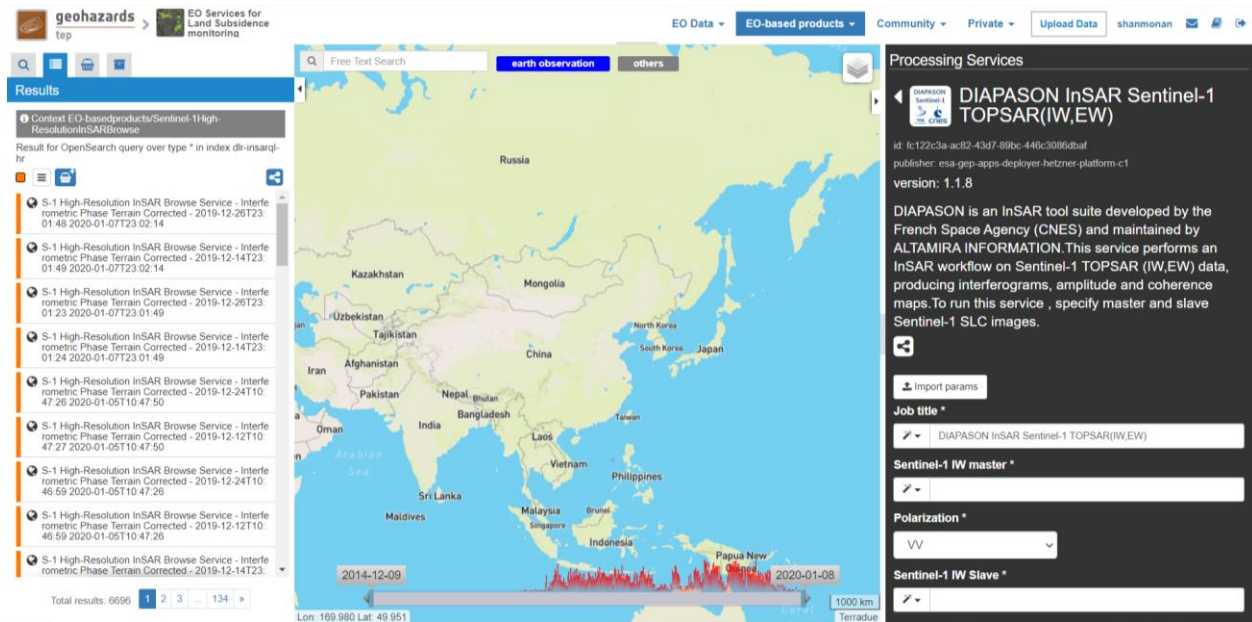


**Figure 3.6** GEP, EO Services for Land Subsidence monitoring thematic application and DIAPASON S-1 processing interface.

The Geohazards Thematic Exploitation Platform (GEP, <https://geohazards-tep.eu>) is a cloud-based platform developed and operated by Terradue s.r.l. (<https://www.terradue.com/portal/>), a leading company in internet infrastructures for earth sciences. Aiming to provide innovative responses to the needs of the geohazards community, and to support the exploitation of satellite earth observation (EO) methods for geohazards specifically, GEP provides a series of ready-to-use satellite EO data and on-demand, systematic processing services to expert users. Additionally, GEP also provides the authority of cloud-based satellite EO data computing algorithm development to service providers (stakeholders) to address the challenges of monitoring tectonic areas globally and the need of massive computing power.

To expert users, GEP provides full access to Copernicus Sentinel-1/2/3, Landsat-8 and as to 70+ TB of historical EO data (including ERS and ENVISAT), conditional access to Pleiades and Spot 6/7 high-resolution optical imageries, ASTER Level-1T Precision Terrain Corrected Registered At-Sensor Radiance products, and some specific data collections from various of EO missions, including JAXA's ALOS/ALOS-2, ASI's COSMO-SkyMed, and DLR's TerraSAR-X.

To access the services, researcher should prepare a proposal that specifies the research objective, project duration and processing services to the administrators. The administrators will grant the processing and data authority based on the presented proposal.

In this research, the DIAPASON S-1 algorithm under the “EO Services for Land Subsidence monitoring thematic application” is chosen to conduct the Sentinel-1 differential interferometry processing. DIAPASON is an InSAR tool suite developed by the French Space Agency (CNES) and maintained by TRE-Altamira. This service will help in the production of Sentinel-1 differential interferograms, amplitude and coherence maps.

Google Earth Engine (GEE) was applied to retrieve the time series of MODIS 8-day Land Surface Temperature (LST) and ERA5 monthly precipitation data, then to compare with the SqueeSAR™ displacement time series results.

### 3.2.2. ALOS PALSAR

#### 3.2.2.1. Data

The Advanced Land Observing Satellite (ALOS) was developed by the Japan Aerospace Exploration Agency (JAXA), and was successfully launched on 24 January 2006, and ended its operation on 22 April 2011. It follows the Japanese Earth Resources Satellite-1 (JERS-1) and Advanced Earth Observing Satellite (ADEOS) and utilizes advanced land-observing technology.

The ALOS had mounted three remote sensing instruments: the Panchromatic Remote Sensing Instrument for Stereo Mapping (PRISM) for digital elevation mapping, the Advanced Visible and Near Infrared Radiometer type 2 (AVNIR-2) for precise land coverage observation, and PALSAR (the Phased Array type L-band Synthetic Aperture Radar) that has been used for day-and-night and all-weather earth observation (source: [https://www.eorc.jaxa.jp/ALOS/en/about/about\\_index.htm](https://www.eorc.jaxa.jp/ALOS/en/about/about_index.htm) ).

The ALOS provides a systematic EO strategy that assures emergency observations first, then to meet the planned routine monitoring. To generate differential interferograms, the data acquired from ALOS PALSAR instrument is used in this research. The ALOS PALSAR data is collected at four different modes, including Global Fine Beam (Single/Dual polarization), Arctic Fine Beam (Dual polarization), Regional Fine Beam Polarimetric and ScanSAR modes (**Figure 3.7**). According to the research objective, data collected in Global Fine Beam (Single/Dual polarization) mode is used in the generation of differential interferograms and SqueeSAR™ processing. **Table 3.3** lists the ALOS PALSAR general characteristic information.

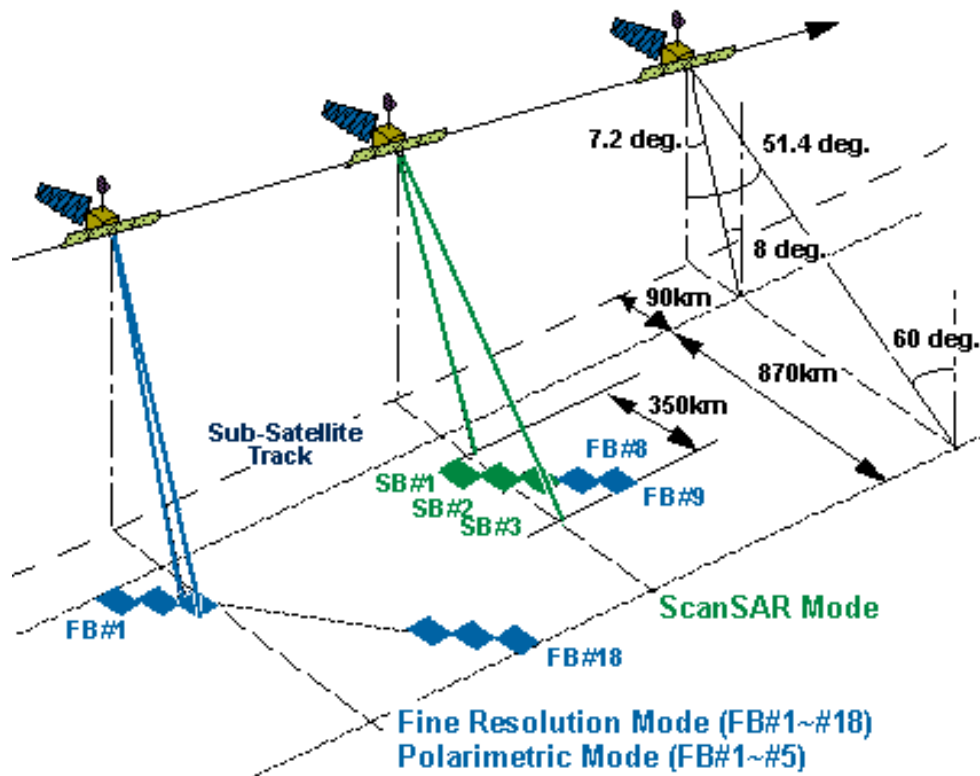


**Figure 3.7** ALOS PALSAR imaging modes

ALOS PALSAR	FBS mode	FBD mode
Spatial Resolution	10 m	20 m
Center Frequency	L-band (1.27 Ghz)	
Swath Width	70 km	
Off-Nadir Angle	34.3°	
Polarization	HH or VV	HH+HV or VV+VH

**Table 3.3** ALOS PALSAR FBS and FBD products

The observation strategy of ALOS aims to provide spatially and temporally consistent, multi-seasonal, on a repetitive basis monitoring globally. **Table 3.4** lists the ALOS PALSAR data imaging dates of this study. From that table, the ALOS PALSAR data used in this study is acquired all year long in all 4 seasons from the summer season of 2007 to the winter season of 2010.

Year	Imaging Dates (Month/Day, mm.dd)				
2007	06.10	07.26	09.10	12.11	
2008	01.26	04.27	06.12	12.13	
2009	01.28	06.15	07.31	09.15	12.16
2010	01.31	03.18	05.03	06.18	
	08.03	09.18	12.19		

**Table 3.4** ALOS PALSAR data used in this study.

**Table 3.5** lists the basic imaging information of ALOS PALSAR data used in this study. **Table 3.6** and **Figure 3.8** indicates the acquisition geometry of ALOS PALSAR data.

Satellite and sensor	Wavelength	Geometry	Sensor mode	Track	Number of Scenes
ALOS PALSAR	23.61 cm	Ascending	P7/F7	423	20

**Table 3.5** Imaging information of ALOS PALSAR data

<b>Line of sight angle</b>	$\Theta = 38.88^\circ$	$\Delta = 8.68^\circ$	
<b>Line of sight versors</b>	$V = 0.778$	$N = -0.095$	$E = -0.62$

**Table 3.6** Acquisition geometry of ALOS PALSAR data



**Figure 3.8** Acquisition geometry diagram of ALOS PALSAR

Various products derived from ALOS have been widely applied for scientific research and application usage, including natural resource management, disaster monitoring and damage mitigation, and regional development and planning. Notably, researchers have used ALOS PRISM data to produce a data set of global digital surface model (DSM) with high horizontal resolution of approximately 3 meters (Tadono et al., 2014).

### 3.2.2.2. Processing methods

In this research, the SAR data (both ALOS PALSAR and Sentinel-1) was first processed using SqueeSAR™ approach. Then to reduce the false estimation of the displacement velocity of the extracted PS/DS targets from the annual thawing and freezing processes of the seasonal frozen soil that will interfere the LOS velocity results, the time series of the displacement was extracted using a mask of 3 whole annual cycles, rather than the 3.5 years of SAR image acquisitions used in the previous SqueeSAR™ processing. Later by the interpretation of the displacement by multiple criteria including local topography, geomorphological information, and land cover (change), the spatial distribution map of permafrost degradation in Sunwu area was confirmed and then combined with the stepwise subsequential wrapped differential interferograms processed using GEP and ENVI-SarScape, the seasonal variation of the permafrost degradation patches was further studied. The detailed workflow is shown in **Figure 3.9**.

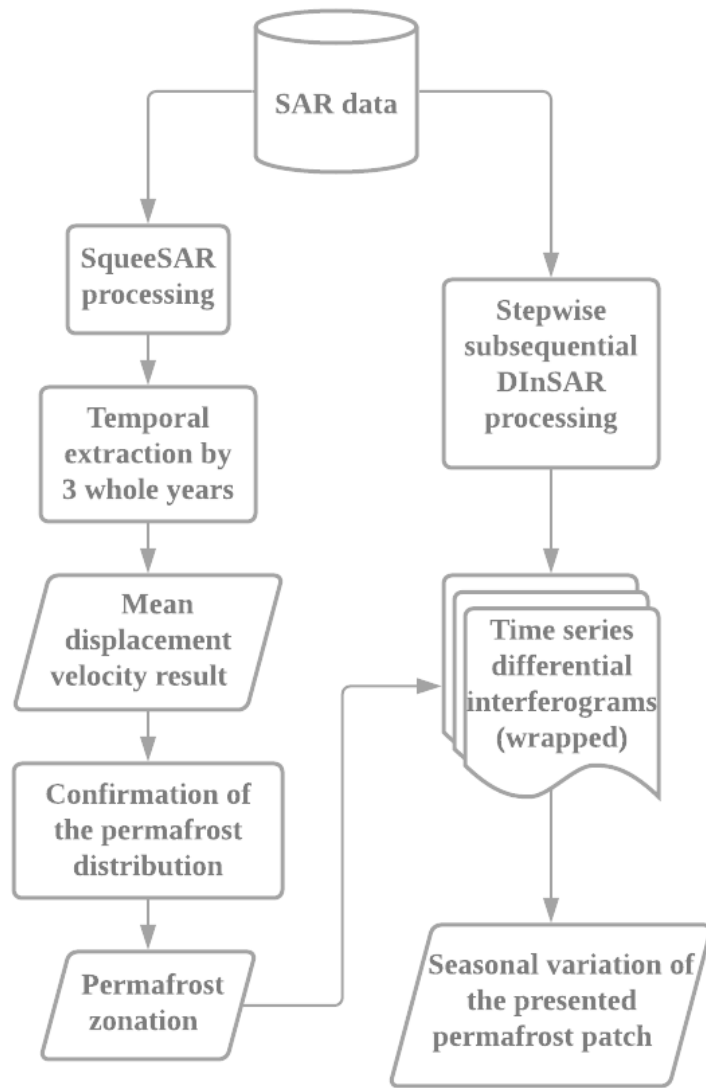


Figure 3.9 The presented workflow

### 3.3. Results

#### 3.3.1. ALOS PALSAR SqueeSAR™ processing

The ALOS PALSAR SqueeSAR™ processing result (temporally clipped from December 2007 to December 2010) is shown in **Figure 3.9**. A threshold of 0.7 was used to improve the coherence of the extracted PS/DS targets. Over 770000 PS/DS targets were extracted from a small area of over 10000 km<sup>2</sup>. The deformation rates range from 40 mm/year to -40 mm/year approximately. **Table 3.7** shows the SqueeSAR™ processing information of the ALOS PALSAR SAR data stack. According to the statistics of the displacement results, we consider that those PS/DS with deformation rate lower than -20 mm/year as a condition for the mapping of the permafrost distribution, shown in orange and red colors in the legend. The blue features in the **Figure 3.10** refers to the deformation towards the ALOS PALSAR sensor. Such positive rate could be referring an actual uplifting in flat areas, or subsidence events considering the local topography. The slope direction displacement map was not produced as the cosine values (up-down, east-west, north-south) of the PS/DS targets were not obtained from the data processing and error reduction considerations.

Combined with local topography, geomorphological information, and land cover (change), 27 polygons inside the red dash line from the **Figure 3.11** refers to the possible permafrost distribution in the study area. Only three of those delineated degrading permafrost patches are not located nearby flat fluvial deposits and they have shown a more slightly velocity of the subsidence. Then three permafrost patches (two of them locate in/near the fluvial deposit, one locates on a slope) were further analyzed in detail, shown in **Figure 3.12** to **Figure 3.17**. The studied points are shown in numeric numbers in the figures and then the displacement time series were plotted in the following figure.

In order to visualize the relationship between the permafrost degradation and the change of land surface temperature, MODIS 8-day land surface temperature time series was plotted together with the SqueeSAR™ displacement results. Clear seasonality effect can be observed from both time series of land surface temperature and the ground deformation. During the thawing months in spring and summer, the increasing land surface temperature initiated the ground deformation. The absorbed heat in the soil causes the thawing of the permafrost, causing the deformation. The ground deformation processes tend to be stable during the hottest seasons due to the equivalent of heat absorbing and emitting, and show uplifting because of the freezing processes when it comes to colder seasons eventually, shown as frost heaving in the field. However, when the accumulated absorbed heat is larger than the emitted heat, the melting process will be always more intensive than the freezing process. The subsidence during the thawing seasons will always be larger than the uplifting during the freezing seasons. Therefore, the long-time ground deformation will be regarded as a key indicator for visualizing the degradation of permafrost.

According to the research of Wang (2012), the increase rate of agricultural land use in the Sunwu County has reached to a rate of 118%, and the land use of gardening has reached 727%, meanwhile the size of forest land cover decreased by 22%. Through the high-resolution optical images in **Figure 3.12**, **Figure 3.14** and **Figure 3.16**, the conversion of forest land cover to agricultural land cover is clearly visualized. Such intensive land cover change in this region could be an important reason of observed permafrost degradation. **Figure 3.12** and **Figure 3.14** have shown two examples of the deformation patches in the fluvial deposits near the rivers. As described in the last chapters, the land cover in these two locations had drastically changed from swampland into agricultural lands. Through the deformation time series shown in **Figure 3.13** and **Figure 3.15**, the acceleration of the deformation rate in these two examples could be related to the human activities.



Sensor Name	Operator	Operation time	Duration (in months)	Wavelength	Geometry	# Of scenes
ALOS PALSAR	JAXA	2007.6 – 2010.12	43	L-band, 23.6 cm	Ascending	20

**Table 3.7** ALOS PALSAR SqueeSAR™ processing information

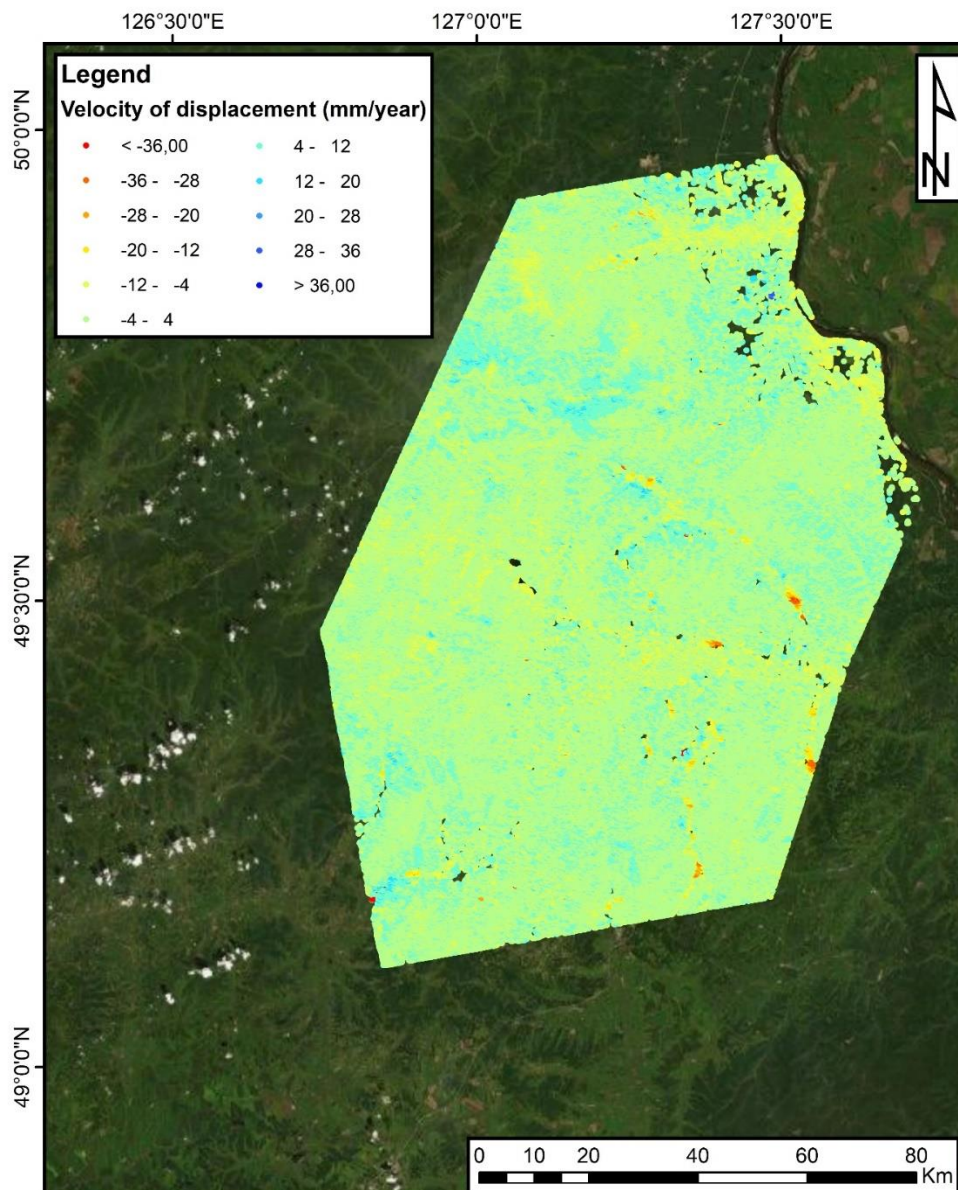


**Figure 3.10** ALOS PALSAR SqueeSAR™ Mean Displacement Velocity Results (period: December 2007 to December 2010, 17 ALOS PALSAR images used)

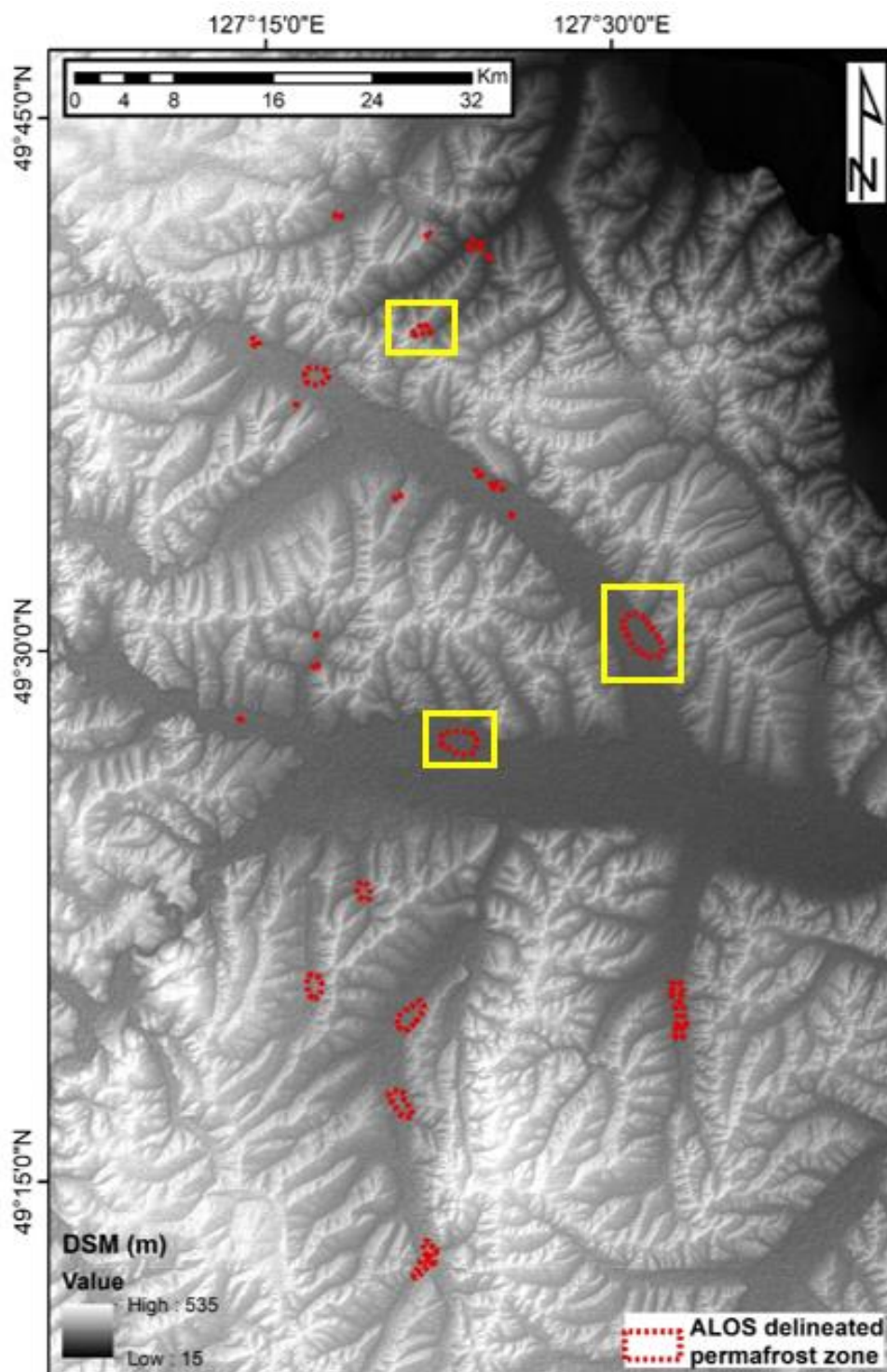


**Figure 3.11** Delineated possible permafrost zones using ALOS PALSAR SqueeSAR™ processing results. The analyzed permafrost patches are labeled in yellow rectangles, shown in the following figures in detail.

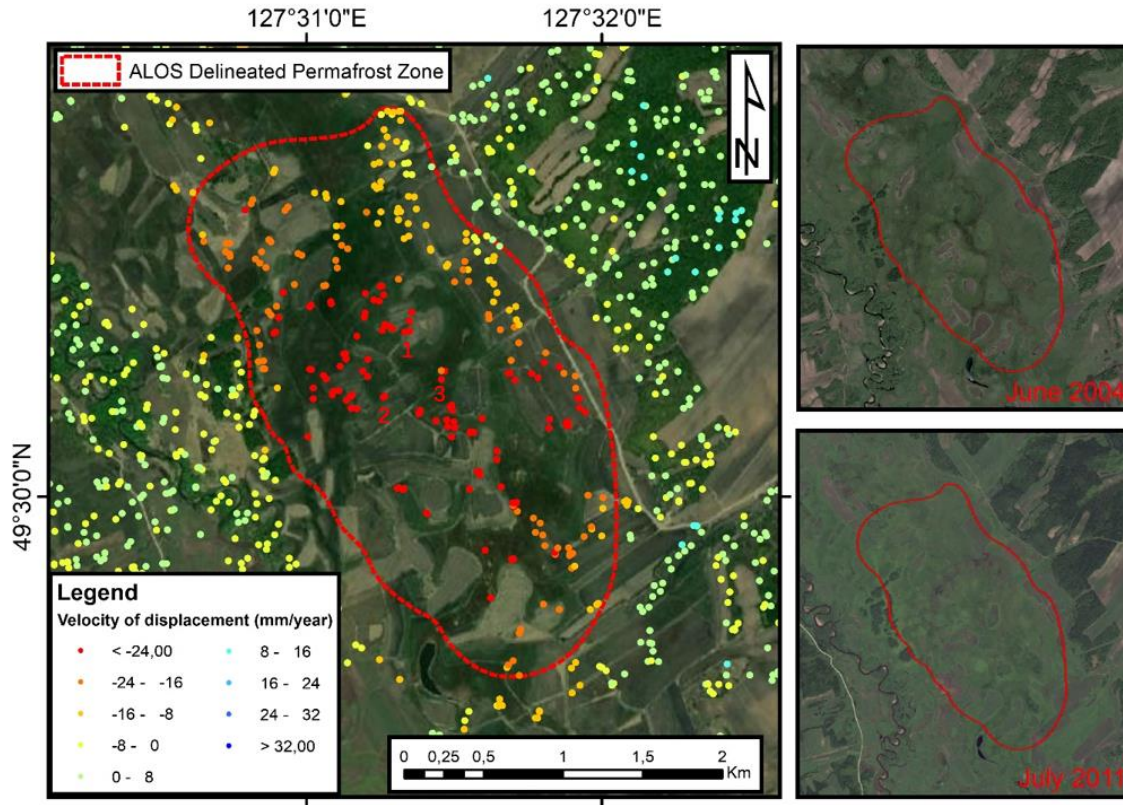


**Figure 3.12** Analyzed degrading permafrost patch No.1 and the high-resolution optical imagery of June 2004 and July 2011 near the permafrost patch No.1. The plotted points are shown in numbers.

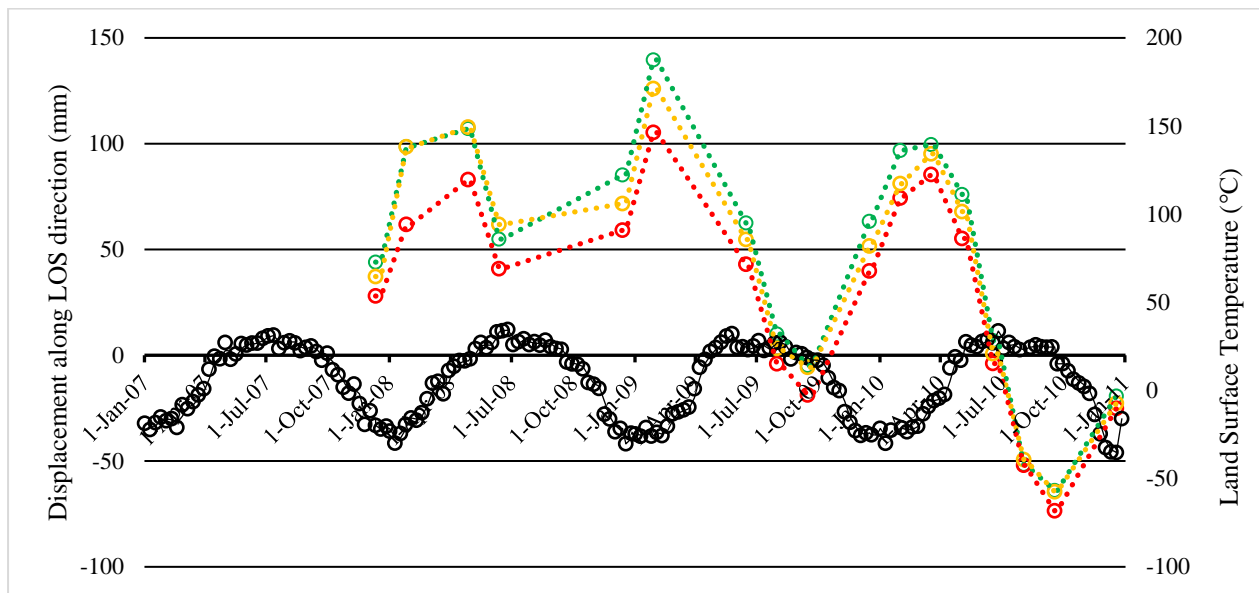


**Figure 3.13** The displacement time series of the studied points in permafrost patch No.1

Point ID	1	2	3
Longitude	127.524157	127.521051	127.524208
Latitude	49.504294	49.503699	49.504327
Point type	DS	DS	DS
Altitude (meter a.s.l.)	239.5	239.7	239.9
Deformation velocity along line-of-sight direction (mm/year)	-7.8	-6.7	-4.9
Coherence	0.96	0.98	0.97

**Table 3.8** The interferometric parameters of the studied points

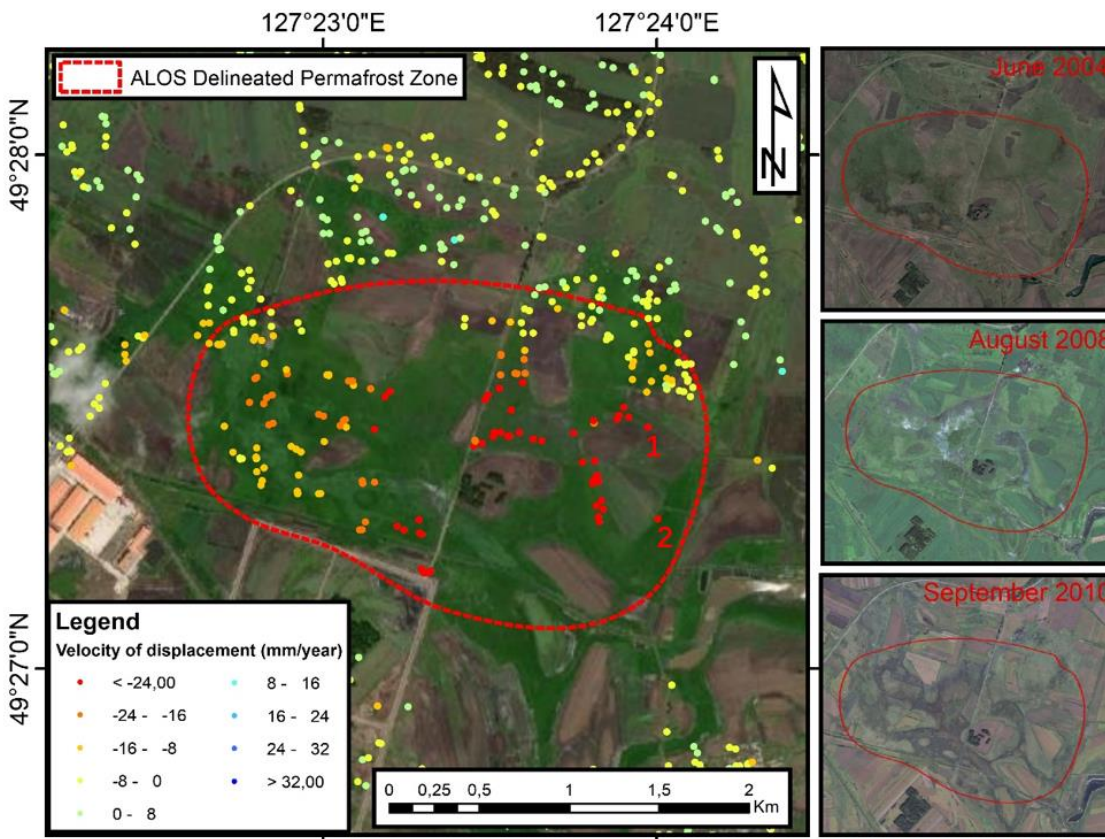


**Figure 3.14** Analyzed degrading permafrost patch No.2 and the high-resolution optical imagery of June 2004, August 2008, and September 2010 near the permafrost patch No.2. The plotted points are shown in numbers.

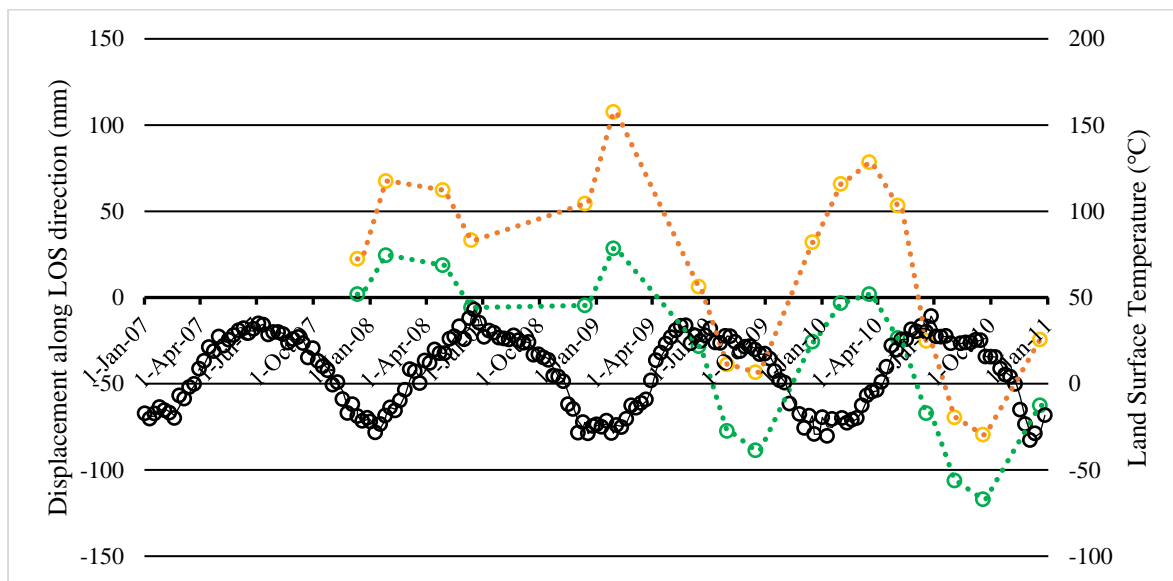


**Figure 3.15** The displacement time series of the studied points in permafrost patch No.2

<b>Point ID</b>	1	2
<b>Longitude</b>	127.399569	127.399976
<b>Latitude</b>	49.457816	49.454856
<b>Point type</b>	DS	DS
<b>Altitude (meter a.s.l.)</b>	238	239.4
<b>Deformation velocity along line-of-sight direction (mm/year)</b>	-20.6	-7.7
<b>Coherence</b>	0.96	0.90

**Table 3.9** The interferometric parameters of the studied points

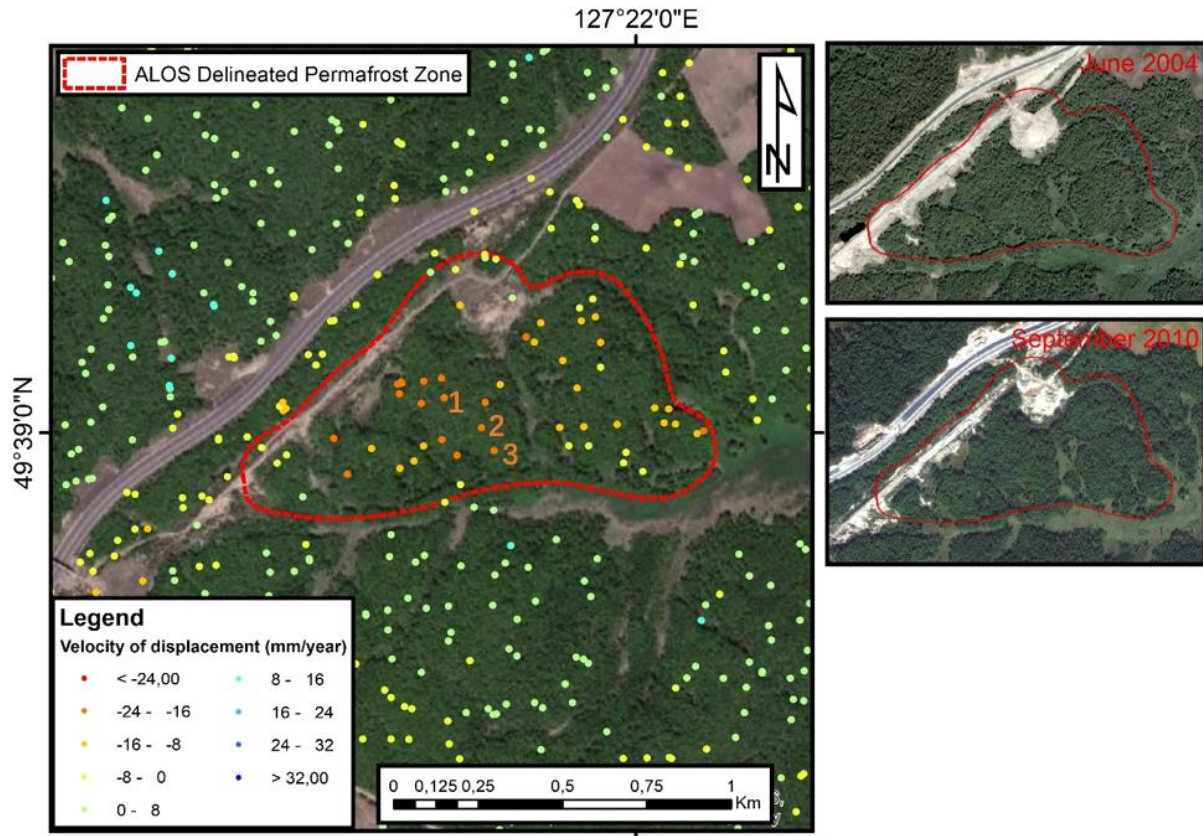


**Figure 3.16** Analyzed degrading permafrost patch No.3 and the high-resolution optical imagery of June 2004 and September 2010 near the permafrost patch No.3. The plotted points are shown in numbers.

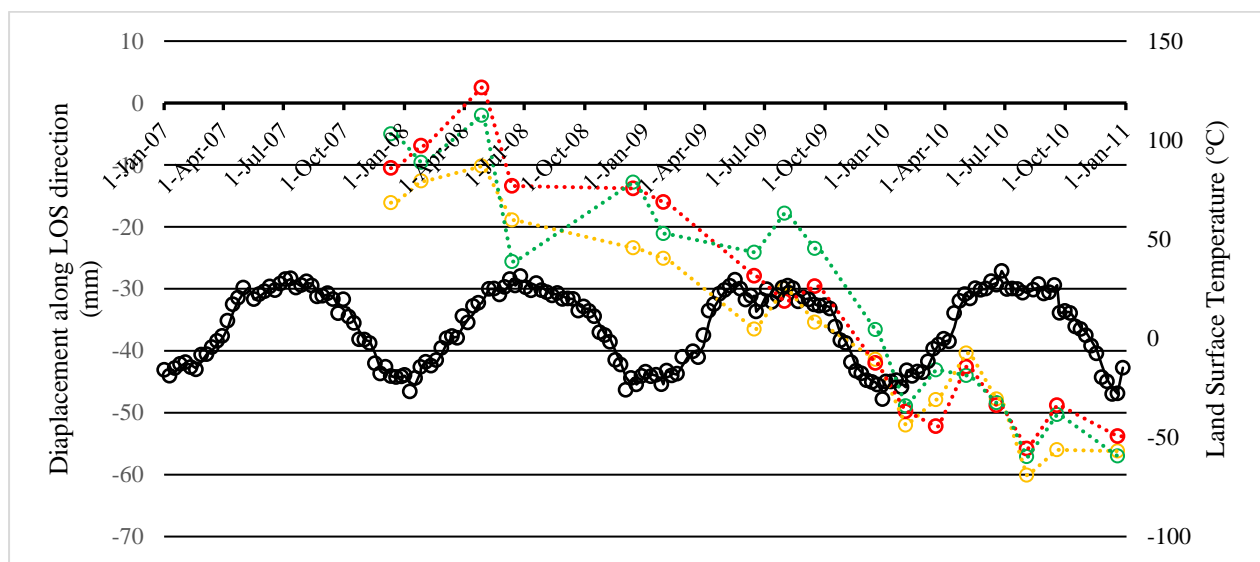


**Figure 3.17** The displacement time series of the studied points in permafrost patch No.3

Point ID	1	2	3
Longitude	127.361552	127.362530	127.362876
Latitude	49.650619	49.650084	49.649702
Point type	DS	DS	DS
Altitude (meter a.s.l.)	289.7	278.6	274
Deformation velocity along line-of-sight direction (mm/year)	-17	-18	-16.2
Coherence	0.96	0.96	0.98

**Table 3.10** The interferometric parameters of the studied points

The third example (**Figure 3.16**, **Figure 3.17** and **Table 3.10**) shows that how the permafrost degradation will influence the construction of infrastructures, although the deformation time series did not appear to have strong seasonality as the former examples that locate in the fluvial deposit areas. In the high-resolution optical remote sensing images two linear features are observed in the center of the image. One of them clearly indicates the Beian-Heihe expressway as shown in **Figure 3.1**. But the second abandoned plan was related to the ground deformation caused by the permafrost degradation. During this research I interviewed the local planners of the Beian-Heihe expressway. The expressway was originally planned to be constructed to the southeast of today's expressway during late 1990s, but that project was suspended because years later the deformation of the slope was observed by the clear cracks on the road surface. Then subsequently, through a series of geo-physical researches, strong electro resistivity signals underground that represents the existence of permafrost was observed underneath the slope and the original planned route then the permafrost was then dug out. According to the SqueeSAR™ results the deformation of the slope is clearly mapped.

### 3.3.2. ALOS PALSAR differential interferometry processing

Besides the SqueeSAR™ processing of ALOS PALSAR, differential interferograms were then produced. The processing of differential interferograms follows the rule of temporal subsequential processing. For instance, the interferometry pairs are SAR image A – SAR image B; SAR image B – SAR image C; SAR image C – SAR image D and so on, where A, B, C, and D refer to subsequential imaging dates in the corresponding image stack of each sensor.

The reason of the creation of the differential interferograms is firstly to provide a clear way to show the ground deformation in the subsequential image acquisitions. Secondly, due to the possible modelling error during the SqueeSAR™ multi-temporal InSAR processing because of the only one master SAR image in the center of the whole imaging period, the differential interferograms will provide another way to verify the SqueeSAR™ processing results. Two summer differential interferograms and two winter differential interferograms of ALOS PALSAR sensor were chosen from the full dataset of subsequential processing of differential interferograms and presented due to the limited volume of the context. **Figure 3.18 to Figure 3.21** shows the clipped smaller study area used in the following analysis and four ALOS PALSAR differential interferograms processed by ENVI SarScape software. The information of these processing is shown in **Table 3.11**.

The ALOS PALSAR SqueeSAR™ displacement time series results were clipped by same temporal interval as the differential InSAR processing and shown from **Figure 3.18 to Figure 3.21**. The annual velocity of the displacement of the extracted PS/DS points rather than the actual displacement are listed in the legend. ALOS PALSAR DInSAR results have shown clear fringes that represent the seasonal deformation over fluvial deposit at local scale which is helpful for the further seasonality analysis. By the combination of the ALOS PALSAR SqueeSAR™ displacement time series results and the ALOS PALSAR stepwise differential interferograms, during the thawing seasons, the fluvial deposits occur severe deformation events. As contrast, the fluvial deposits occur uplifting events during the freezing seasons. But as ALOS PALSAR differential interferograms have shown, more fringes caused by the APS at the regional scale, rather than other reasons observed.

The processing results all indicate that compared to other geological and geomorphological sections, fluvial deposit, or floodplain is more favorable than other environments for permafrost degradation from 2007 to 2011 in Sunwu region. And due to the lack of PS/DS targets within some smaller watersheds, the ground deformation caused by permafrost degradation might have occurred there as well as the observed hotspots shown in **Figure 3.11**. And according to the consistency between the observed fringes and the clipped SqueeSAR™ results that clearly indicate the larger amplitude of subsidence during summer seasons and uplifting during winter seasons, it has been confirmed that the fluvial deposit is the favorable environment for the growth of seasonal frozen soil, as well as the permafrost degradation.

Sensors	Master image	Slave image	Season
ALOS	20171211	20080126	Winter
	20081213	20090128	Winter
	20090615	20090731	Summer
	20100618	20100803	Summer

**Table 3.11** Processing information of ALOS PALSAR differential interferogram



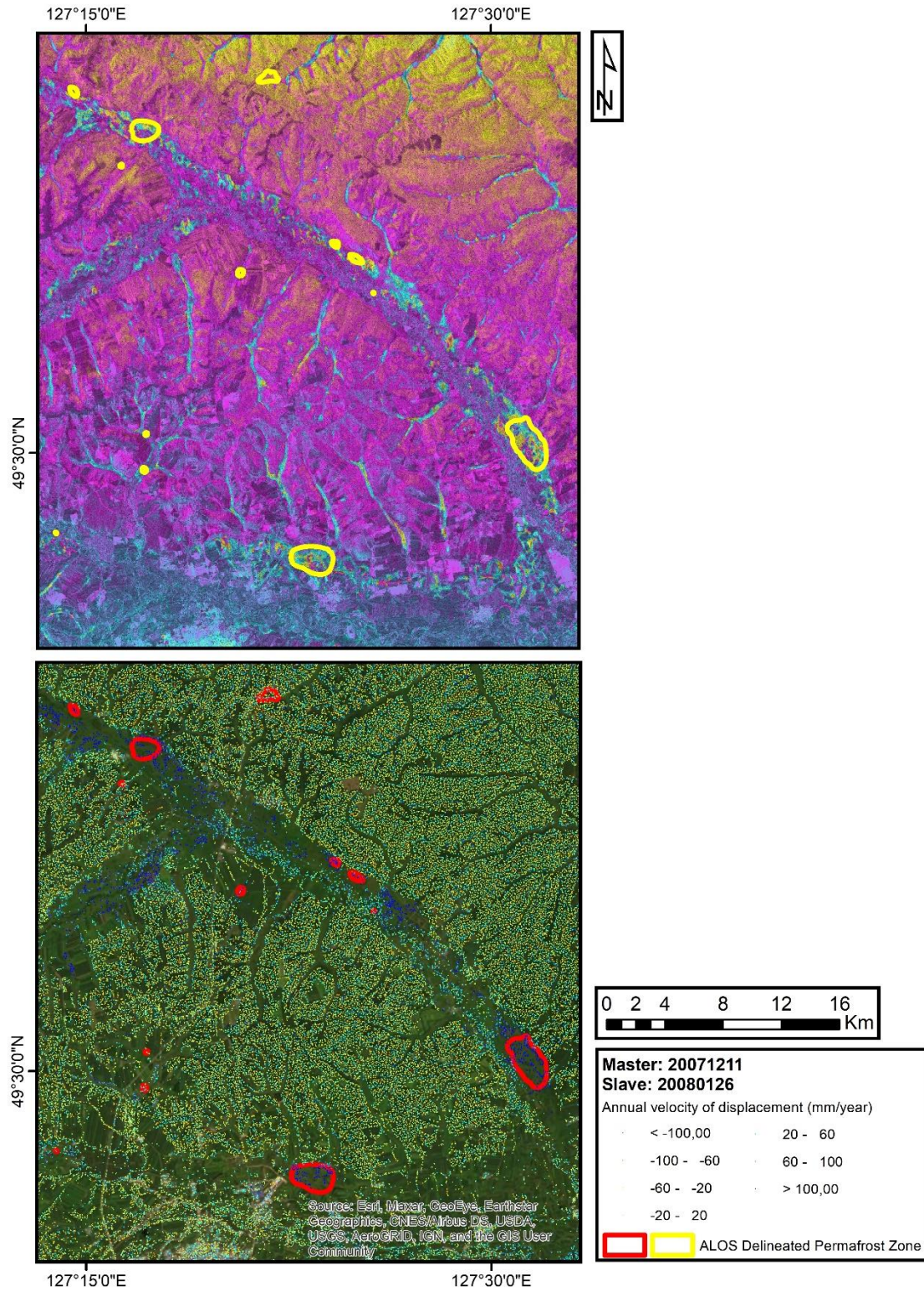


**Figure 3.18** 20071211-20080126 ALOS PALSAR differential interferogram and corresponding SqueeSAR™ results

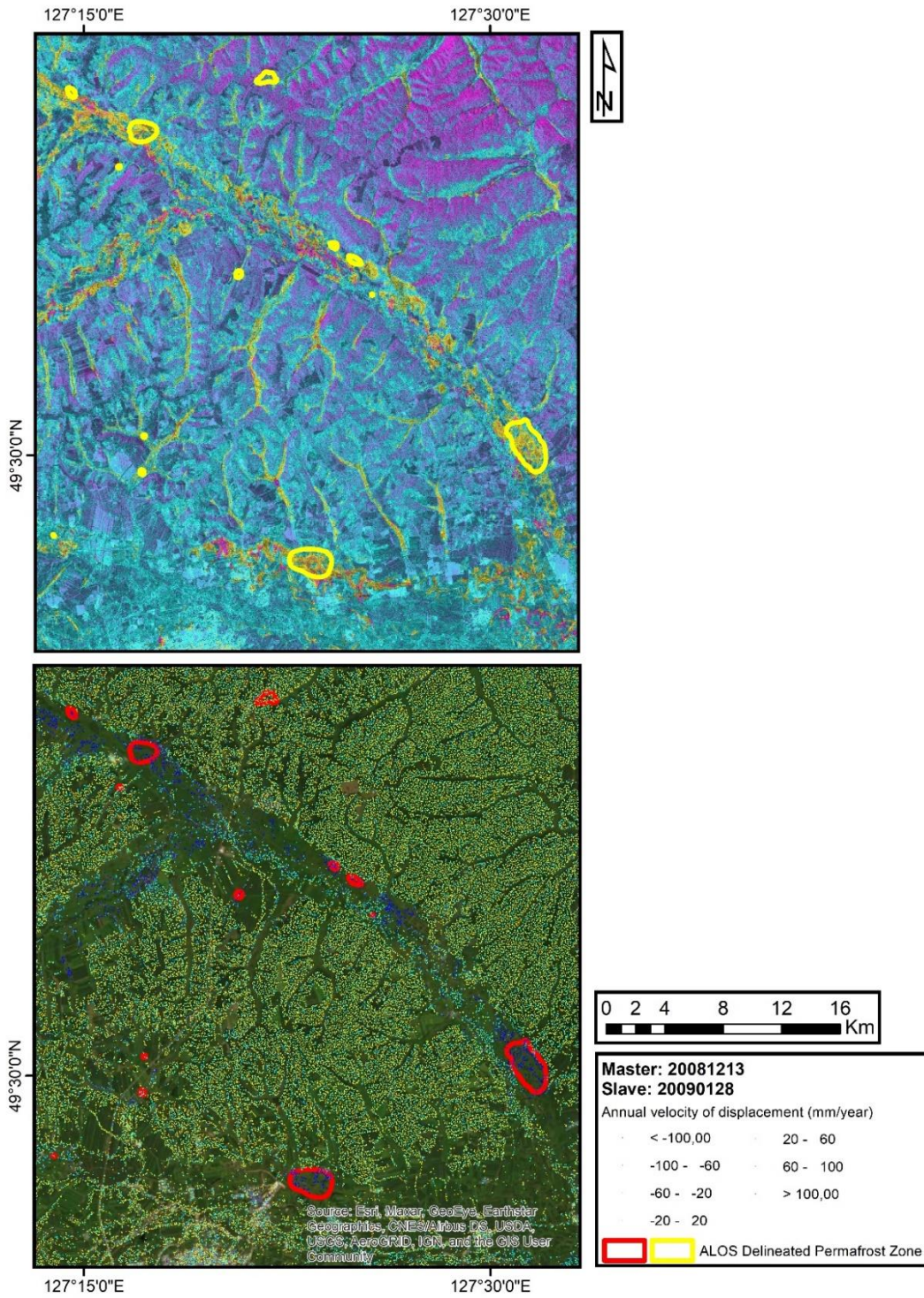


**Figure 3.19** 20081213-20090128 ALOS PALSAR differential interferogram and corresponding SqueeSAR™ results

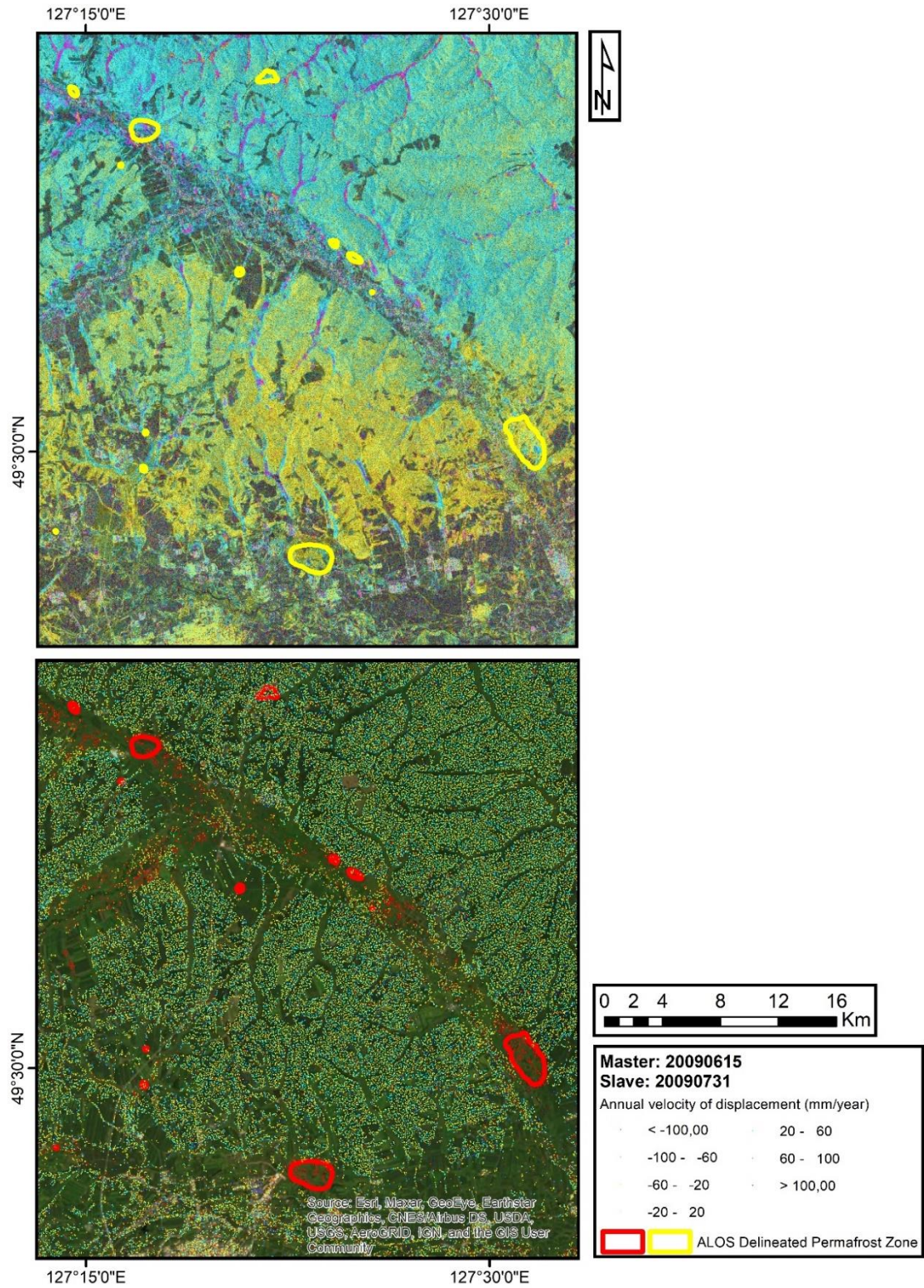


**Figure 3.20** 20090615-20090731 ALOS PALSAR differential interferogram and corresponding SqueeSAR™ results

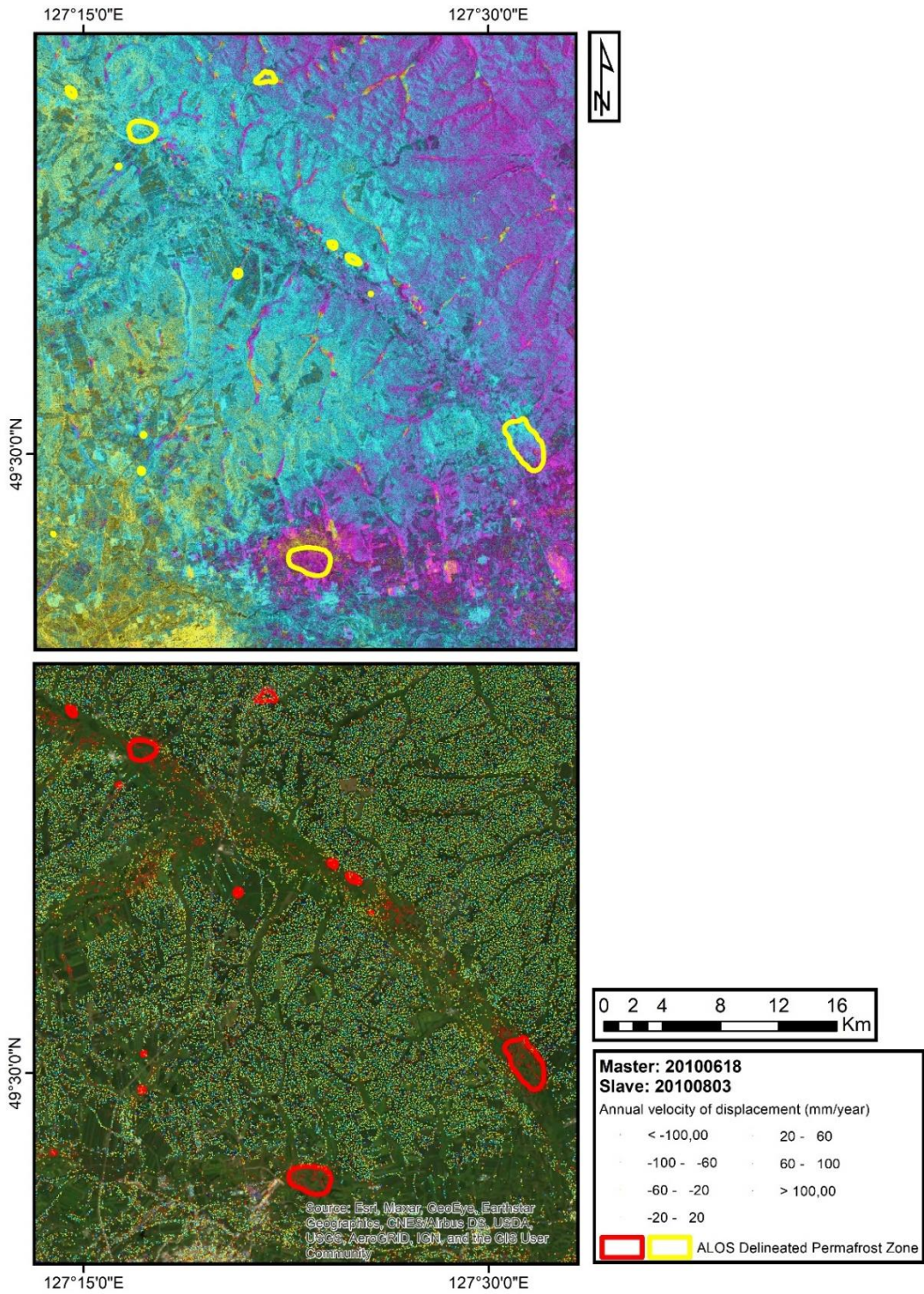


**Figure 3.21** 20100618-20100803 ALOS PALSAR differential interferogram and corresponding SqueeSAR™ results

### 3.3.3. Sentinel-1 SqueeSAR™ and differential interferometry processing

Then the Sentinel-1 SqueeSAR™ processing was conducted and temporally clipped from January 2016 to January 2019 and shown in **Figure 3.22**. The temporal baseline was set as three years as well as the ALOS PALSAR SqueeSAR™ processing. A low threshold of 0.3 was chosen to maintain as many PS/DS points as possible due to the limitation of penetration into forest canopy of the C-band sensor. Over 160000 PS/DS targets are extracted from an area of more than 40000 km<sup>2</sup>. **Table 3.12** shows the processing information of the Sentinel-1 SqueeSAR™ processing. The deformation rates range from 40 mm/year to -40 mm/year approximately. According to the statistics of the displacement results and to maintain the consistency of previous mapping, we consider that those PS/DS with deformation rate lower than -20 mm/year as a condition for the mapping of the permafrost distribution, shown in orange and red colors in the legend. The blue features in the **Figure 3.22** refers to the deformation towards the Sentinel-1 sensor. Such positive rate could be referring an actual uplifting in flat areas, or subsidence events considering the local topography. The slope direction displacement map was not produced as the cosine values (up-down, east-west, north-south) of the PS/DS targets were not obtained from the data processing and error reduction considerations.

Sensor Name	Operator	Operation time	Duration (in months)	Wavelength	Geometry	# Of scenes
Sentinel-1	ESA	2015.6 – 2019.1	42	C-band, 5.6 cm	Descending	90

**Table 3.12** Sentinel-1 SqueeSAR™ processing information

Although the coherence threshold was set to be a low value of 0.3 to maintain as many PS/DS as possible, the density of PS/DS in the Sentinel-1 SqueeSAR™ processing is significantly lower than the ALOS PALSAR SqueeSAR™ processing in nearly all land covers. Following the same strategy as described in **Figure 3.9**, it is nearly impossible to observe and map the deformation hotspot in a specific geological or geomorphological section or a specific land cover in the Sentinel-1 SqueeSAR™ processing.

Then similar to ALOS PALSAR, as described in the previous context, Sentinel-1 stepwise differential interferograms were produced using GEP. The processing information of the presented Sentinel-1 differential interferograms is listed in **Table 3.13**. **Figure 3.23** to **Figure 3.26** list the produced Sentinel-1 differential interferograms and the corresponding SqueeSAR™ result at the same temporal period. The Sentinel-1 differential interferograms produced using winter image pairs (**Figure 3.23** and **Figure 3.25**) have shown clear fringes than the summer pairs (**Figure 3.24** and **Figure 3.26**). The noisy salt and pepper effect from the differential interferograms produced using summer image pairs had increased the difficulty in the interpretation.

Sensors	Master image	Slave image	Season
Sentinel-1	20161230	20170111	Winter
	20171201	20171213	Winter
	20170722	20170803	Summer
	20180717	20180729	Summer

**Table 3.13** Processing information of Sentinel-1 differential interferogram

From the created Sentinel-1 differential interferograms of the freezing seasons, the locations of the clear fringes are very similar to the ALOS PALSAR differential interferograms. That may indicate the uplifting of the fluvial deposits during the freezing season has been continuing until the imaging time of Sentinel-1 sensor, which is ten years after the ALOS PALSAR sensor. Then it is possible to conclude that during thawing seasons the fluvial deposits may occur deformation even the Sentinel-1 summer differential interferograms could not provide such information. Such uplifting in freezing seasons and deformation in thawing seasons could be referring to the existence of seasonal active layer, but due to the lack of the PS/DS points from the Sentinel-1 SqueeSAR™ results, it is nearly impossible to confirm the existence of the permafrost layer underneath the seasonal active layer.

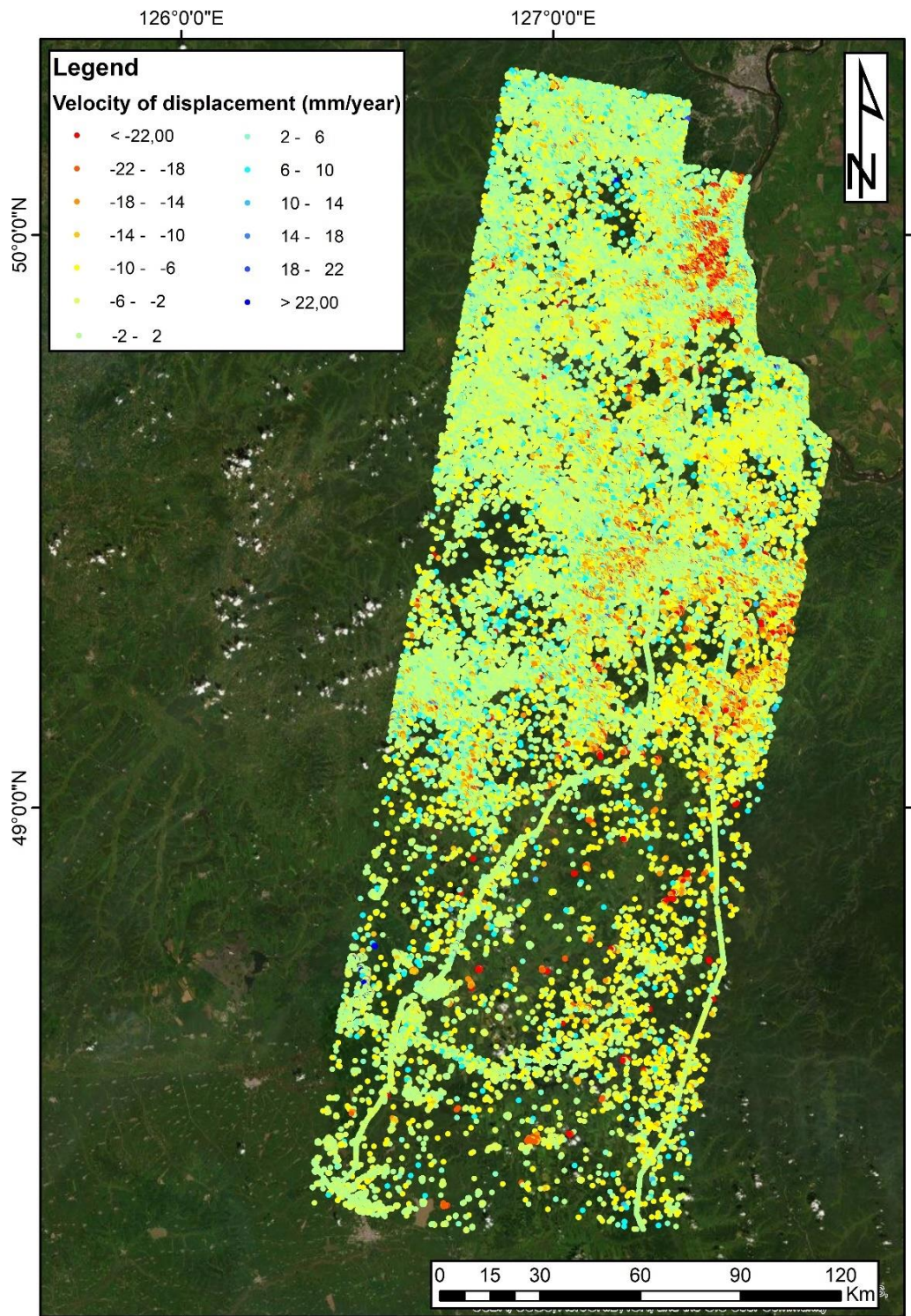


**Figure 3.22** Sentinel-1 SqueeSAR™ Mean Displacement Velocity Results (period: January 2016 to January 2019, 79 Sentinel-1 images used)

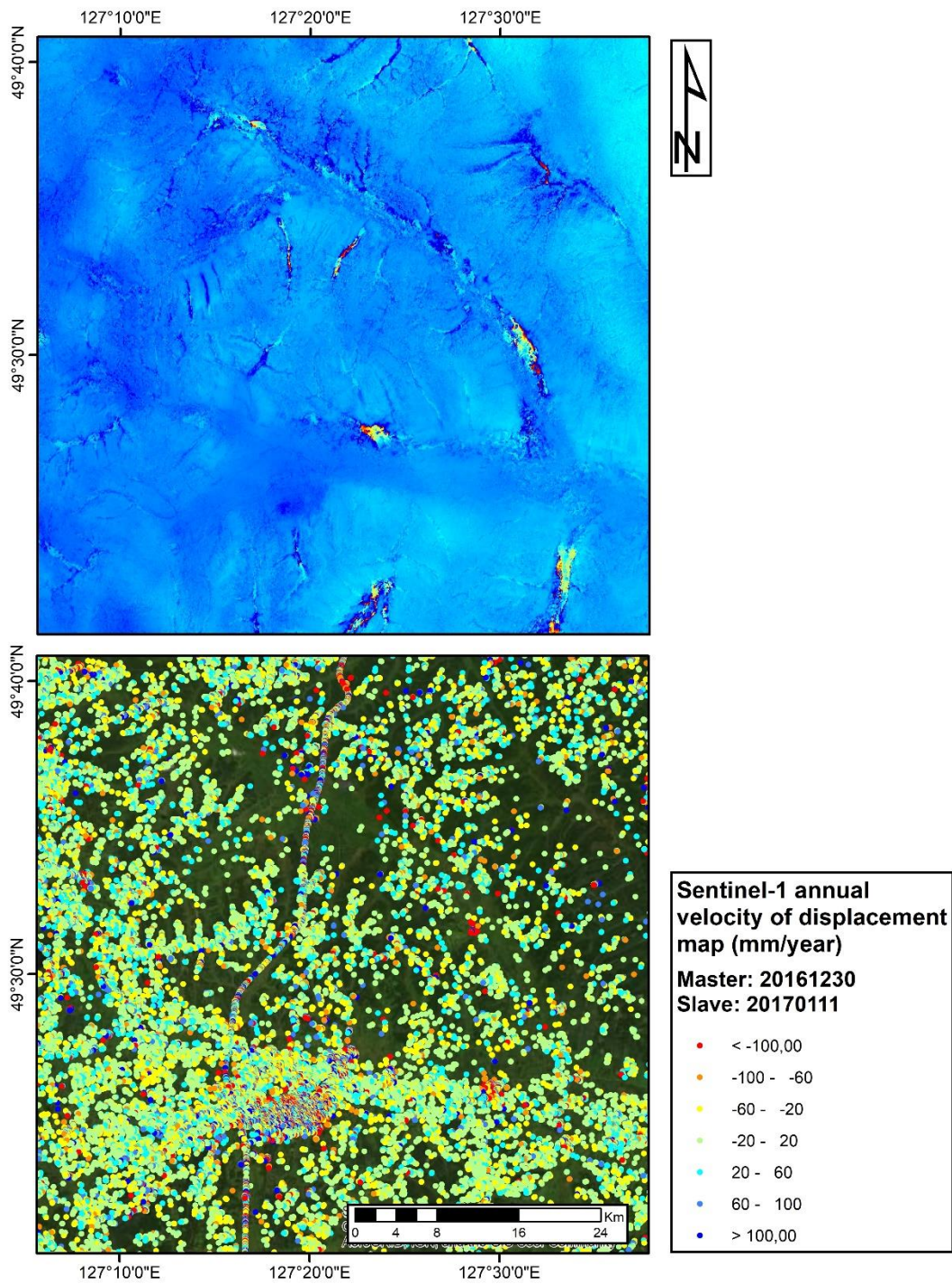


**Figure 3.23** 20161230-20170111 Sentinel-1 differential interferogram and corresponding SqueeSAR™ results



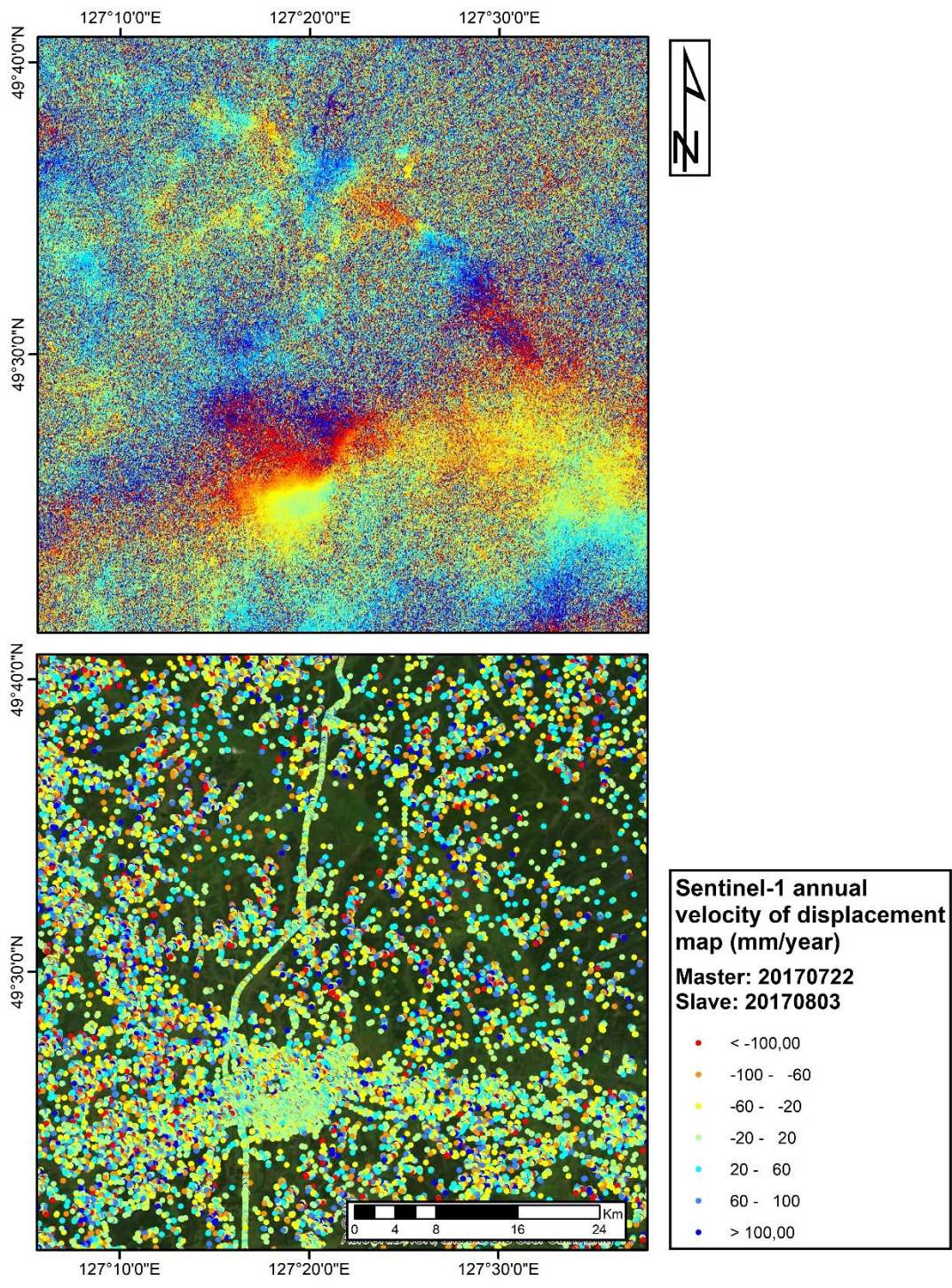


**Figure 3.24** 20170722-20170803 Sentinel-1 differential interferogram and corresponding SqueeSAR™ results

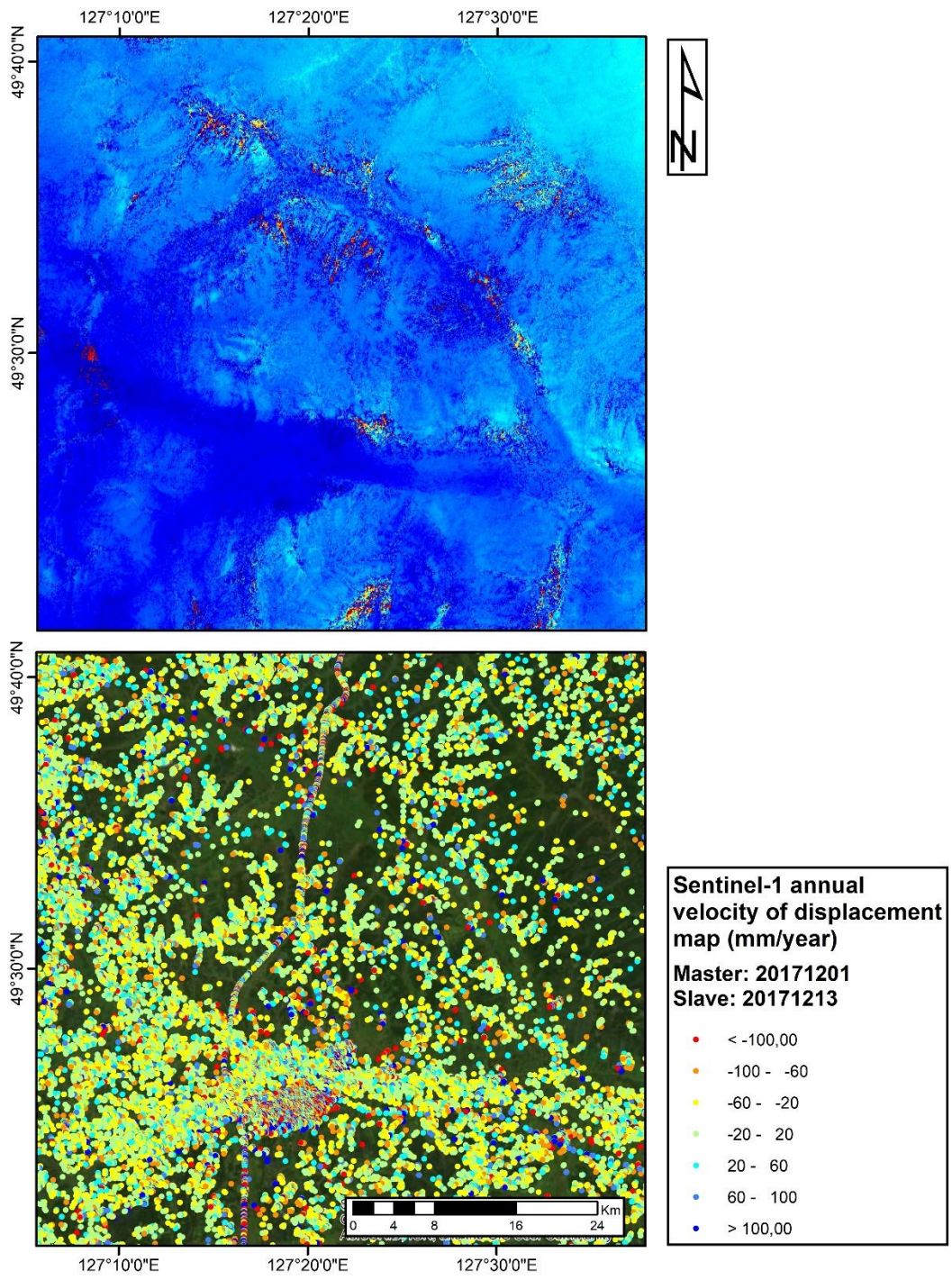


**Figure 3.25** 20171201-20171213 Sentinel-1 differential interferogram and corresponding SqueeSAR™ results

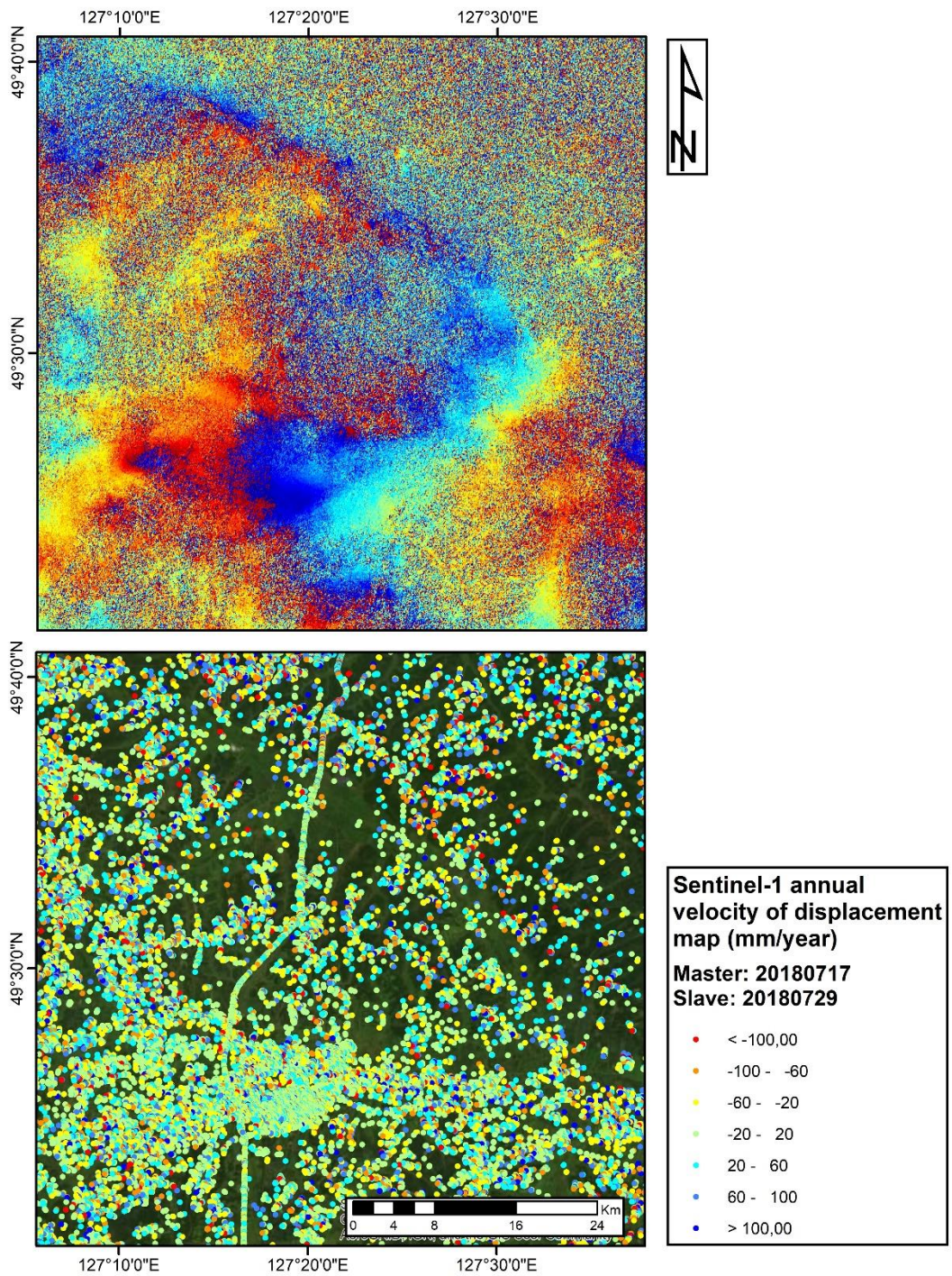


**Figure 3.26** 20180717-20180729 Sentinel-1 differential interferogram and corresponding SqueeSAR™ results

## 3.4. Discussion

### 3.4.1. Sentinel-1

Thanks to its operation strategy, Sentinel-1 provides a huge data stack of 79 images to this research, from a rather short temporal range of 3 years from January 2016 to January 2019. The temporal interval of this dataset is 12 days, which is regular and frequent during the most time of this study, although the temporal interval is not quite equally distributed during the beginning of the image acquisition (from June 2015 to September 2016).

Conventional differential InSAR method was proved to be efficient for the detection of ground motion in the study area. However, restricted by the low coherence of the interferometric pairs during thawing seasons, we here only present one C-band Sentinel-1 differential interferogram of freezing season in the Chapter 3.3 thanks to the GEP cloud processing. Phase unwrapping (especially during the thawing seasons) to the raw interferograms can prone to many errors as the domain land cover in the study area is vegetation (including forests and croplands), and the objective of differential InSAR processing is to visualize the hotspots of the subsidence between two acquisitions that are not easy to be visualized in the SqueeSAR™ processing, but not to measure the intensity of the ground subsidence. Therefore, we did not perform phase unwrapping in the stepwise raw differential interferograms processing.

From the Sentinel-1 SqueeSAR™ results, it is clearly observed that the PS/DS targets are mainly distributed over the urban/man-made infrastructure land cover, including the Beian-Heihe expressway (linear infrastructure, in the middle of the study area), the electricity power facilities (linear infrastructure, on the right of the study area) and the Sunwu town (the biggest settlement of the study area, located in the center of the data frame). The displacements (shown in red-green-blue colors) over this land cover are usually changing gradually, less bumpy compared to the surrounding pixels thanks to its coherent backscattering signal to the Sentinel-1 sensor. Signals that refer to seasonality are barely observed from the time series of displacement. The observed seasonality phenomena are relatively stronger from the ALOS PALSAR SqueeSAR™ result. It could be indicating that initially, the phenomenon of seasonal ground deformation from 2007 to 2010 in the study area was severe, but the deformation intensity had been slowing down as the time went. It is probably because of the isolated permafrost patches in this region has been nearly fully degraded. Considering the density of the extracted PS/DS targets from the Sentinel-1 SqueeSAR™ results, we still do not know if the small patches of permafrost that locate in the places where there is no PS/DS have been fully degraded or not recently.

From the deformation results on the Beian-Heihe expressway, we have observed a subsidence event near the Sunwu town. We later confirmed that those subsidence records are not related to those indicators that would be influencing the accuracy of the analysis including Atmosphere Phase Screen (APS) and topography effect due to its complexity. After comparing to the results provided by the local administration of the expressway, we realized that most of the major subsidence events on the expressway tarmac and the slopes along the expressway happened before the thawing season of 2016, and then, the expressway administration organized multiple maintenance projects of the expressway during July and August 2016. From the displacement records of PS/DS, some bumpy displacement records of time series in the summer of 2016 can be referring to those local repairing projects, but those displacement records of PS/DS targets are different from the local GPS records (confidential data) at the same time. It should be also questioned that considering that during the maintenance projects, the tarmac over the expressway was dug out and repaved. The PS/DS points were still extracted over the maintenance section of the expressway despite the huge differences of the SAR backscattering characteristics between tarmac and gravels in theory.

Some ground subsidence events were verified as being caused by permafrost degradation by a comparison to a research conducted at regional scale using Landsat ETM+ thermal band mapping and thermal transformation equation method to investigate the regional ground thermal status (Wang et al, 2014). Like the conventional Sentinel-1 differential interferogram processing, most of the ground subsidence phenomena were observed near the Holocene deposits nearby the riverbanks, where are favorable for permafrost growth. But theoretically, over the Holocene deposits in the watersheds, the PS/DS points are unlikely to be extracted because the humidity change of the ground coupled with the local hydrology and seasonality had caused extremely low amplitude stabilities during the first PS candidate selection procedure in the SqueeSAR™ processing. It should be questioned that if all, or at which sensitivity the permafrost degradation hotspots nearby the Holocene deposits could be observed through Sentinel-1 SqueeSAR™ processing.

Although the Sentinel-1 SqueeSAR™ has been delivering sufficient PS/DS points on the bare soil, agriculture fields and urban areas, PS/DS points are sparsely extracted in the forests, including deciduous or evergreen, which are the dominant land cover in the study area since the C-band microwave's low capacity in canopy penetration. The deformation signals observed on the agriculture land cover are mixed and very hard to interpret. The reason of the deformation on agriculture land cover could be partially related to a series of agriculture activities including ground water draining, irrigation, plowing, sowing, harvesting or even soil moisture change induced by strong rainfall events. Secondly, the agriculture land cover not only occupies on flat geomorphology but also erosion geomorphology, which has brought more bumpy and controversial displacement results that had obscured the interpretation of the actual ground motion considering the limited spatial resolution of Sentinel-1 sensor.

Many phase jump events during the phase unwrapping procedure are widely observed from both Sentinel-1 differential InSAR and SqueeSAR™ processing results. From the histograms of the time series of displacements obtained by Sentinel-1 SqueeSAR™ processing, the phase jump is shown as a clear gap of 5.6 cm in two neighboring observations where occurred the unwrapping error, as described in the previous context. Most of the unwrapping errors occur during the summer season due to the low coherence that caused "salt-and-pepper" effect in wrapped phase interferograms. Taken the mass and dense vegetation land cover along the relatively thin expressway and the electricity power facilities into consideration, it would be a challenge to maintain the continuous phase unwrapping over those noisy and speckled background backscattering signals. As a contrast, the interferometric coherence is high over the expressway and the electricity facilities that somehow eliminated the phase jump error. But the rather thin and linear feature of the expressway did not contribute much in the unwrapping procedure. The size of smoothing filter is even larger than the width of those expressway and electricity facilities. Therefore, the phase unwrapping procedure is an enormous challenge in the processing of Sentinel-1 summer images.

The velocity of the deformation seems various with the different altitudes of a watershed. On the top of watershed, a slow velocity of displacement around 5 mm/year can be observed in a rather common and general pattern. Meanwhile the velocity at the toe of watersheds, and even in the draining channel nearby have shown a higher velocity more than 30 mm/year. Such phenomena can be observed on the watersheds on the floodplain nearby. The reason of the subsidence over the watershed can be related to the soil compression of the organic soil in that region.

### 3.4.2. ALOS PALSAR

The permafrost deformation hotspot is clearly mapped using ALOS PALSAR SqueeSAR™ results and then further studied using the ALOS PALSAR DInSAR analysis. Like the Sentinel-1 data stack, ALOS PALSAR provides a stack of SAR images with a temporal baseline of three years. But limited by the imaging acquisition mode and low revisit cycle of the ALOS PALSAR sensor, the amount of the images is as few as seventeen. Therefore, from the ALOS PALSAR SqueeSAR™ displacement results, the data records are much less dense compared to the histogram of the Sentinel-1 SqueeSAR™ results. Such limitation of low temporal resolution of less than 5 images per year could bring problems in the understanding of ground motion seasonal dynamics, especially in a cold region like this study area. The lack of the image acquisition during spring and autumn seasons has brought challenges in the identification of the tipping point of the permafrost annual state change. More external expert information is needed to help in the identification of permafrost spatial distribution and understanding in the permafrost dynamic, although we can still estimate the intensity of the ground stability by mapping the total displacement in the three years.

The 8-day MODIS land surface temperature time series didn't show a high correlation with the time series of ground deformation. This result does not show consistency to the air temperature data from 1960 to 2019 of Sunwu National Meteorological Station as stated in Shan et al. (2020) in Chapter 3.1. The reasons could be various. One possible reason could be concluded as the 8-day average temperature time series had eliminated the information including daily maximum and minimum temperature variations. Despite the annual state change of the seasonal frozen soil, the thawing of permafrost would bring the water away and make the ground more arid, which would then cause the increment diurnal change of land surface temperature as the loss of the most effective thermal inertia. Such increasing diurnal change is not possible to be observed in the product of 8-day MODIS land surface temperature time series. In the future studies, the 1-day product with the maximum, minimum and the average land surface temperature will be applied into the correlation study.

Because of the usage of different algorithms while generating the differential interferograms (Sentinel-1: GEP DIAPASON, ALOS PALSAR: ENVI SarScape), the results of differential interferograms of both sensors are not compared and discussed. The SqueeSAR™ results of Sentinel-1 and ALOS PALSAR were then compared, shown in **Figure 3.27** and **Figure 3.28**. Both figures were located at the same position, zoomed at the same scale and applied the same legend. Because the image frame covered area of both results are not identical, we did not compare the overall characters of the PS/DS points in detail. From this comparison, regardless of the limited image quantity in the stack, but thanks to L-band's capacity in vegetation canopy penetration, the ALOS PALSAR SqueeSAR™ analysis extracted far more PS/DS targets in the forests and the draining channels, which are two major land cover types in the clipped study area. The ALOS PALSAR SqueeSAR™ result did not cover some parts of the Beian-Heihe expressway, because a reconstruction and expansion engineering project started from the summer of 2009. Due to the instability of the backscattering amplitude signal over the highway towards the ALOS PALSAR sensor, which makes the SqueeSAR™ processing cannot extract the PS/DS candidate point at those places in the beginning. That is why there is no point extracted along some sections of the Beian-Heihe expressway in ALOS PALSAR SqueeSAR™ processing.

How winter snowpack will influence the interferometric results is not discussed because according to the high coherence during winter seasons in both ALOS PALSAR and Sentinel-1 interferometric processing, there is limited proofs indicating that the quality of displacement results in freezing seasons are worse than the results in thawing seasons.

### 3.4.3. Other possible sensors

Besides the C-band Sentinel-1 and L-band ALOS PALSAR data, we also tested the feasibility of using X-band TerraSAR-X data to reveal the ground deformation in our study area. To accomplish this research objective, we checked the TerraSAR-X SAR data stack first but found out that the temporal acquisition of the data only covers from April 2012 to November 2012, and the total amount of the available images was only 15, with an average temporal interval of 11 days. The low quantity of the TerraSAR-X images cannot meet the minimum demand of SqueeSAR™ algorithm. After generating some raw, wrapped differential interferograms using SNAP software and SAR image acquisitions during the thawing and wetter seasons of spring and summer in a year, the extreme low coherence, and noises in wrapped interferograms would be severe problems for PS/DS target extraction even if there was enough data acquisition. In the interferograms of autumn season, the fringes near man-made infrastructures are slightly clearer than the interferograms of spring and summer and the coherence value is higher. The Beian-Heihe expressway can be clearly identified from the coherence map but cannot be identified from the wide-spread noises of the interferograms. Although different sizes of Goldstein filters, low-pass multi-looking filters and de-speckle filters were applied, there is still no clear phase signal observed from the wrapped and unwrapped interferograms. Therefore, we did not introduce the X-band TerraSAR-X data into this research although it has higher spatial resolution and a frequent revisiting cycle.

Additionally, due to a lack of SAR observation, the estimation and analysis of ground deformation from 2010 to 2015 is not available after checking COSMO-SkyMed, RADARSAT-1/2 and ENVISAT data storage.

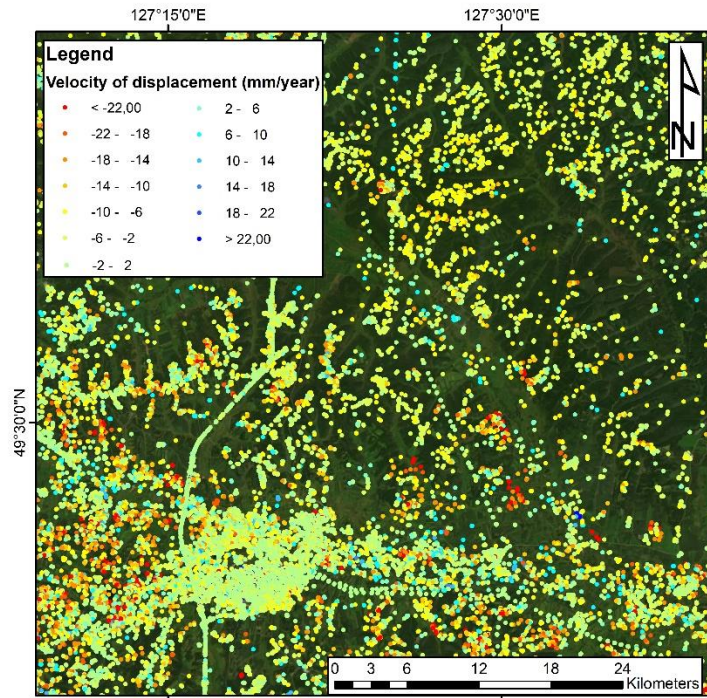


**Figure 3.13** Cropped Sentinel-1 SqueeSAR™ mean displacement velocity result

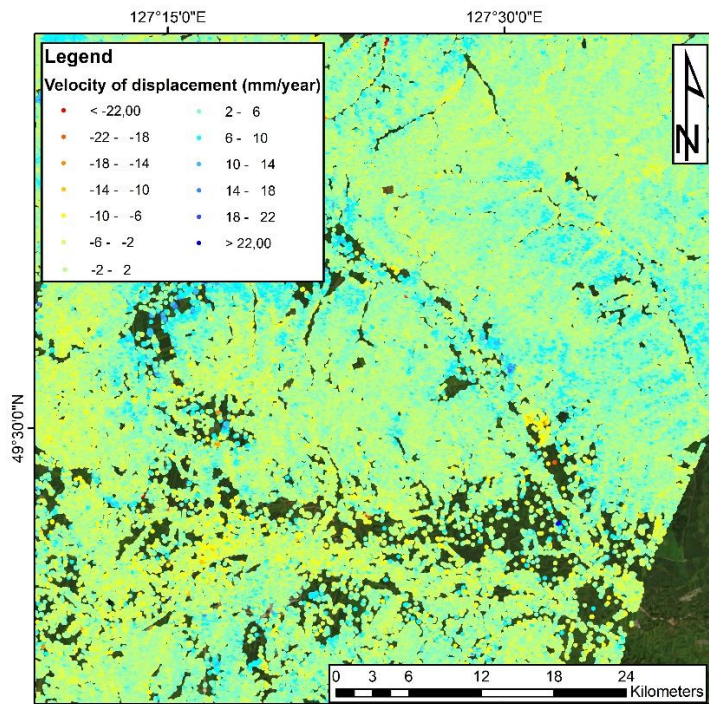


**Figure 3.28** Cropped ALOS PALSAR SqueeSAR™ mean displacement velocity result



## Chapter 4. Case Study 2: Aosta Valley Region, Northwestern Italy

### 4.1. Introduction

Periglacial processes in mountainous regions are prone to catastrophic mass wasting processes, such as rockfalls, glacial floods, landslides, permafrost degradation, or debris flows (Kääb et al., 1997; Kääb & Kneisel, 2006), and have been playing a key role in alpine landscapes evaluation due to their sensitivity to thermal changes, as well as human activities (Haeberli et al., 2017; Solari et al., 2019; Imaizumi et al., 2018; Roer et al., 2014; Cignetti et al., 2016; Haeberli et al., 2006; Korup et al., 2010a; Korup et al., 2010b; Lugon & Stoffel, 2010; Schneuwly-Bollschweiler & Stoffel, 2012; Barboux et al., 2014). Rock glacier is a typical kind of complex periglacial landform existing in alpine landscapes of permafrost regions (Haeberli et al., 2006, Solari et al., 2019). It is a tongue- or lobate-shaped morphology, containing ice-rich or frozen debris and steadily creeping perennially along non-glacierized slopes (Liu et al., 2013; Haeberli et al., 2006). Rock glaciers usually are characterized into inactive, active, or relict, depending on their recorded kinematic and their ice content (Haeberli et al., 2006). Active rock glaciers creep downslope cohesively because of its internal ice at various deformation rates from mm/year to m/year levels, whereas inactive and relict rock glaciers, due to the low or null ice content, nearly remain static (Strozzi et al., 2020; Liu et al., 2013; Barsch, 1996).

Surface kinematics is a fundamental characteristic of rock glaciers (Haeberli et al., 2006; Liu et al., 2013). Rock glaciers are visible indicators of permafrost thermal status. Changes in climatic conditions and human activities have a severe impact on rock glacier dynamics, and it will increase the frequency and intensity of mass wasting events including debris flow and landslides (Crozier & Glade, 2005; Crozier et al., 2010; Huggel et al., 2012). The dynamics of rock glacier flow provide an easier way to locate and indicate short- to medium-term response to environmental changes and the ongoing degradation of sporadic permafrost (Strozzi et al., 2020).

Monitoring the surface kinematics of rock glaciers in Alpine landscape is of vital importance to increase our capability to assess geological hazards and the permafrost thermal status. There has been a huge increasing of research on the monitoring of rock glaciers in European Alps using both conventional in-situ observations and remote sensing in the past decades (Kääb et al., 1997; Krainer & Mostler, 2000; Delaloye et al., 2008; Noetzi & Muehll, 2010; Ikeda & Matsuoka, 2002; Lugon et al., 2004; Otto et al., 2009). In-situ instruments are installed at close distances to the rock glaciers to acquire high resolution full displacement time series of each rock glacier over a specific time. However, the regional scale dynamic of rock glaciers cannot be determined solely relying on the field observations that consumes huge amount of substantial labor, time, and financial budgets. Remote sensing is the major technique to better understand the rock glacier dynamics and thus, the situation of permafrost (Strozzi et al., 2020). Among remote sensing methods, spaceborne DInSAR has developed fast and were extensively applied in the recent years into the measurement of rock glacier dynamics (Rignot et al., 2002; Kenyi et al., 2003; Strozzi et al., 2004; Liu et al., 2013; Lilleøren et al., 2013; Barboux et al., 2014; Rick et al., 2015; Necsoiu et al., 2016; Wang et al., 2017; Villarroel et al., 2018; Brencher et al., 2020). MTInSAR can provide the long displacement time series data with extensive spatial coverage without sacrificing the accuracy compared to field investigations.

Some researchers have applied DInSAR method in rock glacier inventories. A study in Sierra Nevada, California, USA (Liu et al., 2013) has shown the potential of L-band ALOS PALSAR in rock glacier inventory. Clear fringes from the interferogram represent the displacement of approximately 5 cm over the detected active rock glaciers during the two imagery acquisition dates of 46 days. Imaizumi et al. (2018) applied L-

band ALOS PALSAR DInSAR analysis in Zermatt Valley, Switzerland and found out that the rock glaciers are likely to be distributed on north-facing slopes.

Previously in this research a series of pioneer research using free-of-charge C-band Sentinel-1 DInSAR analysis of Aosta Valley Region had been performed. But restricted to the low spatial resolution and poor penetration capacity of C-band Sentinel-1 sensor, the backscatter signal over some vegetation-covered areas and snow-covered areas during winter seasons are noisy and blurred, meanwhile the coherence is rather low. From the experiences of the low-land permafrost detection research in northeastern China (Chapter 4), L-band ALOS PALSAR InSAR analysis will show clearer fringes and higher coherence to help in the locating of active rock glaciers thanks to its stronger capacity of canopy and snow cover penetration compared to C-band Sentinel-1.

As the development of the conventional DInSAR method, advanced DInSAR methods have been developed and widely applied into the research of rock glacier kinematics. In the past, the irregular acquisitions of the past SAR missions limited a long-term monitoring of rock glacier kinematics. Thanks to the launch of the Sentinel-1A/B constellation, the regular imaging (every 6 days in Europe, every 12 days over other areas worldwide) and the free and open data policy have made the long-term monitoring possible. Strozzi et al. (2020) used Sentinel-1 MTInSAR method to complete in situ measurements of active rock glacier kinematics worldwide. Reinosch et al. (2020) used Sentinel-1 MTInSAR method and revealed that the displacement of the rock glaciers on the Nyingqêntanglha range on the Qinghai Tibetan Plateau does not show seasonal pattern, but a linear pattern instead. Brencher et al. (2020) employed Sentinel-1 MTInSAR to identify and monitored nearly 255 active rock glaciers in an area of 27.6 km<sup>2</sup> at an average elevation of 3290 m in the Uinta Mountains, Utah, USA then analyzed the trend of degradation with the climatic factors of daily temperature, soil moisture, snow-water equivalent, and precipitation.

Therefore, in this study, our first objective is to exploit the deformation characteristics of active rock glaciers in Aosta Valley Region, northwestern Italy using C-band Sentinel-1 SqueeSAR<sup>TM</sup> processing results and to produce a rock glacier activeness map using L-band ALOS PALSAR DInSAR analysis. This work is organized as follows. We first introduce the study area of Aosta Valley Region by geomorphological, environmental, and meteorological characteristics. Then we introduce the data and the proposed research methodologies, including interpretation of Sentinel-1 SqueeSAR<sup>TM</sup> results acquired from 2015 to 2020 in both ascending and descending orbits in the case of rock glacier monitoring, and the processing and the interpretation of DInSAR analysis of ALOS PALSAR data in descending orbit in the exploitation of rock glacier mapping. We then present some examples that indicate the displacement of the rock glaciers in the study area using Sentinel-1 SqueeSAR<sup>TM</sup> and ALOS PALSAR DInSAR results. Finally, we make a discussion on the evaluation of the methodologies we applied in this research and the feasibility of the InSAR analysis in the research of rock glaciers.

## 4.2. Study area, data, and methods

### 4.2.1. Aosta Valley Region

Aosta Valley (Valle d'Aosta in Italian language, VdA in abbreviation) Region locates in the northwestern Italy. Geologically, it is a part of the Western Alps. It is the smallest region of Italy, covering an area of 3262 km<sup>2</sup>. It is considered as a mountainous region because almost 50% of the region's territory has an elevation higher than 2000 m a.s.l. and the highly variable topography ranging from 300 m a.s.l. to the mountain peaks higher than 4000 m a.s.l. (Cignetti et al, 2016). The geomorphology and the Digital Surface Model are shown in **Figure 4.1** and **Figure 4.2**, respectively.

In VdA Region, the densely populated areas and other man-made infrastructures are mainly distributed in the main valleys around 500 to 1500 m a.s.l. The deciduous and evergreen forests and grasslands, which are gradually replaced by bare rocks, debris, or glaciers, at an elevation higher than the tree line of around 2000 m a.s.l. The mountainous morphology brings a variety of small and local climates that influences the landscapes, as the high peaks that act as morphological "barriers" against the passing through of humidity component in the air masses (Ratto et al., 2003). The total precipitation in both snow and rain regimes in the VdA Region is around 1000 - 1100 mm/year, as along the valle where located the human settlements, the climate is temperate, with an around 600 mm/year precipitation (Ratto et al., 2003; Solari et al, 2019). During winters, snowfalls are frequent, and the snow cover usually lasts from late October to early April of the next year, and the extreme rainfalls usually occur between late spring (late April to May) and early autumn (September to early October), registering cumulated rainfalls over 250 mm in few days (Salvatici et al, 2018).

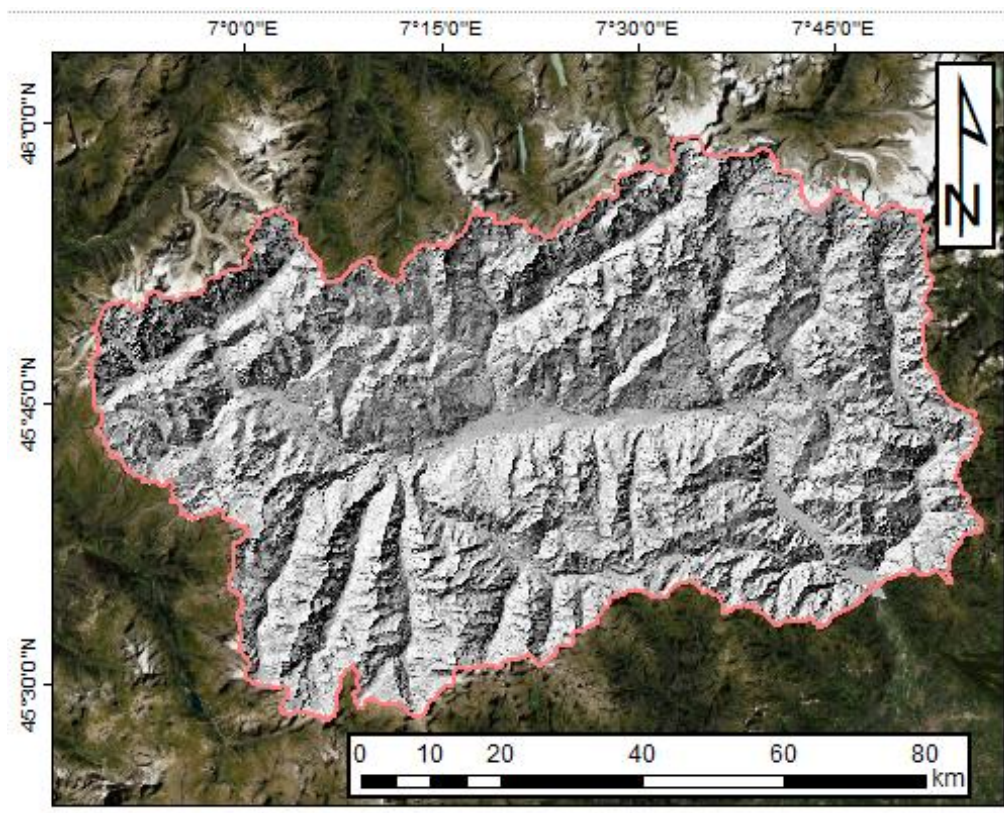


**Figure 4.1** Hill shade map that represents the mountainous geomorphology of the VdA Region.

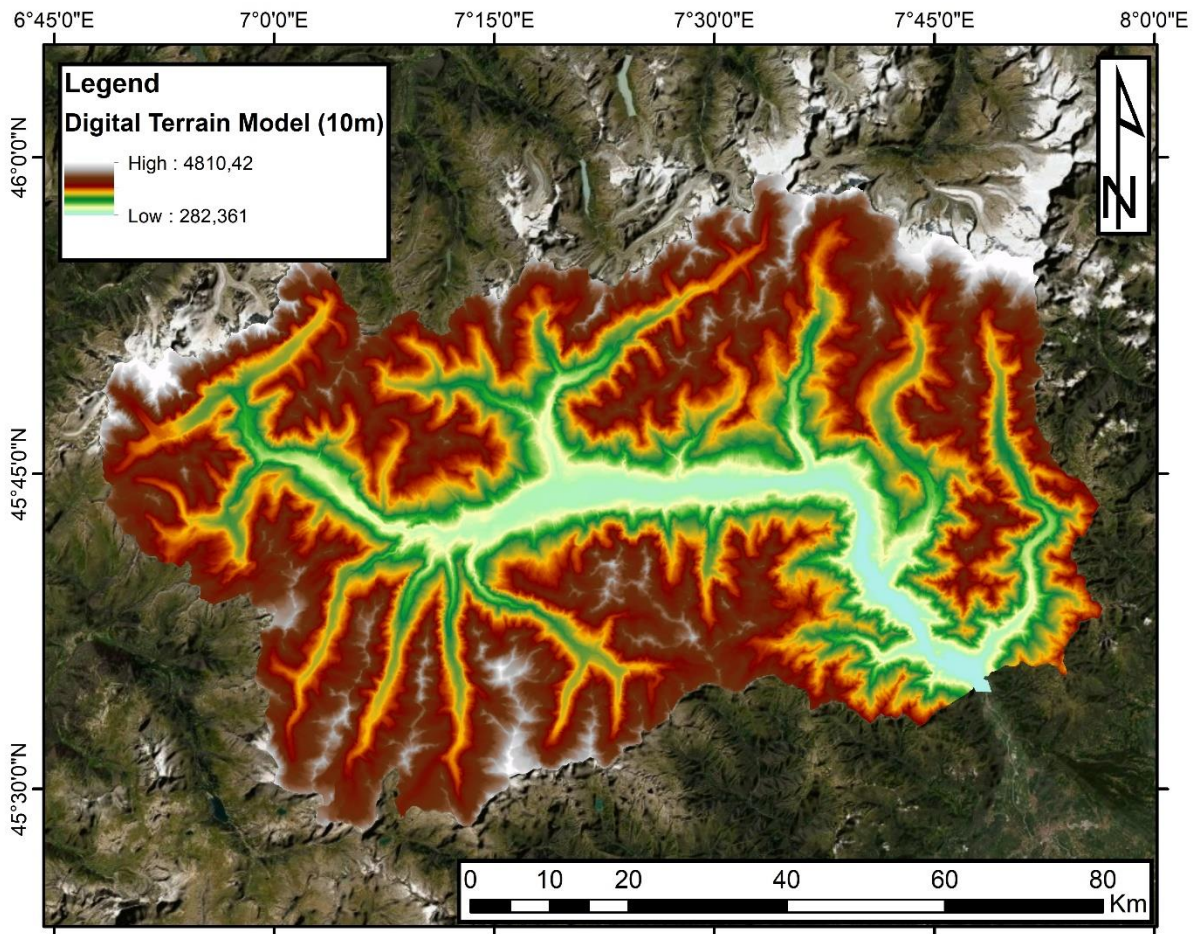


**Figure 4.2** 10-meter resolution Digital Terrain Model (DTM, 10-meter resolution) of VdA Region

#### 4.2.2. Rock glacier inventory data of Aosta Valley Region

VdA is characterized by mass movements related to periglacial landforms, such as rock glaciers, which commonly exist in alpine landscapes. The rock glacier inventory of VdA Region is published on an online GIS platform operated by the regional authorities but has not provided public download function. Therefore, the author remapped the online data by geo-referencing into ArcGIS software with the help of the in-built Microsoft Bing high-resolution optical images, as shown in **Figure 4.3**.

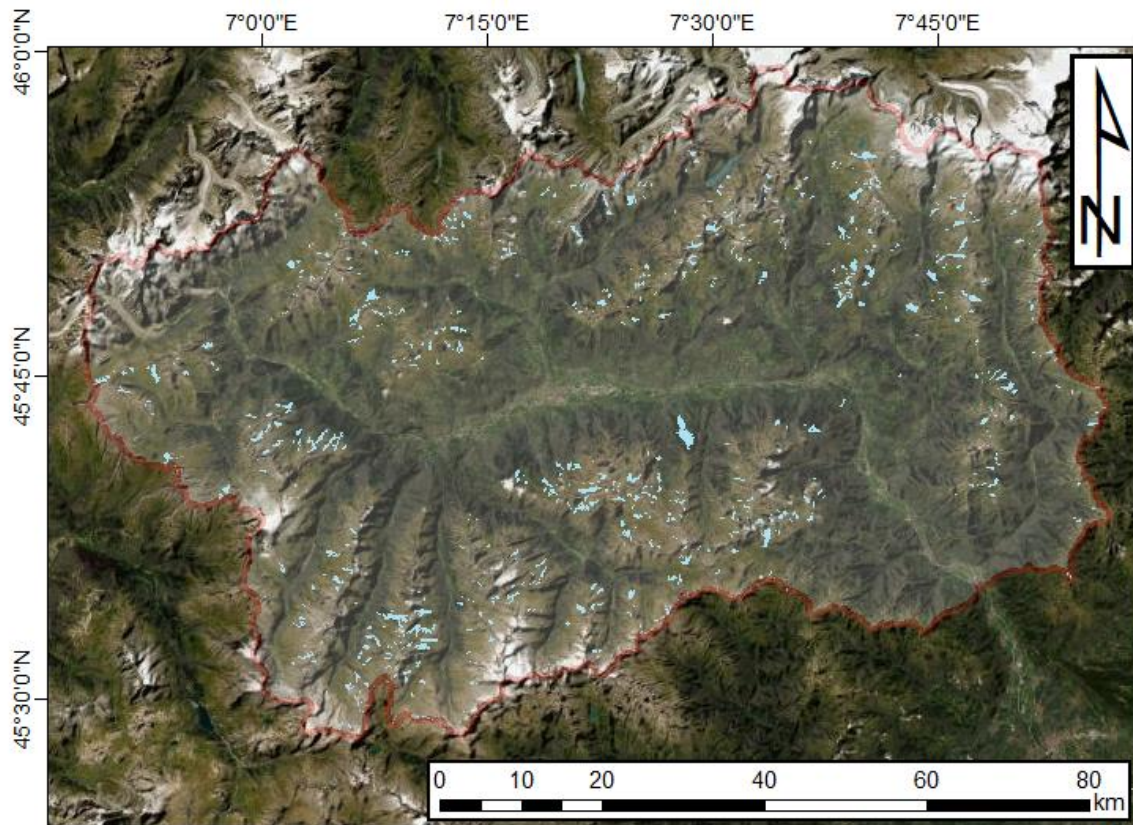


**Figure 4.3** Rock glacier inventory dataset in VdA Region (source: <http://catastoghiacciai.partout.it/GeoGhiacciai> )

### 4.2.3. Sentinel-1 SqueeSAR™ processing results

This methodology initial with the delivery of deformation maps of the entire VdA Region. Those maps are derived by analyzing two large stacks of C-band Sentinel-1 data using SqueeSAR™ algorithm (Ferretti et al., 2011). This method has been introduced in detail in Chapter 2. Sentinel-1 and ALOS PALSAR dataset has been introduced in Chapter 3. Ferretti et al. (2011), Bellotti et al. (2014), Solari et al. (2019) and Carlà et al. (2019) have proved the accuracy and versatility of this dataset.

The following **Figure 4.4** and **Figure 4.5** show the C-band Sentinel-1 SqueeSAR™ processing result from July 2015 to June 2020 in ascending and descending geometries of VdA Region. Considering the period was approximately 5 years, the LOS velocity error brought by the seasonal displacement of permafrost deformation can be neglected. The following tables shown the satellite and acquisition information of ascending and descending geometries.

Satellite	Wavelength	Geometry	Sensor mode	Track	Number of Scenes
Sentinel-1	5.55 cm	Ascending	IW	88	262
		Descending		66	269

**Table 4.1** Satellite information of Sentinel-1 SqueeSAR™ processing

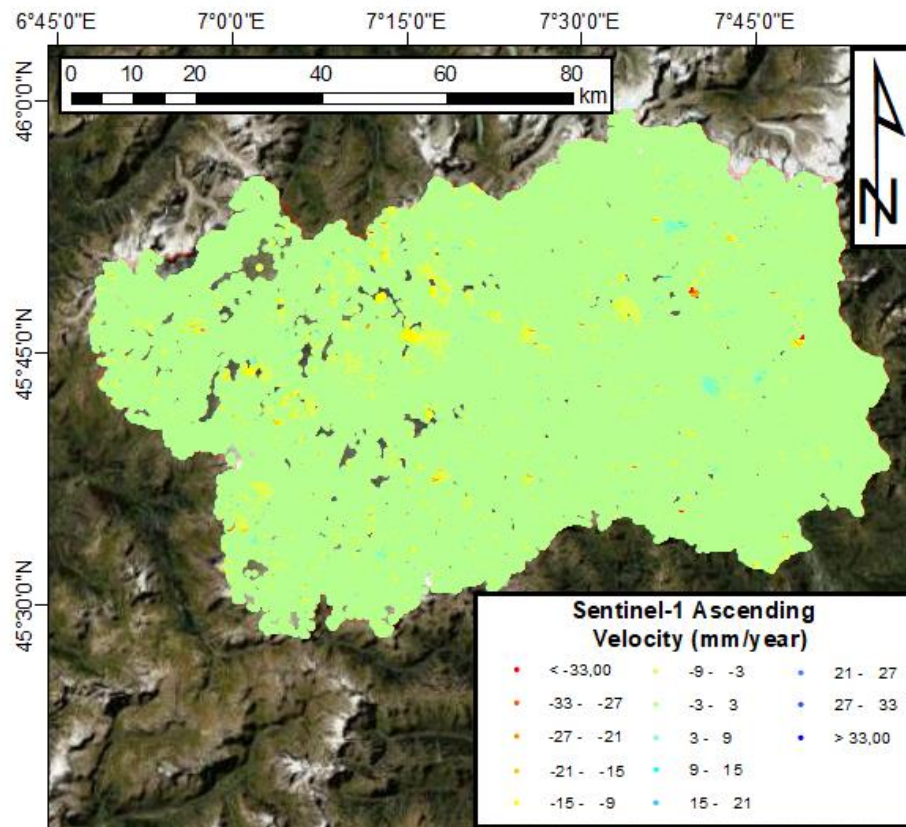


**Figure 4.4** The results of Sentinel-1 SqueeSAR™ analysis in VdA Region, ascending geometry, July 2015 to June 2020

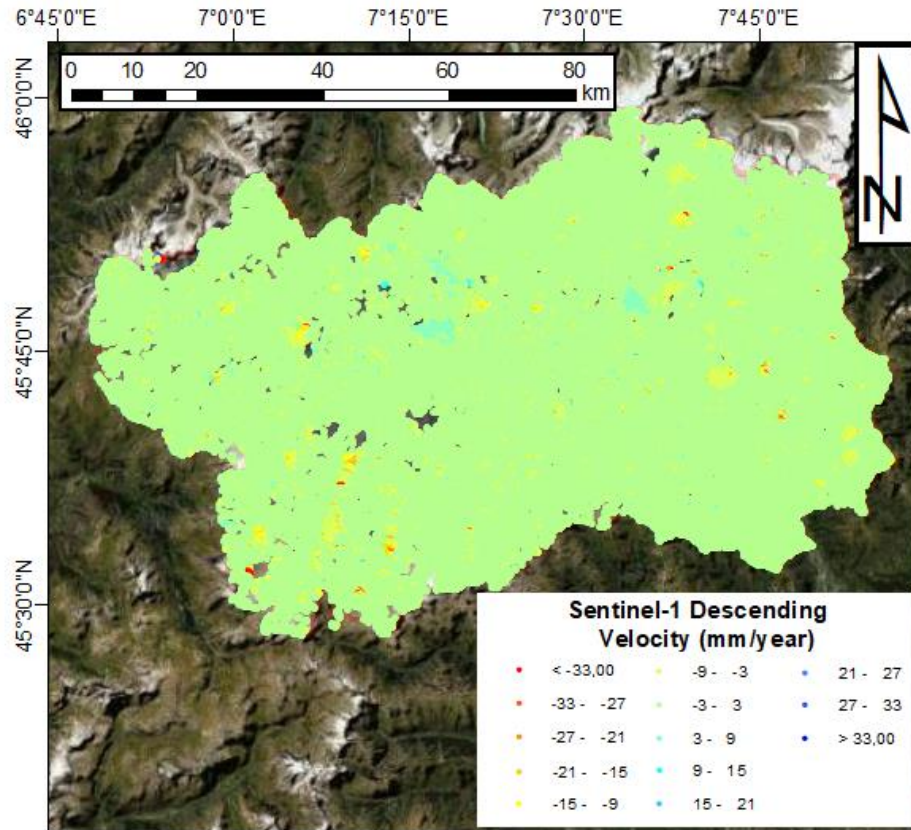


**Figure 4.5** The results of Sentinel-1 SqueeSAR™ analysis in VdA Region, descending geometry, July 2015 to June 2020

#### 4.2.4. ALOS PALSAR data and DInSAR processing

Different from the last research of low-land permafrost in northeastern China, the ALOS PALSAR data used in this research is provided by European Space Agency (ESA)'s Third Party Mission (TPM) on-the-fly processing and dissemination service. The service is free of charge. Users should submit a brief proposal and the information of the required data as a Fast Registration to the service supplier, then the data will be available online to download upon the approval of the Fast Registration submission within 2 days.

Currently, the availability of the ALOS PALSAR data (including PLR, FBS and FBD mode, PLR means Polarimetry, FBS means "Fine Beam Single" meanwhile FBD means "Fine Beam Dual") provided by this service covers Europe, Africa, and Middle East zone, with some worldwide products in addition.

**Table 4.2** listed the imaging dates of the data acquired from the ESA TPM on-the-fly service. According to the available images in the archive, the FBD mode images are mainly collected in the warmer seasons from May to September, meanwhile the FBS mode images are all collected in the colder seasons from December to March of the next year. Considering the seasonality effect in the studies of ground motion in cold regions, two individual series of InSAR analysis of warmer and colder seasons respectively, would be ideal for the identification of the dynamics of rock glacier in different thermal conditions. The interferometric pairs are listed in **Table 4.3**.

FBS mode (HH)	FBD mode (HH+HV)
2008.2.2	2007.8.2
2008.3.19	2007.9.17
2009.2.4	2008.5.4
2009.12.23	2008.6.19
2010.3.25	2009.6.22
	2009.8.7
	2009.9.22
	2010.5.10
	2010.6.25

**Table 4.2** The imaging dates of the acquired available ALOS PALSAR data within the study area provided by ESA TPM on-the-fly service.



<b>FBS mode</b>	2008.2.2 – 2008.3.19
	2009.12.23 – 2010.3.25
<b>FBD mode</b>	2007.8.2 – 2007.9.17
	2008.5.4 – 2008.6.19
	2009.6.22 – 2009.8.7
	2009.8.7 – 2009.9.22
	2009.6.22 – 2009.9.22
	2010.5.10 – 2010.6.25

**Table 4.3** Planned interferometric pairs.

The selection of interferometric pairs follows the criteria as described below:

- (a) The ALOS PALSAR images in the same interferometric stack should maintain the same imaging mode.
- (b) To minimize the ground deformation caused by seasonality effects, the maximum temporal baseline of the ALOS PALSAR images in the same interferometric stack should be smaller than 100.

Therefore, theoretically, 8 differential interferograms should be formulated in this processing. From the processing and interpretation of the delivered L-band ALOS PALSAR interferograms, we aim to delineate the active rock glaciers using supervised classification. The selected active rock glacier should meet the following conditions:

- (a) There should be clear fringes (color difference) covering the moving area on the interferometric phase maps.
- (b) The shape of the moving materials should be tongue- or lobate-shaped on the high-resolution optical image, as described in the Chapter 4.1.
- (c) The interferometric coherence over the moving area should be lower than surrounding pixels, to eliminate the fringes due to the DEM error.
- (d) The target fringes should be much smaller than the size of the located valleys, to eliminate the fringes due to the Atmosphere Phase Screen (APS) error.

### 4.3. Results

#### 4.3.1. Permanent scatters and distributed scatters (PS/DS) detected in the Rock Glaciers by Sentinel-1 SqueeSAR™ analysis

##### 4.3.1.1. General result

We extracted the PS/DS points that locate in the boundary of rock glaciers by regional rock glacier investigation dataset. To eliminate the false labeling of the point velocity due to the strong seasonality in the periglacial landforms, we clipped the 5 annual cycles from July 2015 to June 2020 from the original regional processing of November 2014 to June 2020. They are shown by different orbits in **Figure 4.6** and **Figure 4.7**, respectively. **Table 4.4** lists the basic statistics of the detected active rock glaciers using Sentinel-1 SqueeSAR™ processing.

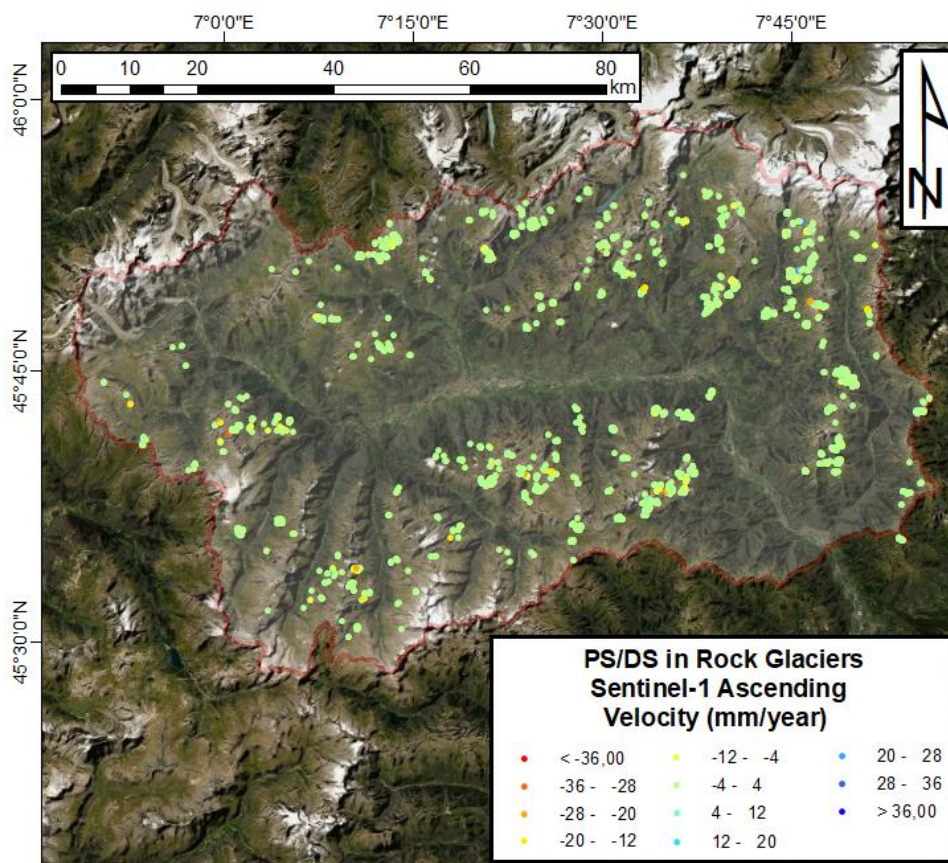


**Figure 4.6** Mean displacement rate map of the rock glaciers in VdA Region, Sentinel-1 ascending orbit, SqueeSAR™ method, from July 2015 to June 2020

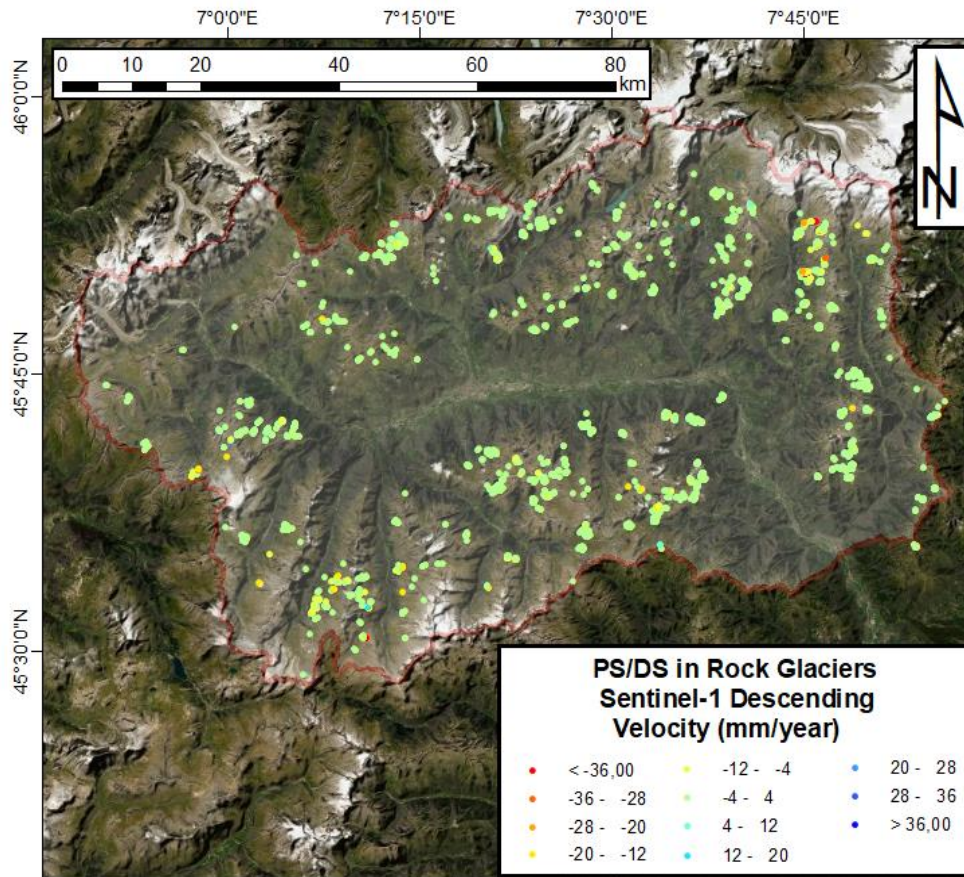


**Figure 4.7** Mean displacement rate map of the rock glaciers in VdA Region, Sentinel-1 descending orbit, SqueeSAR™ method, from July 2015 to June 2020

From the statistics in **Table 4.4**, only few rock glaciers contain enough PS/DS targets to be interpreted. In Chapter 4.3.1.2 and 4.3.1.3 two examples rock glaciers with enough PS/DS inside will be presented.

	Quantity of rock glaciers from the regional authorities' dataset	Total surface of rock glaciers	Detected PS/DS targets over rock glaciers	Rock glacier covered by PS/DS targets	Average PS/DS Targets within a rock glacier	PS/DS Target Density
Sentinel-1 Ascending	941	136 km <sup>2</sup>	2887	386	7	21.2 per km <sup>2</sup>
Sentinel-1 Descending			3146	419	8	23.1 per km <sup>2</sup>

**Table 4.4** Statistics of the displacement time series of the detected active rock glaciers using Sentinel-1 SqueeSAR™ analysis

#### 4.3.1.2. Example 1: La Clapey Gerbioz rock glacier

Here presents a typical active rock glacier detected located at the east of VdA Region, near the main central valley (**Figure 4.8**). The velocity of the movement of the detected PS/DS points is shown in the legend. Then **Table 4.5** listed the characteristic information of this rock glacier. This rock glacier is moving towards northeast direction and consisted with two lobes (shown in yellow contour lines of **Figure 4.8**) located at different altitudes according to the high-resolution optical image and the Sentinel-1 SqueeSAR™ result, thanks to the high PS/DS density. The studied points locate at the front edge of the two lobes, and named as point 1 and 2, shown in the figure as well. **Table 4.6** indicates the interferometric parameters during the SqueeSAR™ processing of the two points.

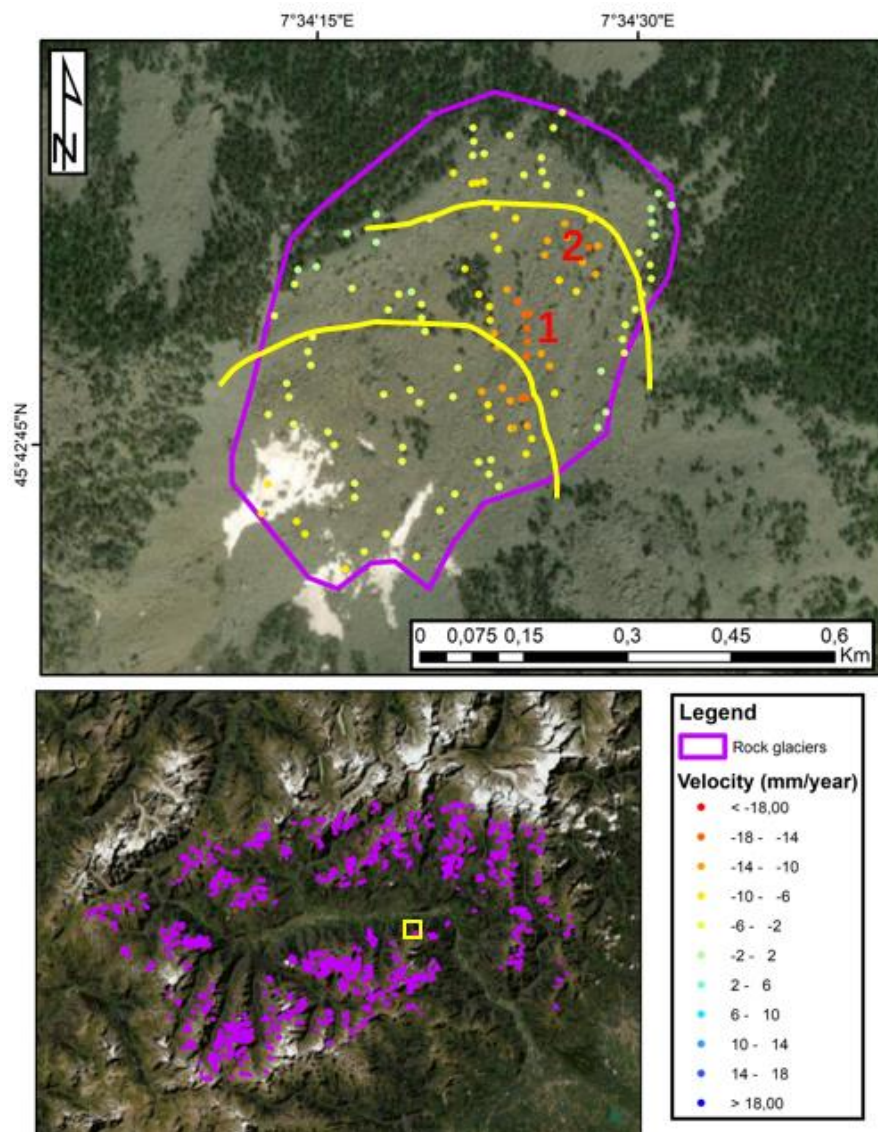


**Figure 4.8** Detected La Clapey Gerbioz rock glacier. The Sentinel-1 SqueeSAR™ result is on ascending geometry.

<b>Maximum length (km)</b>	0.8
<b>Maximum width (km)</b>	0.56
<b>Area (km<sup>2</sup>)</b>	0.31
<b>Number of PS/DS</b>	122
<b>PS/DS density</b>	394/km <sup>2</sup>

**Table 4.5** The characteristic information of this rock glacier

<b>Point ID</b>	1	2
<b>Longitude</b>	7.573546	7.574348
<b>Latitude</b>	45.713560	45.714294
<b>Point type</b>	PS	PS
<b>Altitude (meter a.s.l.)</b>	1967.7	1948.8
<b>Deformation velocity along line-of-sight direction (mm/year)</b>	-15.2	-14.5
<b>Coherence</b>	0.94	0.92

**Table 4.6** The interferometric parameters of the studied points

The type of both two selected points are PS, and their coherence values are higher than 0.90, which refers to their high reflectivity and stability of the backscattering signals. Both points represent the maximum deformation velocity along line-of-sight direction of the two lobes of the entire rock glacier is around 15 mm/year, and the velocity of deformation is not significantly different among each year during July 2015 to June 2020. The seasonal effect can be clearly noticed from both displacement time series (**Figure 4.9**). The displacement is severe during the freezing seasons, from September to the March of the following year, but remains relatively stable during the thawing seasons, from March to September. The displacement records of the two studied points have shown a strong seasonality as described. The land surface temperature from November 2014 to July 2020 are also plotted in the figure.

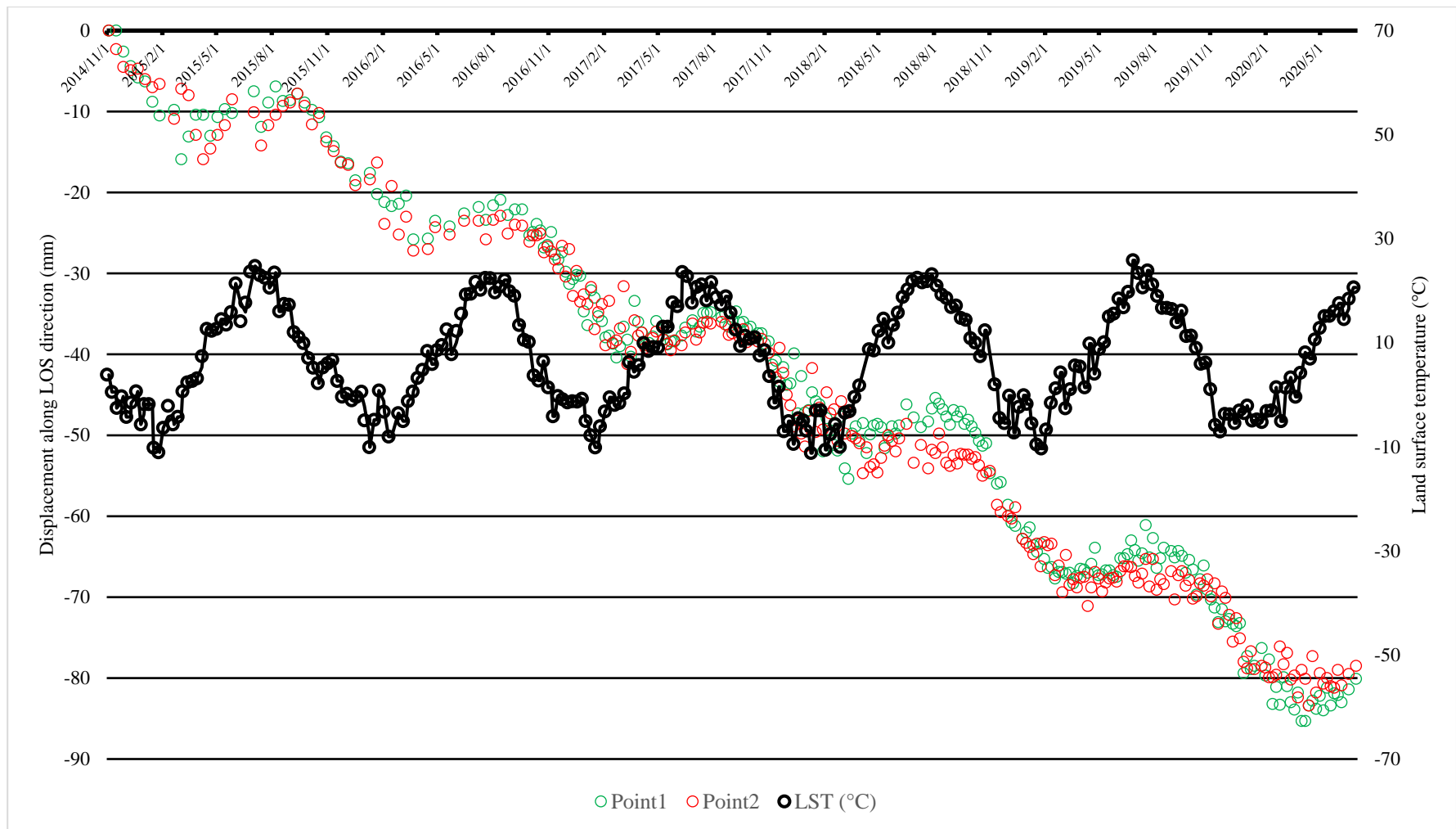


**Figure 4.9** The displacement time series of the studied points in La Clapey Gerbioz rock glacier and the MODIS 8-day land surface temperature from November 2014 to July 2020

### 4.3.1.3. Example 2

Here presents the second example of active rock glaciers locate at the northeast of VdA Region (**Figure 4.10**). The rock glacier located at top-left (RG1) of the figure and the rock glacier in the center (RG2) are moving towards northwest direction and the rock glacier located at bottom-right (RG3) is moving towards southeast direction. The central rock glacier is consisted with multiple lobes according to the high-resolution optical image but cannot be determined from the SqueeSAR™ result due to the low PS/DS density. The velocity of the movement of the detected PS/DS points is shown in the legend. Four PS/DS points are studied in this example, shown in the figure, and named numerically. Then **Table 4.7** listed the characteristic information of this rock glaciers. **Table 4.8** record the interferometric parameters during the SqueeSAR™ processing of the four points, respectively.

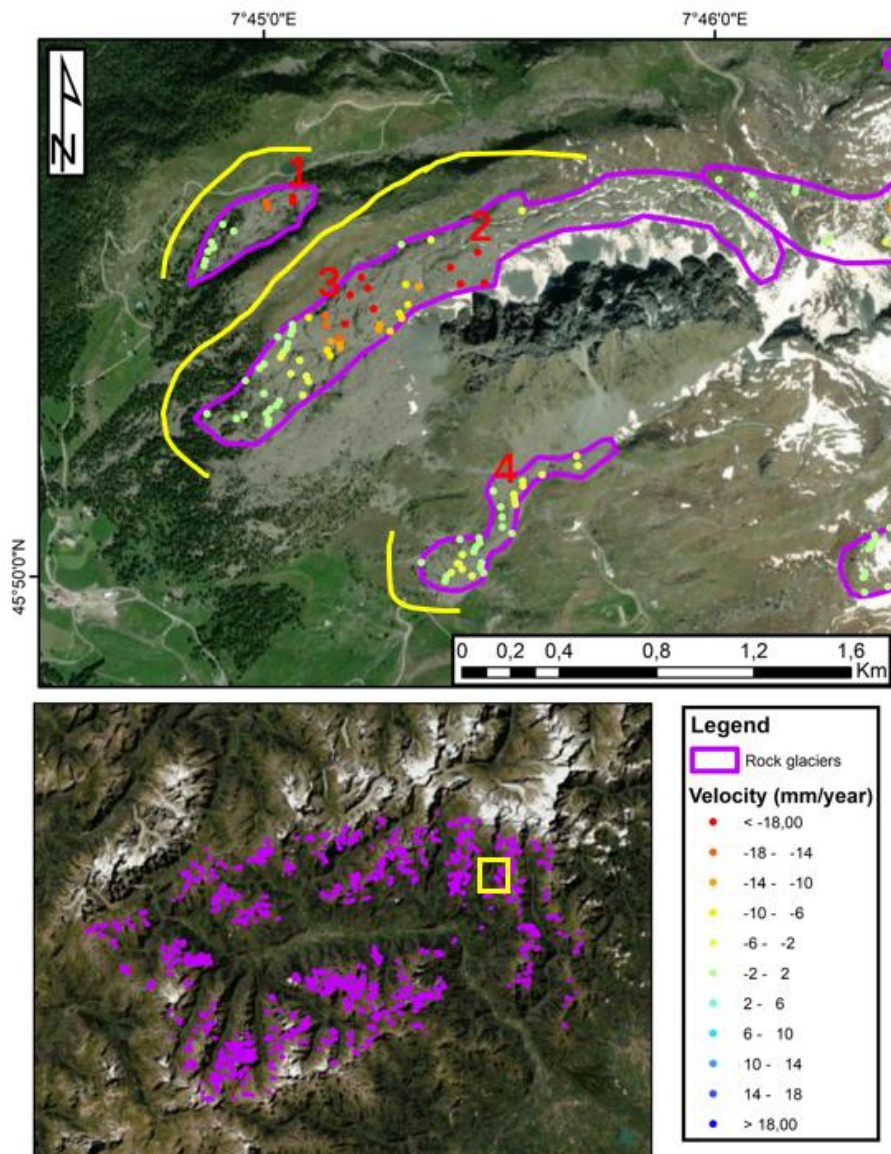


**Figure 4.10** Detected rock glaciers Example No.2. The Sentinel-1 SqueeSAR™ result is on descending geometry.



<b>Rock glacier name</b>	RG1	RG2	RG3
<b>Maximum length (km)</b>	0.65	2.79	0.96
<b>Maximum width (km)</b>	0.2	0.27	0.21
<b>Area (km<sup>2</sup>)</b>	0.09	0.6	0.12
<b>Number of PS/DS</b>	11	56	30
<b>PS/DS density</b>	122/km <sup>2</sup>	93/km <sup>2</sup>	250/km <sup>2</sup>

**Table 4.7** The characteristic information of the studied rock glaciers

<b>Point ID</b>	1	2	3	4
<b>Longitude</b>	7.751024	7.757852	7.753214	7.759578
<b>Latitude</b>	45.843114	45.841696	45.840565	45.835629
<b>Point type</b>	PS	PS	PS	PS
<b>Altitude (meter a.s.l.)</b>	2352.8	2479.8	2402.7	2457.6
<b>Deformation velocity along line-of-sight direction (mm/year)</b>	-26.5	-52.6	-37.3	-4.1
<b>Coherence</b>	0.76	0.63	0.8	0.78

**Table 4.8** The interferometric parameters of the studied points

The type of four selected points are PS, and their coherence values are relatively high. The displacement of each point is shown in **Figure 4.11**. The points in RG1 and RG2 show a high deformation speed along line-of-sight direction but the point in rock glacier 3 doesn't. It indicates that although the three rock glaciers are located geographically close, their motion still varies differently. Like the previous example, the displacement is severe during the freezing seasons but remain relatively stable during the thawing seasons. From all these four displacement time series, the snow cover effect that brought the bumping records in these time series can be clearly observed during the freezing seasons, which are from November to April of the following year. However, from three of the selected four points, we have observed an increment in the annual seasonality. Such phenomenon could be referring to an increment of the water content in the moving body of the rock glaciers due to the warming trend as observed in the time series of the land surface temperature.

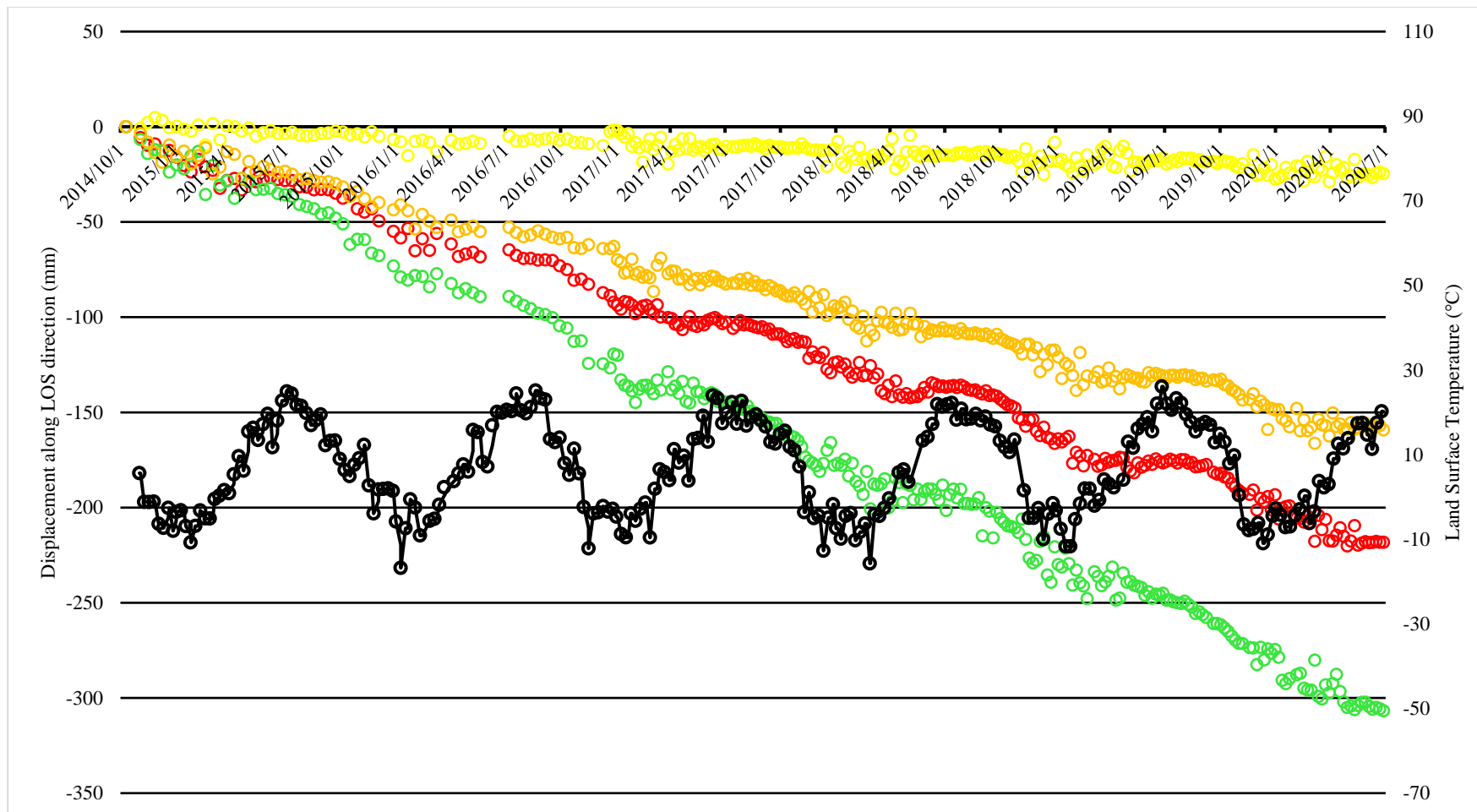


**Figure 4.11** The displacement time series of the studied points in the example 2 and the MODIS 8-day land surface temperature from October 2014 to July 2020

#### 4.3.2. Using ALOS PALSAR L-band differential interferometry to map the active rock glaciers in the late summer season of 2007.

The differential InSAR processing of the ALOS PALSAR images are operated in SNAP 8.0 software. The wrapped differential interferogram generated using L-band ALOS PALSAR images of 2 August 2007 and 17 September 2007 is shown in **Figure 4.12**.

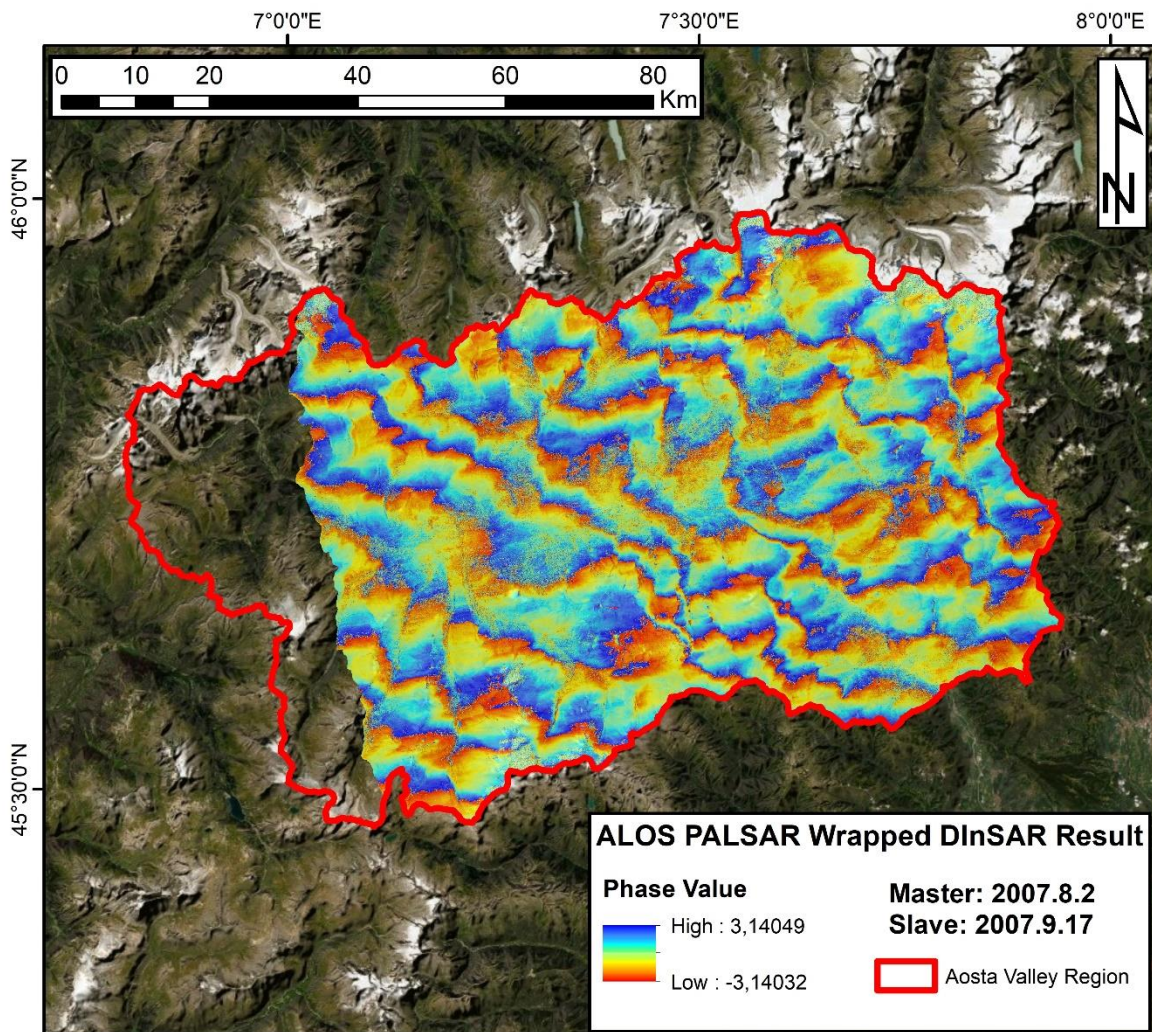


**Figure 4.9** Wrapped ALOS PALSAR 20070802-20070917 differential interferogram.

Among the alpine mountainous geomorphology like VdA Region, multiple errors caused by decorrelation, topography, reference DEM and APS can significantly influence the efficiency of the unwrapping of the interferograms. Also, since the purpose of this research is to use SAR interferometry as a supplementary tool to map the active rock glacier rather than measuring its movement, the differential interferogram is left wrapped.

It should be noted that the imaging frame of ALOS PALSAR sensor used in this research is not completely covering the boundary of VdA Region. The western part of VdA Region is not contained in ALOS PALSAR

data frame, as shown in the **Figure 4.12**. Therefore, through the ALOS DInSAR result, we are not able to access the activity of the rock glaciers located in the west of VdA Region.

The ALOS PALSAR differential interferogram result indicates that from August 2, 2007, to September 17, 2007, with a temporal baseline of 46 days, 107 active rock glaciers were identified and delineated in the intersection area between ALOS PALSAR and the boundary of VdA Region after a double check using the high-resolution optical images provided by Google Earth. To exclude the possible miss categorizing, regional IFFI dataset was also used in the double-check session. At last, 91 of those ALOS PALSAR differential interferograms detected rock glaciers are the same as the inventory dataset provided by regional authorities and 16 additional active rock glaciers were detected, as shown in **Figure 4.13**.

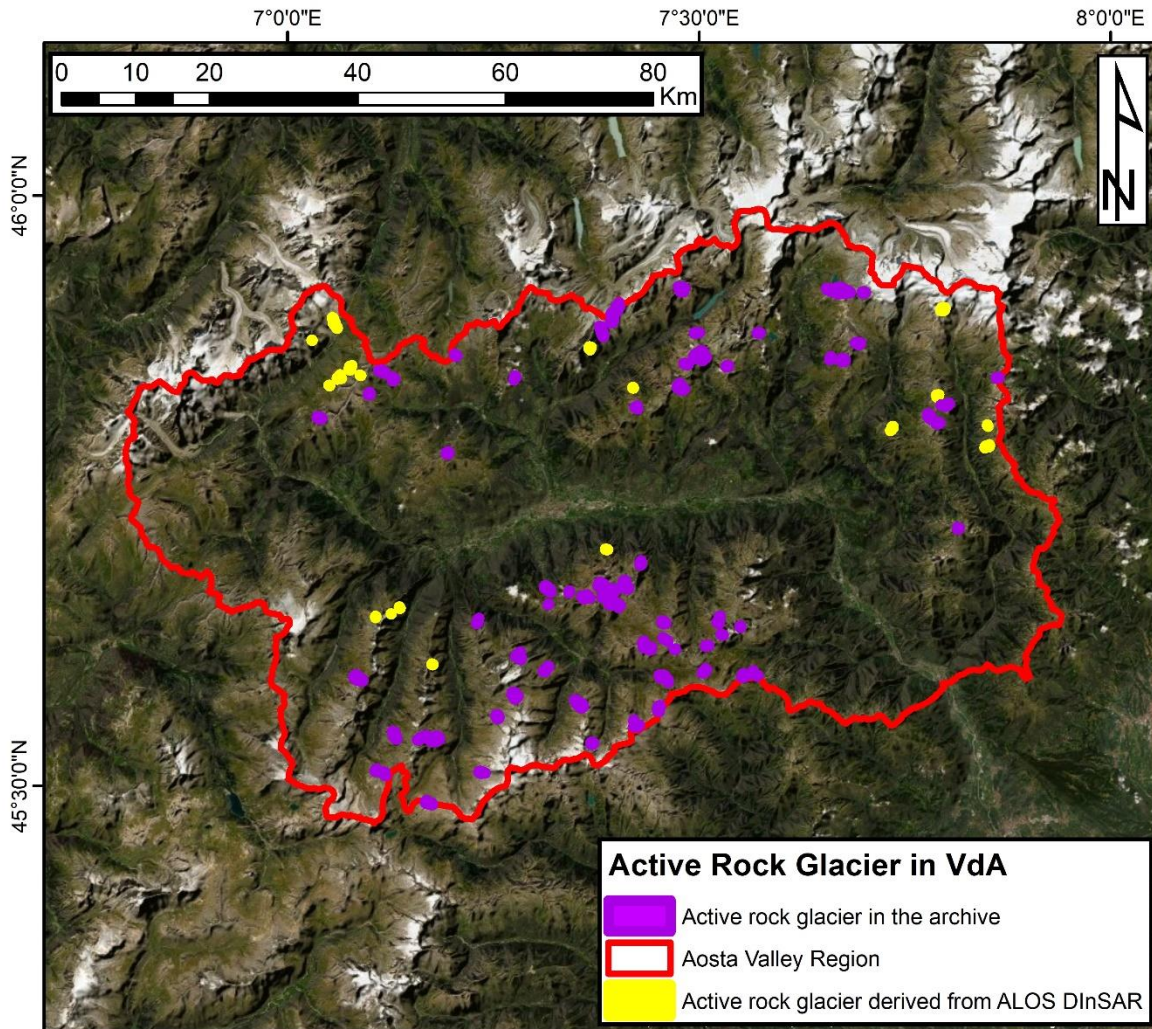


**Figure 4.10** Delineated active rock glaciers using ALOS differential interferogram and Sentinel-1 SqueeSAR™ processing

## 4.4. Discussion

In this work we use multiple methodologies to investigate the activity of the rock glaciers in VdA Region using SAR interferometry.

### 4.4.1. ALOS PALSAR differential interferometry processing and the updated results of active rock glacier mapping

ALOS PALSAR interferograms shown clearer fringes and higher coherence than Sentinel-1 differential interferograms thanks to its longer wavelength and higher spatial resolution. Therefore, in this study, ALOS PALSAR differential interferometry is performed rather than Sentinel-1 differential interferometry processing in the mapping of active rock glaciers in VdA Region. The reasons include its better penetration capacity thanks to longer wavelength of the sensor brings the clearer fringes in the vegetated and snow-covered areas. Secondly, the ALOS PALSAR has a higher spatial resolution of 4 by 9 meters than Sentinel-1's 5 by 20 meters in this case.

From the ALOS PALSAR differential interferogram 107 active rock glaciers were detected. The number is much smaller than the 941 active rock glaciers recorded in the local dataset of field investigation. The reason of that huge difference could be:

- (1) the real fringe that represents the actual displacement obscured with false signals of APS or topography effect.
- (2) no displacement was detected during the imaging time gap, August 2, 2007, to September 17, 2007, in this case.
- (3) some of the active rock glaciers recorded in the local investigation dataset had been fully or partially degraded into inactive rock glaciers from the time that the dataset was delivered till now.

Their displacements are so slow that are not able to be observed using ALOS PALSAR differential interferometry method. But still, 16 additional active rock glaciers in VdA Region were identified by ALOS PALSAR differential interferometry and verified by interpretation of the high resolution optical remote sensing imagery. It indicates the effectiveness of this differential interferometry method in active rock glacier detection. In the future, these 16 newly identified active rock glaciers will be verified by differential interferometry methods using all available SAR data including COSMO-SkyMed, ENVISAT and RADARSAT, etc. And we are aiming to detect more active rock glaciers using differential interferometry method in the future.

Like the case of data shortage of TerraSAR-X images in low-land permafrost analysis in northeastern China, due to the low data quantity (only 14 images in 4 years) that was not available to meet the minimum requirements of advanced multi-temporal InSAR processing including SqueeSAR™ and even SBAS, which usually requires less image acquisitions than SqueeSAR™ processing. Additionally, due to different imaging modes of the sensor (FBS and FBD mode), the multi-temporal SAR interferometry analysis of ALOS PALSAR image stack was not accomplished although the raw SAR data in both FBS and FBD modes shares the same orbit track and imaging frame. It indicates that the seasonality analysis of active rock glacier deformation in VdA Region is unlikely to be accomplished solely using ALOS PALSAR data. The significant land cover change among the freezing and thawing seasons had also influenced the quality of the raw differential interferograms by altering the backscattering characteristics of the ground surface. Therefore, only differential interferograms within the thawing seasons (in this case, from June to September) were formulated, selected, and analyzed using SNAP software. However, the low coherence and noisy fringes obscured our research of thawing seasons of 2008, 2009 and 2010, only remained one pair of available readable differential interferogram from 2 August 2007 to 17 September 2007. The low coherence and poor interferogram quality should be related to the complex APS in the mountainous geomorphology of

VdA Region during thawing seasons. The processing information of the conducted ALOS PALSAR differential interferograms using SNAP software and the corresponding quality assessments are listed in **Table 4.9**.

Interferometric pairs (Bt)	Imaging mode	Pixel size (range*azimuth, in meters)/pixel spacing (in meters)	Processing software	Quality comment
2007.8.2-2007.9.17 (46)	FBD	9.48*4.04/9.37	SNAP	Acceptable, fringes are clear and active rock glaciers are detectable
2008.5.4-2008.6.19 (46)				Extreme low coherence
2009.6.22-2009.8.7 (46)				Low coherence, dense fringes
2009.8.7-2009.9.22 (46)				Low coherence, dense fringes
2009.6.22-2009.9.22 (92)				Low coherence, dense fringes
2010.5.10-2010.6.25 (46)				APS problem

**Table 4.7** Experiment records of ALOS PALSAR differential interferogram processing in VdA Region. The temporal baseline of each interferometric pair is listed in the brackets. The items colored in red refers to the ideal differential interferogram used in the active rock glacier mapping.

#### 4.4.2. Sentinel-1 SqueeSAR™ processing results and the seasonality of active rock glaciers in VdA Region

This research on understanding active rock glacier dynamics in VdA Region is among one of the first researches that discovered such phenomena in a regional scale, thanks to the application of Sentinel-1 SqueeSAR™ processing. The high-frequency and regular revisiting time of Sentinel-1 data as low as 6 days in VdA Region have benefited the SqueeSAR™ processing in this research.

Thanks to the relatively more homogenous landforms and less humid landscape, the Sentinel-1 SqueeSAR™ processing in VdA Region has provided far denser PS/DS distribution than the same processing in the permafrost region of northeastern China. However, compared to the plain geomorphology of low-land permafrost in northeastern China studied in the previous chapter, the deformation analysis to some specific large scale and slow-moving landslides such as Deep-Seated Gravitational Slope Deformation (DSGSD) in the Alpine mountainous regions usually needs to project the line-of-sight displacement into the displacement along the direction of the slope. However, due to its relatively faster movement, smaller volume and more variable surface geomorphologies, such projection is not suggested to being performed in the deformation analysis of active rock glaciers.

Over some fast-moving active rock glaciers, there were few or no PS/DS extracted because of their fast velocity of displacement and horizontal moving direction. It can be solved in the future by the application of pixel offset tracking, using SAR images with higher spatial resolution than Sentinel-1, such as COSMO-SkyMed or TerraSAR-X SAR amplitude images.

The research of a similar purpose of studying the ground deformation processes in high mountain areas conducted in the same region of VdA by Cignetti et al., (2016) applied the SAR data acquired by the sensor of ERS-1/2 from 1992 to 2000 and the data acquired by ENVISAT ASAR sensor from 2002 to 2010. Thanks to the 8-day MODIS land surface temperature data on the Google Earth Engine, the plot of the 8-day MODIS LST time series from January 2004 to January 2011, approximately representing the temporal duration of the ENVISAT ASAR data of the location of the example 1 is shown in **Figure 4.14** and the plot of the 8-day MODIS LST time series from January 2014 to January 2021 that representing the sensing time of Sentinel-1 sensor in this research is shown in **Figure 4.15** as a compare. According to the results of linear regression, the land surface temperature has shown a slightly increasing trend from January 2014 to January 2021, rather than the slightly decreasing trend from January 2004 to January 2011. By another comparison from the displacement map of this research and the result that was shown in the research of Cignetti et al., (2016), the La Clapey Gerbioz rock glacier was recorded as relict from the ENVISAT ASAR SBAS displacement result, which is different from the obvious significant deformation shown in **Figure 4.8**. Therefore, it would be reasonable to assume that the deformation of La Clapey Gerbioz rock glacier is due to the increasing temperature in the rock glacier body.

The seasonality is identified from the displacement histograms generated by SqueeSAR™ analysis. From the deformation results of SqueeSAR™ analysis, during freezing seasons in VdA Region, it is revealed that over some active rock glaciers, the ground had shown a phenomenon of faster subsidence, rather than remaining stable or slightly uplifting due to the freezing processes in low temperature during winter seasons, December to March especially, as shown in the two examples of last chapter. It indicates a half-year time lapse from the dynamics of the Mean Annual Air Temperature. Such observation is not aligned with the observations listed in Strozzi et al., (2020), which is a similar research that monitored and analyzed the dynamic of rock glacier in Switzerland Alps, western Greenland, and Argentinian Andes. The reason is needed to be thoroughly studied in the future.



**Figure 4.15** shows the displacement time series of the points studied in the example 1 (La Clapey Gerbioz rock glacier) and the monthly ERA5 precipitation time series data from November 2014 to July 2020, and **Figure 4.16** shows the displacement time series of the studied points in the example 2 and the monthly ERA5 precipitation time series data from October 2014 to July 2020. As a contrast, the monthly ERA5 precipitation time series data has not shown to be coefficient with the displacement time series of the active rock glaciers.

The seasonality is not calculated mathematically, just identified by the displacement histogram is because some of the displacements are altered by the false signal caused by snow coverage during winter season. The penetration capacity of microwave into the snow depends on the wavelength of the sensor and the humidity of the snow, which is hard to determine using remote sensing methods. From the histograms, different from the Sentinel-1 SqueeSAR™ time series of displacements in northeastern China, bumpy displacement records caused by snow cover have been observed during winter seasons. That will cause the wrong identification in autocorrelation analysis, which is an important step while calculating the seasonality. We have not found perfect and uniformed criteria for the removal of the bumpy records caused by the snow during winter. It is a challenge while quantifying the seasonality. Therefore, manual check is still mandatorily needed in the interpretation of seasonality of active rock glaciers in VdA Region in this research. In the future we are aiming to calculate the seasonality of those observed time series of displacements of the detected active rock glaciers mathematically after finding out a method to eliminate those noisy displacement records caused by the winter snow.

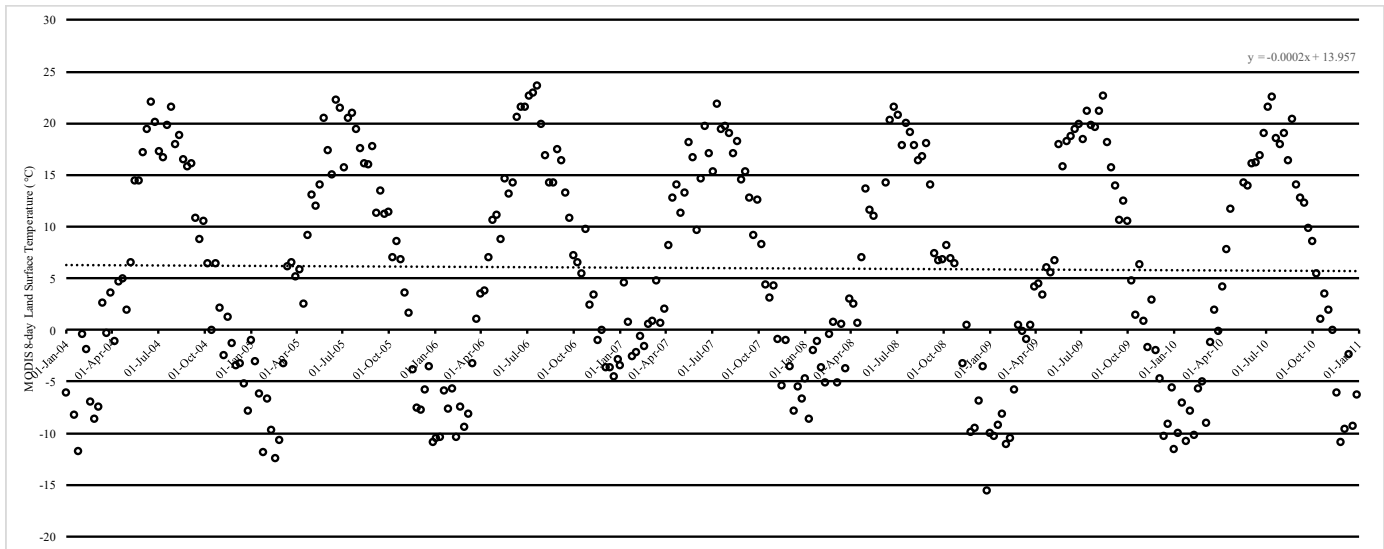


**Figure 4.14** MODIS 8-day Land Surface Temperature at La Clapey Gerbioz rock glacier, January 2004 to January 2011.

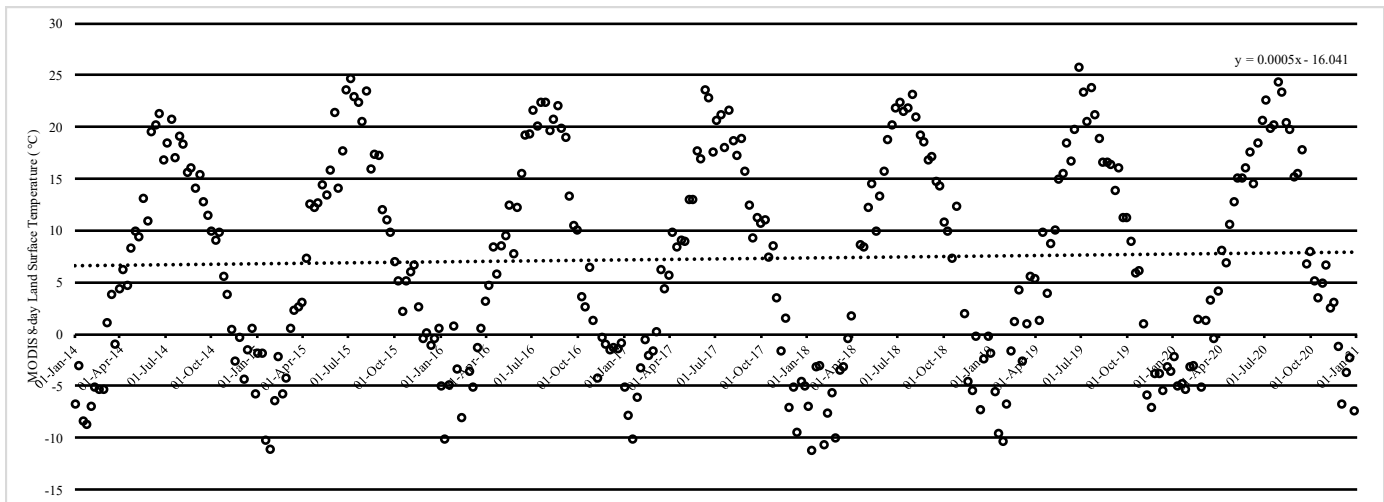


**Figure 4.15** MODIS 8-day Land Surface Temperature at La Clapey Gerbioz rock glacier, January 2014 to January 2021.

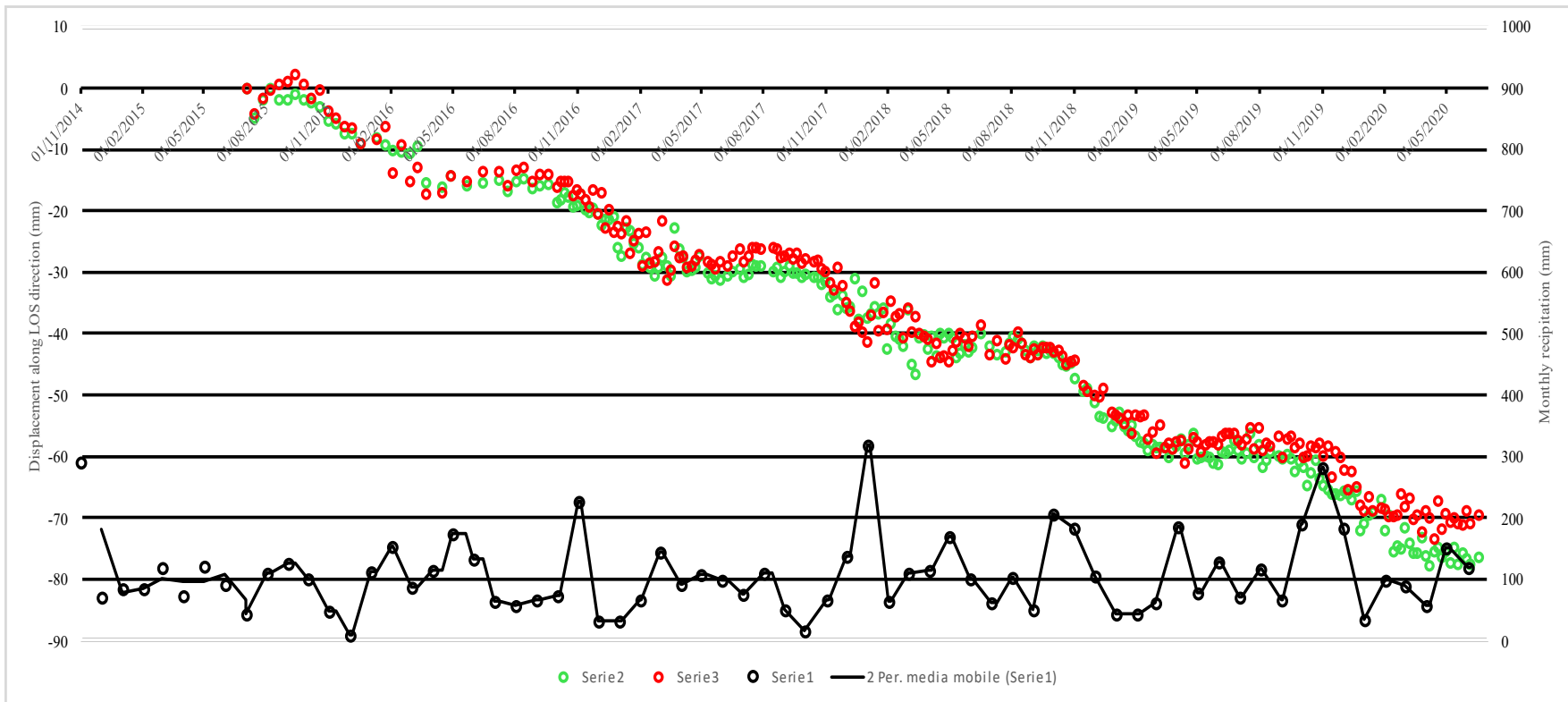


**Figure 4.16** The displacement time series of the studied points in the La Clapey Gerbioz rock glacier case study and ERA5 monthly aggregated precipitation data from November 2014 to July 2020

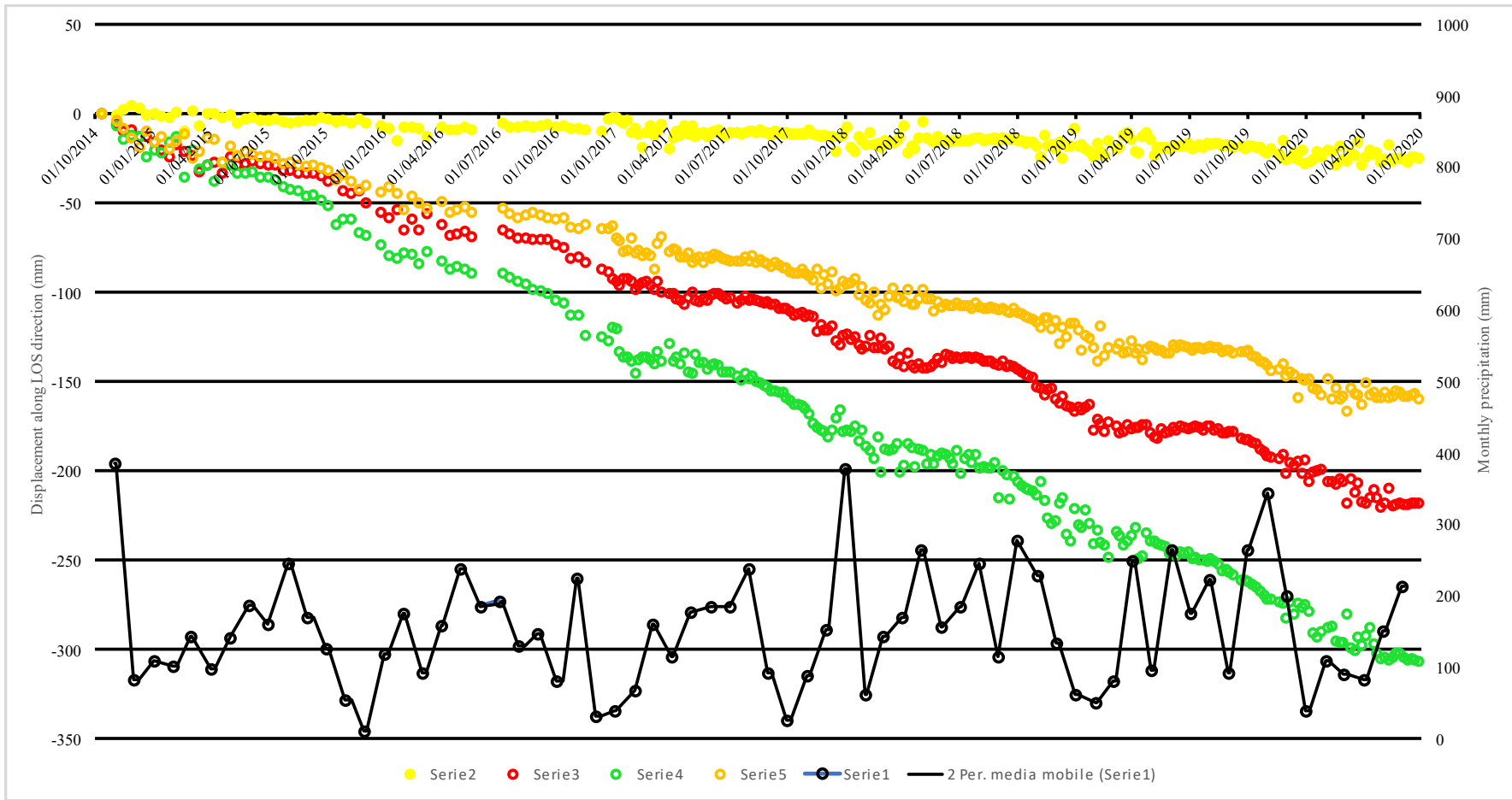


**Figure 4.17** The displacement time series of the studied points in the example 2 and ERA5 monthly aggregated precipitation data from October 2014 to July 2020

## Chapter 5. Conclusion and Future Recommendations

This PhD work was developed on two study sites: sporadic low-land permafrost-distributed region in northeastern China and alpine Aosta Valley Region in northwestern Italy, focusing on the subsidence signal detection in the periglacial landforms in cold regions using DInSAR and advanced SqueeSAR™ techniques with an in-detail interpretation of the displacement results. This work has demonstrated the feasibility and the potential of SAR interferometry in deformation phenomena related studies in cold regions.

From the C-band Sentinel-1 SqueeSAR™ result of low-land permafrost region in northeastern China, a few significant deformation events can be identified and monitored around man-made infrastructures and bare soils. The displacement hotspot can hardly be detected in those places with dense vegetation because of the low density of PS/DS due to the low capacity of vegetation canopy penetration of C-band microwave. The potential distribution of permafrost degradation is mapped using L-band ALOS PALSAR InSAR analysis. Although the L-band microwave can better penetrate the canopy and L-band ALOS PALSAR SqueeSAR™ result provides a higher density of PS/DS coverage in the same study area, the temporal resolution is too limited to provide a full inter-annual displacement to reveal the full seasonality of the ground deformation. In the future, combined with advanced multi-temporal InSAR processing algorithms like SqueeSAR™, P-SBAS, CPT, etc., SAR data collected by other L-band SAR sensors with more frequent revisit cycles in the future projects will be much more helpful than current C-band Sentinel-1 and L-band ALOS PALSAR in the monitoring of ground deformation in low-land permafrost regions of northeastern China. Additionally, to enhance the interferometric coherence in high geological hazard prone areas due to the dense distribution of the vegetation, the installation of corner reflectors is demonstrated to be useful in the increment of backscattering signal to the SAR sensor, therefore, to formulate higher coherence values, clearer fringes, and more PS/DS targets.

However, the reason of the extreme high coherence from Sentinel-1 DInSAR and SqueeSAR™ during winter seasons, even though there normally has thick snow coverage been left unsolved, which would be crucial in the research of permafrost environment. One possible explanation could be the imaging time of the Sentinel-1 sensor is always around 5 a.m. (GMT 21:00, GMT+8). During the winter season the local air temperature at 5 a.m. in the study area is always as low as -30°C according to the local weather record, which is the lowest of the day. With the extreme low air temperature, and without too much solar radiation, the surface water and the water trapped in the snow patches were remained frozen, which helped to reduce the moisture of the snow patch, and then to increase the interferometric coherence by an enhancement of the microwave penetration. It needs to be well studied in the future, probably on-site with field measurements of snow or soil moisture time series monitoring.

The C-band Sentinel-1 SqueeSAR™ results of the rock glaciers in Aosta Valley Region of northwestern Italy have provided the full dynamics of the rock glaciers with acceptable spatial and temporal resolution. The activeness of the rock glaciers is evaluated using the factor of velocity from the displacement time series result of SqueeSAR™ results of Aosta Valley Region combining with the regional rock glacier delineation map using high-resolution optical imagery, but still, some of the extremely fast-moving and horizontal-moving rock glaciers during some specific seasons are not identified from the SqueeSAR™ result due to the limitation of interferometry theory. Although having shown much clearer fringes than the Sentinel-1 differential interferograms, thanks to its longer wavelength and higher spatial resolution, L-band ALOS PALSAR differential interferometry result only indicates the activeness of rock glaciers during two specific dates in one summer. Due to the shortage of the ALOS PALSAR image quantity, we are not able to fully achieve the research object of “using ALOS PALSAR interferometry to investigate the distribution of active rock glacier in Aosta Valley Region”. We hope other L-band SAR data with higher revisiting cycle can help

to solve this research object in the future. New generation L-band sensors, such as ALOS-2, NISAR and SAOCOM with more frequent revisit period and higher spatial resolution will help in the detection of fringes and PS/DS targets, obtaining more information of the displacements occurring in the cold regions.

Some rock glaciers have shown a more severe subsidence phenomenon during freezing seasons including late autumn, winter and early spring (for example, from late November to early March), and such subsidence phenomenon is less severe in the warmer seasons of late spring, summer and early autumn (for example, from May to September), which is reverse to the conventional understanding of the freeze-and-thaw cycle conceptual model and our first research of the low-land permafrost in northeastern China in this PhD work. Some research indicates that the ascending air circulation along the slope could be one of the major reasons for the unexpected subsidence in the winter season (Delaloye & Lambiel, 2005). In the future, we are looking forward to comparing the SqueeSAR™, GBInSAR, GNSS and LiDAR displacement time series results, first to validate the accuracy from SqueeSAR™ processing, then to find out the reason to understand such phenomenon by investigating individual rock glaciers with such typical phenomenon using GBInSAR analysis (Zahs et al., 2019) in Aosta Valley Region.

Pixel Offset Tracking (POT) method using X-band TerraSAR-X or COSMO-SkyMed SAR data to monitor rapid horizontal periglacial movements including rock glaciers, glaciers, moraines, and rock debris in Alpine cold regions will be helpful in the understanding of rock glacier dynamics in another dimension, rather than solely relying on regional SqueeSAR™ analysis.

The application of radar interferometry to different case studies in cold regions has allowed us to critically evaluate both strengths and shortcomings. The traditional differential interferometric analysis achieved the qualitative studies of deformation area locating and mapping, meanwhile multi-temporal InSAR, SqueeSAR™ specifically in this research, achieved the quantitative studies in this research. Despite the limitations of SAR application, a combination between traditional DInSAR and multi-temporal InSAR analysis will contribute to geological hazard and ground deformation related studies, especially in cold regions where have strong seasonality changes in landscape and sparsely distributed PS/DS targets. In the future, we are looking forward to integrating the multi-temporal InSAR time series of displacement data into the early warning systems of landslide and infrastructure monitoring in the regional or local-scaled projects for the purpose of geological hazard mitigation on behalf of public administration.

## Acknowledgement

First of all, I would like to thank my supervisors, Professor Nicola Casagli and Doctor Silvia Bianchini for providing me such a great opportunity of this PhD at the Department of the Earth Sciences of the University of Florence and consistent constructive advices in this work. Without you, I wouldn't have such amazing experiences during the past years in a foreign country far away from home.

Secondly, I would like to be sincerely grateful to all my colleagues and friends in the remote sensing group, especially Doctor Federico Raspini, Doctor Matteo Del Soldato, Doctor Pierluigi Confuorto and Doctor Lorenzo Solari. They helped me in every aspect of my researches in detail with patience, having inspired and encouraged me to realize all my big and small thoughts and ideas based on their professional knowledges and various experiences. It has been a great honor for me to acknowledge those good and kind-hearted colleagues.

Special thanks to my external supervisors Doctor Fernando Bellotti, Doctor Marco Basilico and the company CEO, Doctor Alessandro Ferretti from TRE-Altamira who welcomed me into their company during my four-month internship in Milan. They devoted contribution in the SqueeSAR™ data processing and result quality insurance sessions of this work. Their outstanding professionalism, wisdom and craftsmanship in the career and critical supervision made me benefit so much.

Last but not least, I would to say a big, big thank you to my families for all the sacrifices, kind, long-term support and the most important, for giving me this opportunity to pursue this PhD abroad.

## Chapter 6. Reference

- Azócar, G. (2016). Permafrost Favorability Index Map (PFI), Bremerhaven, PANGAEA.
- Azócar, G. F., Brenning, A., & Bodin, X. (2017). Permafrost distribution modelling in the semi-arid Chilean Andes. *The Cryosphere*, 11, 877–890. <https://doi.org/10.5194/tc-11-877-2017>
- Bamler, R., & Hartl, P. (1998). Synthetic aperture radar interferometry Synthetic aperture radar interferometry. *Inverse Problems*, 14(4).
- Barbieri, M., & Lichtenegger, J. (2005). Introduction to SAR for Geology. *Spaceborne radar applications in Geology; ESA TM-17*, 1-54.
- Bartsch, A., Grosse, G., Kääh, A., Westermann, S., Strozzi, T., Wiesmann, A., Duguay, C., Seifert, F.M., Obu, J., & Goler, R. (2016). GlobPermafrost – how space-based earth observation supports understanding permafrost. *Proc. Living Planet Symposium*, Prague, Czech Republic, 9–13 May 2016, 740, 332.
- Barboux, C., Delaloye, R., & Lambiel, C. (2014). Inventorying slope movements in an Alpine environment using DInSAR. *Earth Surface Processes and Landforms*, 39(15), 2087–2099. <https://doi.org/10.1002/esp.3603>
- Barsch, D. (1996). Rockglaciers: Indicators for the Present and Former Geoecology in High Mountain Environments in Springer Series in Physical Environment, edited by Barsch, D. 1–331. Berlin, Germany: Springer Verlag.
- Bellotti, F., Bianchi, M., Colombo, D., Ferretti, A., & Tamburini, A. (2014). Advanced InSAR Techniques to Support Landslide Monitoring. *Mathematics of Planet Earth. Lecture Notes in Earth System Sciences*, Springer, Berlin, Heidelberg. [https://doi.org/10.1007/978-3-642-32408-6\\_64](https://doi.org/10.1007/978-3-642-32408-6_64)
- Berardino, P., Fornaro, G., Lanari, R., & Sansosti, E. (2002). A new Algorithm for Surface Deformation Monitoring based on Small Baseline Differential SAR Interferograms. *IEEE Transactions on Geoscience and Remote Sensing*, 2002, 40(11), 2375-2383. <https://doi.org/10.1109/TGRS.2002.803792>
- Brencher, G., Handwerger, A., & Munroe, J. (2020). InSAR-based characterization of rock glacier movement in the Uinta Mountains, Utah, USA. *The Cryosphere Discussions*, (December), 1–36. <https://doi.org/10.5194/tc-2020-274>
- Brown, J., Hinkel K.M., & Nelson F.E. (2000). The circumpolar active layer monitoring (calm) program: Research designs and initial results, *Polar Geography*. 24:3, 166-258. <https://doi.org/10.1080/10889370009377698>



- Brown, J., Ferrians, O., Heginbottom, J.A., & Melnikov, E. (2002). *Circum-Arctic Map of Permafrost and Ground-Ice Conditions, Version 2*. Boulder, Colorado USA. NSIDC: National Snow and Ice Data Center. <https://doi.org/10.7265/skbg-kf16>
- Capes, R., & Marsh, S. (2009). *TerraFirma User Guide*. <https://doi.org/10.13140/RG.2.2.16889.88161>
- Carlà, T., Tofani, V., Lombardi, L., Raspini, F., Bianchini, S., Bertolo, D., Thuegaz, P., & Casagli, N. (2019). Combination of GNSS, satellite InSAR, and GBInSAR remote sensing monitoring to improve the understanding of a large landslide in high alpine environment. *Geomorphology*, 335, 62–75. <https://doi.org/10.1016/j.geomorph.2019.03.014>
- Casu, F., Manzo, M., & Lanari, R. (2006). A quantitative assessment of the SBAS algorithm performance for surface deformation retrieval from DInSAR data. *Remote Sensing of Environment*, 102(3–4), 195–210. <https://doi.org/10.1016/j.rse.2006.01.023>
- Chang, L., & Hanssen, R. F. (2015). Detection of permafrost sensitivity of the Qinghai–Tibet railway using satellite radar interferometry. *International Journal of Remote Sensing*, 36(3), 691–700. <https://doi.org/10.1080/01431161.2014.999886>
- Cheng, G., & Wu, T. (2007). Responses of permafrost to climate change and their environmental significance, Qinghai-Tibet Plateau. *Journal of Geophysical Research: Earth Surface*, 112(2), 1–10. <https://doi.org/10.1029/2006JF000631>
- Christensen, T. R., Johansson, T., Åkerman, H. J., Mastepanov, M., Malmer, N., Friborg, T., Crill, P., & Svensson, B. H. (2004). Thawing sub-arctic permafrost: Effects on vegetation and methane emissions. *Geophysical Research Letters*, 31(4). <https://doi.org/10.1029/2003GL018680>
- Cignetti, M., Manconi, A., Manunta, M., Giordan, D., De Luca, C., Allasia, P., & Ardizzone, F. (2016). Taking advantage of the ESA G-POD service to study ground deformation processes in high mountain areas: A Valle d’Aosta case study, Northern Italy. *Remote Sensing*, 8(10), 852. <https://doi.org/10.3390/rs8100852>
- Colesanti, C., Ferretti, A., Prati, C., & Rocca, F. (2003). Monitoring landslides and tectonic motions with the Permanent Scatterers Technique. *Engineering Geology*, 68(1–2), 3–14. [https://doi.org/10.1016/S0013-7952\(02\)00195-3](https://doi.org/10.1016/S0013-7952(02)00195-3)
- Confuorto, P. (2016). From site-scale to large areas monitoring of ground deformation phenomena by integration of different DInSAR techniques in Crotone Province (Southern Italy). Ph.D. thesis, University of Naples Federico II, Naples
- Crosetto, M., Monserrat, O., Cuevas-González, M., Devanthéry, N., & Crippa, B. (2016). Persistent Scatterer Interferometry: A review. *ISPRS Journal of Photogrammetry and Remote Sensing*, 115, 78–89. <https://doi.org/10.1016/j.isprsjprs.2015.10.011>
- Crozier, M. J., & Glade, T. (2012). *Landslide Hazard and Risk: Issues, Concepts and Approach*. *Landslide Hazard and Risk*. <https://doi.org/10.1002/9780470012659.ch1>
- Crozier, M. J. (2010). Deciphering the effect of climate change on landslide activity: A review. *Geomorphology*, 124(3–4), 260–267. <https://doi.org/10.1016/j.geomorph.2010.04.009>

- Cruden, D. M. (1991). A simple definition of a landslide. *Bulletin of the International Association of Engineering Geology - Bulletin de l'Association Internationale de Géologie de l'Ingénieur*, 43(1), 27–29. <https://doi.org/10.1007/BF02590167>
- Cruden, D. M., & Varnes, D. J. (1996). *LANDSLIDE TYPES AND PROCESSES. Landslides: Investigation and Mitigation, Transportation Research Board Special Report 247, Washington D.C.*
- Daout, S., Doin, M. P., Peltzer, G., Socquet, A., & Lasserre, C. (2017). Large-scale InSAR monitoring of permafrost freeze-thaw cycles on the Tibetan Plateau. *Geophysical Research Letters*, 44(2), 901–909. <https://doi.org/10.1002/2016GL070781>
- Delaloye, R. & Lambiel, C. (2005). Evidence of winter ascending air circulation throughout talus slopes and rock glaciers situated in the lower belt of alpine discontinuous permafrost (Swiss Alps), *Norsk Geografisk Tidsskrift - Norwegian Journal of Geography*. 59(2), 194-203. <https://doi.org/10.1080/00291950510020673>
- Delaloye, R., Strozzi, T., Lambiel, C., Perruchoud, E., & Raetzo, H. (2008). Landslide-like development of rockglaciers detected with ERS-1/2 SAR interferometry. *Proceedings ESA FRINGE Symposium 2007*.
- Eppler, J., Kubanski, M., Sharma, J., & Busler, J. (2015). High temporal resolution permafrost monitoring using a multiple stack InSAR technique. *International Archives of the Photogrammetry, Remote Sensing and Spatial Information Sciences - ISPRS Archives*, 40(7W3), 1171–1176. <https://doi.org/10.5194/isprsarchives-XL-7-W3-1171-2015>
- Ferretti, A., Prati, C., & Rocca, F. (2000). Nonlinear subsidence rate estimation using permanent scatterers in differential SAR interferometry. *IEEE Transactions on Geoscience and Remote Sensing*, 38(5-1), 2202–2212. <https://doi.org/10.1109/36.868878>
- Ferretti, A., Prati, C., & Rocca, F. (2001). Permanent scatterers in SAR interferometry. *IEEE Transactions on Geoscience and Remote Sensing*, 39(1), 8–20. <https://doi.org/10.1109/36.898661>
- Ferretti, A., Fumagalli, A., Novali, F., Prati, C., Rocca, F., & Rucci, A. (2011). A new algorithm for processing interferometric data-stacks: SqueeSAR. *IEEE Transactions on Geoscience and Remote Sensing*, 49(9), 3460–3470. <https://doi.org/10.1109/TGRS.2011.2124465>
- Ferretti, A., Bellotti, F., Alberti, S., Allievi, J., Del Conte, S., Tamburini, A., Tamburini, A., Broccolato, M., Ratto, S., & Alberto, W. (2011). Landslide Mapping Using SqueeSAR Data. In *AGU Fall Meeting Abstracts* (Vol. NH51C-05).
- French, H.M. (2017). *The periglacial environment*. John Wiley & Sons. <https://doi.org/10.1002/9781118684931>
- Froude, M. J., & Petley, D. N. (2018). Global fatal landslide occurrence from 2004 to 2016. *Natural Hazards and Earth System Sciences*, 18(8), 2161–2181. <https://doi.org/10.5194/nhess-18-2161-2018>
- Gabriel, A.K., & Goldstein, R. (1988). Crossed orbit interferometry: theory and experimental results from SIR-B. *International Journal of Remote Sensing*, 9, 857-872.

- Gabriel, A. K., Goldstein, R. M., & Zebker, H. A. (1989). Mapping small elevation changes over large areas: differential radar interferometry. *Journal of Geophysical Research*, 94(B7), 9183–9191. <https://doi.org/10.1029/JB094iB07p09183>
- Haeberli, W., Hallet, B., Arenson, L., Elconin, R., Humlum, O., Käab, A., Kaufmann, V., Ladanyi, B., Matsuoka, N., Springman, S., & Mühll, D.V. (2006). Permafrost creep and rock glacier dynamics. *Permafrost Periglacial Process*, 17, 189-214. <https://doi.org/10.1002/ppp.561>
- Haeberli, W., Schaub, Y., & Huggel, C. (2017). Increasing risks related to landslides from degrading permafrost into new lakes in de-glaciating mountain ranges. *Geomorphology*, 293, 405–417. <https://doi.org/10.1016/j.geomorph.2016.02.009>
- Hanssen, R. F. (2001). *Radar Interferometry: Data Interpretation and Error Analysis*. Springer Science & Business Media.
- Brown, J., Ferrians Jr., O. J., Heginbottom, J. A., & Melnikov, E. S. (1997). Circum-Arctic Map of Permafrost and Ground Ice Conditions. In *USGS Numbered Series* (Vol. 2, p. 1). Retrieved from <http://pubs.usgs.gov/cp/45/plate-1.pdf>
- Heginbottom, J. A., Brown, J., Ferrians Jr., O.J., & Melnikov, E.S. (1993). Circum-Arctic Map of Permafrost and Ground Ice Conditions. *Permafrost: Sixth International Conference, Beijing, Proceedings. Wushan, Guangzhou, China*. South China University Press. 2, 1132- 1136.
- Herrera, G., Gutiérrez, F., García-Davalillo, J. C., Guerrero, J., Notti, D., Galve, J. P., Fernández-Merodo, J.A., & Cooksley, G. (2013). Multi-sensor advanced DInSAR monitoring of very slow landslides: The Tena Valley case study (Central Spanish Pyrenees). *Remote Sensing of Environment*, 128, 31–43. <https://doi.org/10.1016/j.rse.2012.09.020>
- Hock, R., & Rasul, G., (2019). Chapter 2: High Mountain Areas. *IPCC Special Report on the Ocean and Cryosphere in a Changing Climate*, 131–202.
- Hooper, A., Zebker, H., Segall, P., & Kampes, B. (2004). A new method for measuring deformation on volcanoes and other natural terrains using InSAR persistent scatterers. *Geophysical Research Letters*, 31(23), 1–5. <https://doi.org/10.1029/2004GL021737>
- Hooper, A. (2006). Persistent scatterer radar interferometry for crustal deformation studies and modeling of volcanic deformation, Ph.D. thesis, Stanford University, Stanford
- Hooper, A. J. (2008). A multi-temporal InSAR method incorporating both persistent scatterer and small baseline approaches. *Geophysical Research Letters*, 35(16), 1–5. <https://doi.org/10.1029/2008GL034654>
- Hooper, A., Bekaert, D., Spaans, K., & Arikan, M. (2012). Recent advances in SAR interferometry time series analysis for measuring crustal deformation. *Tectonophysics*, 514–517, 1–13. <https://doi.org/10.1016/j.tecto.2011.10.013>
- Huggel, C., Clague, J. J., & Korup, O. (2012). Is climate change responsible for changing landslide activity in high mountains? *Earth Surface Processes and Landforms*, 37(1), 77–91. <https://doi.org/10.1002/esp.2223>

- Ikeda, A., & Matsuoka, N. (2002). Degradation of talus-derived rock glaciers in the upper engadin, Swiss alps. *Permafrost and Periglacial Processes*, 13(2), 145–161. <https://doi.org/10.1002/ppp.413>
- Imaizumi, F., Nishiguchi, T., Matsuoka, N., Trappmann, D., & Stoffel, M. (2018). Interpretation of recent alpine landscape system evolution using geomorphic mapping and L-band InSAR analyses. *Geomorphology*, 310, 125–137. <https://doi.org/10.1016/j.geomorph.2018.03.013>
- Kääb, A., Haeberli, W., & Hilmar Gudmundsson, G. (1997). Analysing the creep of mountain permafrost using high precision aerial photogrammetry: 25 years of monitoring Gruben rock glacier, Swiss Alps. *Permafrost and Periglacial Processes*, 8(4), 409–426. [https://doi.org/10.1002/\(SICI\)1099-1530\(199710/12\)8:4<409::AID-PPP267>3.0.CO;2-C](https://doi.org/10.1002/(SICI)1099-1530(199710/12)8:4<409::AID-PPP267>3.0.CO;2-C)
- Kääb, A., & Kneisel, C. (2006). Permafrost creep within a recently deglaciated glacier forefield: Muragl, Swiss Alps. *Permafrost and Periglacial Processes*, 17(1), 79–85. <https://doi.org/10.1002/ppp.540>
- Kenyi, L. W., & Kaufmann, V. (2003). Estimation of rock glacier surface deformation using SAR interferometry data. *IEEE Transactions on Geoscience and Remote Sensing*, 41(6 PART II), 1512–1515. <https://doi.org/10.1109/TGRS.2003.811996>
- Kharuk, V. I., Shushpanov, A. S., Im, S. T., & Ranson, K. J. (2016). Climate-induced landsliding within the larch dominant permafrost zone of central Siberia. *Environmental Research Letters*, 11(4). <https://doi.org/10.1088/1748-9326/11/4/045004>
- Korup, O., Densmore, A. L., & Schlunegger, F. (2010). The role of landslides in mountain range evolution. *Geomorphology*, 120(1–2), 77–90. <https://doi.org/10.1016/j.geomorph.2009.09.017>
- Korup, O., Montgomery, D. R., & Hewitt, K. (2010). Glacier and landslide feedbacks to topographic relief in the Himalayan syntaxes. *Proceedings of the National Academy of Sciences of the United States of America*, 107(12), 5317–5322. <https://doi.org/10.1073/pnas.0907531107>
- Krainer, K., & Mostler, W. (2000). Reichenkar rock glacier: A glacier derived debris-ice system in the western Stubai Alps, Austria. *Permafrost and Periglacial Processes*, 11(3), 267–275. [https://doi.org/10.1002/1099-1530\(200007/09\)11:3<267::AID-PPP350>3.0.CO;2-E](https://doi.org/10.1002/1099-1530(200007/09)11:3<267::AID-PPP350>3.0.CO;2-E)
- Lagios, E., Sakkas, V., Novali, F., Bellotti, F., Ferretti, A., Vlachou, K., & Dietrich, V. (2013). SqueeSAR™ and GPS ground deformation monitoring of Santorini Volcano (1992-2012): Tectonic implications. *Tectonophysics*, 594, 38–59. <https://doi.org/10.1016/j.tecto.2013.03.012>
- Lanari, R., Casu, F., Manzo, M., Zeni, G., Berardino, P., Manunta, M., & Pepe, A. (2007). An overview of the Small BAseline Subset algorithm: A DInSAR technique for surface deformation analysis. *Pure and Applied Geophysics*, 164(4), 637–661. <https://doi.org/10.1007/s00024-007-0192-9>
- Lanari, R., Mora, O., Manunta, M., Mallorquí, J. J., Berardino, P., & Sansosti, E. (2004). A small-baseline approach for investigating deformations on full-resolution differential SAR interferograms. *IEEE Transactions on Geoscience and Remote Sensing*, 42(7), 1377–1386. <https://doi.org/10.1109/TGRS.2004.828196>
- Lilleøren, K. S., Etzelmüller, B., Gärtner-Roer, I., Kääb, A., Westermann, S., & Gudmundsson, Á. (2013). The Distribution, Thermal Characteristics and Dynamics of Permafrost in Tröllaskagi, Northern Iceland,

- as Inferred from the Distribution of Rock Glaciers and Ice-Cored Moraines. *Permafrost and Periglacial Processes*, 24, 322–335. <https://doi.org/10.1002/ppp.1792>
- Liu, L., Millar, C. I., Westfall, R. D., & Zebker, H. A. (2013). Surface motion of active rock glaciers in the Sierra Nevada, California, USA: Inventory and a case study using InSAR. *Cryosphere*, 7, 1109–1119. <https://doi.org/10.5194/tc-7-1109-2013>
- Lugon, R., Delaloye, R., Serrano, E., Reynard, E., Lambiel, C., & González-Trueba, J. J. (2004). Permafrost and Little Ice Age glacier relationships, posets massif, central Pyrenees, Spain. *Permafrost and Periglacial Processes*, 15(3), 207–220. <https://doi.org/10.1002/ppp.494>
- Lugon, R., & Stoffel, M. (2010). Rock-glacier dynamics and magnitude-frequency relations of debris flows in a high-elevation watershed: Ritigraben, Swiss Alps. *Global and Planetary Change*, 73, 202–210. <https://doi.org/10.1016/j.gloplacha.2010.06.004>
- Massonnet, D., & Feigl, K. L. (1998). Radar interferometry and its application to changes in the earth's surface. *Reviews of Geophysics*, 36, 441–500. <https://doi.org/10.1029/97RG03139>
- Matsuoka, N. (2001). Solifluction rates, processes and landforms a global review. *Earth-Science Reviews*, 55, 107–134. [https://doi.org/10.1016/S0012-8252\(01\)00057-5](https://doi.org/10.1016/S0012-8252(01)00057-5)
- Nagler, T., Rott, H., & Kamelger, A. (2002). Analysis of landslides in Alpine areas by means of SAR interferometry. *International Geoscience and Remote Sensing Symposium (IGARSS)*, 1, 198–200. <https://doi.org/10.1109/igarss.2002.1024986>
- Necsoiu, M., Onaca, A., Wigginton, S., & Urdea, P. (2016). Rock glacier dynamics in Southern Carpathian Mountains from high-resolution optical and multi-temporal SAR satellite imagery. *Remote Sensing of Environment*, 177, 21–36. <https://doi.org/10.1016/j.rse.2016.02.025>
- Nelson, F. E., Anisimov, O. A., & Shiklomanov, N. I. (2002). Climate change and hazard zonation in the circum-arctic permafrost regions. *Natural Hazards*, 26(3), 203–225. <https://doi.org/10.1023/A:1015612918401>
- Noetzli, J. & Vonder Muehll, D. (2010). Permafrost in Switzerland 2006/2007 and 2007/2008. Glaciological Report Permafrost No. 8/9, Cryospheric Commission of the Swiss Academy of Sciences (SCNAT).
- Ortiz, M.D. (2017). Remote Sensing of Open Water Fraction and Melt Ponds in the Beaufort Sea Using Machine Learning Algorithms, Ph.D. thesis, University of Miami, Miami
- Otto, J.C., Schrott, L., Jaboyedoff, M., & Dikau, R. (2009). Quantifying sediment storage in a high alpine valley (Turtmannal, Switzerland). *Earth Surface Processes and Landforms*, 34, 1726–1742. <https://doi.org/10.1002/esp.1856>
- Outcalt, S. I., Arbor, A., Nelson, F. E., & Hinkel, K. M. (1990). Region in Freezing Soil. *Water Resources*, 26(7), 1509–1516.

- Pham, T. D., Yokoya, N., Bui, D. T., Yoshino, K., & Friess, D. A. (2019). Remote sensing approaches for monitoring mangrove species, structure, and biomass: Opportunities and challenges. *Remote Sensing*, *11*(230). <https://doi.org/10.3390/rs11030230>
- Ran, Y., Li, X., Cheng, G., Zhang, T., Wu, Q., Jin, H., & Jin, R. (2012). Distribution of Permafrost in China: An Overview of Existing Permafrost Maps. *Permafrost and Periglacial Processes*, *23*, 322–333. <https://doi.org/10.1002/ppp.1756>
- Raspini, F., Bianchini, S., Ciampalini, A., Del Soldato, M., Solari, L., Novali, F., ... Casagli, N. (2018). Continuous, semi-automatic monitoring of ground deformation using Sentinel-1 satellites. *Scientific Reports*, *8*(7253), 1–11. <https://doi.org/10.1038/s41598-018-25369-w>
- Raspini, F., Bianchini, S., Ciampalini, A., Del Soldato, M., Montalti, R., Solari, L., Tofani, V., & Casagli, N. (2019). Persistent Scatterers continuous streaming for landslide monitoring and mapping: the case of the Tuscany region (Italy). *Landslides*, *16*, 2033–2044. <https://doi.org/10.1007/s10346-019-01249-w>
- Ratto, S., Bonetto, F., & Comoglio, C. (2003). The October 2000 flooding in Valle d’Aosta (Italy): Event description and land planning measures for the risk mitigation. *International Journal of River Basin Management*, *1*(2), 105–116. <https://doi.org/10.1080/15715124.2003.9635197>
- Reinosch, E., Buckel, J., Dong, J., Gerke, M., Baade, J., & Riedel, B. (2020). InSAR time series analysis of seasonal surface displacement dynamics on the Tibetan Plateau. *Cryosphere*, *14*, 1633–1650. <https://doi.org/10.5194/tc-14-1633-2020>
- Richman, D. (1982). *U.S. Patent No. 4,321,601*. 1982. Washington, DC: U.S. Patent and Trademark Office.
- Rick, B., Delaloye, R., & Barboux, C. (2015). Detection and inventorying of slope movements in the Brooks Range, Alaska using DInSAR: a test study. 68e Conférence Canadienne de Géotechnique et 7e Conférence Canadienne Sur Le Pergélisol, 20 Au 23 Septembre 2015, Québec, Québec.
- Rignot, E., Hallet, B., & Fountain, A. (2002). Rock glacier surface motion in Beacon Valley, Antarctica, from synthetic-aperture radar interferometry. *Geophysical Research Letters*, *29*. <https://doi.org/10.1029/2001GL013494>
- Rizzoli, P., & Bräutigam, B. (2014). Radar backscatter modeling based on global TanDEM-X mission data. *IEEE Transactions on Geoscience and Remote Sensing*, *52*(9), 5974–5988. <https://doi.org/10.1109/TGRS.2013.2294352>
- Romanovsky, V.E., Marchenko, S.S., Daanen, R., Sergeev, D.O., & Walker, D.A. (2008). Soil climate and frost heave along the permafrost/ecological North American Arctic transect. *Proceedings of the Ninth International Conference on Permafrost*, *2*, 1519–1524.
- Rosen, P. A., Hensley, S., Joughin, I.R., Li, F.K., Madsen, S.N., Rodriguez, E., & Goldstein, R.M. (2000). Synthetic aperture radar interferometry. *PROCEEDINGS OF THE IEEE*, *88*(3), 333–382. <https://doi.org/10.1109/5.838084>

- Rouyet, L., Lauknes, T. R., Christiansen, H. H., Strand, S. M., & Larsen, Y. (2019). Seasonal dynamics of a permafrost landscape, Adventdalen, Svalbard, investigated by InSAR. *Remote Sensing of Environment*, 231(111236). <https://doi.org/10.1016/j.rse.2019.111236>
- Salvatici, T., Tofani, V., Rossi, G., D'Ambrosio, M., Tacconi Stefanelli, C., Benedetta Masi, E., Rosi, A., Pazzi, V., Vannocci, P., Petrolo, M., Catani, F., Ratto, S., Stevenin, H., & Casagli, N. (2018). Application of a physically based model to forecast shallow landslides at a regional scale. *Natural Hazards and Earth System Sciences*, 18, 1919–1935. <https://doi.org/10.5194/nhess-18-1919-2018>
- Sandau, R. (2010). Status and trends of small satellite missions for Earth observation. *Acta Astronautica*, 66, 1–12. <https://doi.org/10.1016/j.actaastro.2009.06.008>
- Schneuwly-Bollschweiler, M., & Stoffel, M. (2012). Hydrometeorological triggers of periglacial debris flows in the Zermatt valley (Switzerland) since 1864. *Journal of Geophysical Research: Earth Surface*, 117(F02033). <https://doi.org/10.1029/2011JF002262>
- Selva, D., & Krejci, D. (2012). A survey and assessment of the capabilities of Cubesats for Earth observation. *Acta Astronautica*, 74, 50–68. <https://doi.org/10.1016/j.actaastro.2011.12.014>
- Shan, W., Hu, Z., Guo, Y., Zhang, C., Wang, C., Jiang, H., Liu, Y., & Xiao, J. (2015). The impact of climate change on landslides in southeastern of high-latitude permafrost regions of China. *Frontiers in Earth Science*, 3. <https://doi.org/10.3389/feart.2016.00022>
- Shan, W., Xu, Z., Guo, Y., Zhang, C., Hu, Z., & Wang, Y. (2020). Geological methane emissions and wildfire risk in the degraded permafrost area of the Xiao Xing'an Mountains, China. *Scientific Reports*, 10(21297). <https://doi.org/10.1038/s41598-020-78170-z>
- Shi, P.J., Sun, S., Wang, M., Li, N., Wang, J.A., Jin, Y.Y., Gu, X.T., & Yin, W.X. (2014). Climate change regionalization in China (1961–2010). *Science China Earth Sciences*, 57(11), 2676–2689. <https://doi.org/10.1007/s11430-014-4889-1>
- Shur, Y., Hinkel, K. M., & Nelson, F. E. (2005). The transient layer: Implications for geocryology and climate-change science. *Permafrost and Periglacial Processes*, 16, 5–17. <https://doi.org/10.1002/ppp.518>
- Sinha, S., Jeganathan, C., Sharma, L. K., & Nathawat, M. S. (2015). A review of radar remote sensing for biomass estimation. *International Journal of Environmental Science and Technology*, 12, 1779–1792. <https://doi.org/10.1007/s13762-015-0750-0>
- Solari, L., Del Soldato, M., Montalti, R., Bianchini, S., Raspini, F., Thuegaz, P., Bertolo, D., Tofani, V., & Casagli, N. (2019). A Sentinel-1 based hot-spot analysis: landslide mapping in north-western Italy. *International Journal of Remote Sensing*, 40(20), 7898–7921. <https://doi.org/10.1080/01431161.2019.1607612>
- Solari, L., Bianchini, S., Franceschini, R., Barra, A., Monserrat, O., Thuegaz, P., P.; Bertolo, D., Crosetto, M., & Catani, F. (2020). Satellite interferometric data for landslide intensity evaluation in mountainous regions. *International Journal of Applied Earth Observation and Geoinformation*, 87(102028). <https://doi.org/10.1016/j.jag.2019.102028>

- Stanley, T., & Kirschbaum, D. B. (2017). A heuristic approach to global landslide susceptibility mapping. *Natural Hazards*, 87, 145–164. <https://doi.org/10.1007/s11069-017-2757-y>
- Strozzi, T., Kääh, A., & Frauenfelder, R. (2004). Detecting and quantifying mountain permafrost creep from in situ inventory, space-borne radar interferometry and airborne digital photogrammetry. *International Journal of Remote Sensing*, 25(15), 2919–2931. <https://doi.org/10.1080/0143116042000192330>
- Strozzi, T., Farina, P., Corsini, A., Ambrosi, C., Thüning, M., Zilger, J., Wiesmann, A., Wegmüller, U., & Werner, C. (2005). Survey and monitoring of landslide displacements by means of L-band satellite SAR interferometry. *Landslides*, 2, 193–201. <https://doi.org/10.1007/s10346-005-0003-2>
- Strozzi, T., Wegmüller, U., Keusen, H. R., Graf, K., & Wiesmann, A. (2006). Analysis of the terrain displacement along a funicular by SAR interferometry. *IEEE Geoscience and Remote Sensing Letters*, 3(1), 15–18. <https://doi.org/10.1109/LGRS.2005.855072>
- Strozzi, T., Antonova, S., Günther, F., Mätzler, E., Vieira, G., Wegmüller, U., Westermann, H., & Bartsch, A. (2018). Sentinel-1 SAR interferometry for surface deformation monitoring in low-land permafrost areas. *Remote Sensing*, 10(1360). <https://doi.org/10.3390/rs10091360>
- Strozzi, T., Caduff, R., Jones, N., Barboux, C., Delaloye, R., Bodin, X., Kääh, A., Mätzler, E., & Schrott, L. (2020). Monitoring rock glacier kinematics with satellite synthetic aperture radar. *Remote Sensing*, 12(559). <https://doi.org/10.3390/rs12030559>
- Tadono, T., Ishida, H., Oda, F., Naito, S., Minakawa, K., & Iwamoto, H. (2014). Precise Global DEM Generation by ALOS PRISM. *ISPRS Annals of the Photogrammetry, Remote Sensing and Spatial Information Sciences*, II(4), 71–76. <https://doi.org/10.5194/isprsannals-ii-4-71-2014>
- Torres, R., Snoeij, P., Geudtner, D., Bibby, D., Davidson, M., Attema, E., Potin, P., Rommen, B., Floury, N., Brown, M., Traver, I.N., Deghaye, P., Duesmann, B., Rosich, B., Miranda, N., Bruno, C., L'Abbate, M., Croci, R., Pietropaolo, A., Huchler, M., & Rostan, F. (2012). GMES Sentinel-1 mission. *Remote Sensing of Environment*, 120, 9–24. <https://doi.org/10.1016/j.rse.2011.05.028>
- Trofaier, A. M., Westermann, S., & Bartsch, A. (2017). Progress in space-borne studies of permafrost for climate science: Towards a multi-ECV approach. *Remote Sensing of Environment*, 203, 55–70. <https://doi.org/10.1016/j.rse.2017.05.021>
- Villarroel, C. D., Beliveau, G. T., Forte, A. P., Monserrat, O., & Morvillo, M. (2018). DInSAR for a regional inventory of active rock glaciers in the Dry Andes Mountains of Argentina and Chile with sentinel-1 data. *Remote Sensing*, 10(1588). <https://doi.org/10.3390/rs10101588>
- Wang, S., Xu, B., Shan, W., Shi, J., Li, Z., & Feng, G. (2019). Monitoring the degradation of island permafrost using time-series insar technique: A case study of heihe, China. *Sensors (Switzerland)*, 19(1364). <https://doi.org/10.3390/s19061364>
- Wang, X., Liu, L., Zhao, L., Wu, T., Li, Z., & Liu, G. (2017). Mapping and inventorying active rock glaciers in the northern Tien Shan of China using satellite SAR interferometry. *Cryosphere*, 11, 997–1014. <https://doi.org/10.5194/tc-11-997-2017>



- Werner, C., Wegmüller, U., Strozzi, T., & Wiesmann, A. (2003). Interferometric Point Target Analysis for Deformation Mapping. *International Geoscience and Remote Sensing Symposium (IGARSS)*, 4362–4364. <https://doi.org/10.1109/igarss.2003.1295516>
- Wu, Q., Liu, Y., Zhang, J., & Tong, C. (2002). A review of recent frozen soil engineering in permafrost regions along Qinghai-Tibet Highway, China. *Permafrost and Periglacial Processes*, 13(3), 199–205. <https://doi.org/10.1002/ppp.420>
- Zahs, V., Hämmerle, M., Anders, K., Hecht, S., Sailer, R., Rutzinger, M., Williams, J.G., & Höfle, B. (2019). Multi-temporal 3D point cloud-based quantification and analysis of geomorphological activity at an alpine rock glacier using airborne and terrestrial LiDAR. *Permafrost and Periglacial Processes*, 30, 222–238. <https://doi.org/10.1002/ppp.2004>